Operational modal analysis on the SA Agulhas II

by
Christof Moolman van Zijl

Thesis presented in partial fulfilment of the requirements for the degree of Master of Engineering (Mechanical) in the Faculty of Engineering at Stellenbosch University

Supervisor: Prof. A. Bekker

March 2020

Declaration

By submitting this thesis electronically, I declare that the entirety of the work contained therein is my own, original work, that I am the sole author thereof (save to the extent explicitly otherwise stated), that reproduction and publication thereof by Stellenbosch University will not infringe any third party rights and that I have not previously in its entirety or in part submitted it for obtaining any qualification.

Date: March 2020

Abstract

Operational modal analysis on the SA Agulhas II

CM. van Zijl

Thesis: MEng (Mechanical)

March 2020

Full-scale operational measurements were conducted on a polar vessel during an expedition to Antarctica. Accelerometers distributed along the length of the vessel were used to capture vertical, lateral and torsional hull global motions. A parametric study on a stochastic subspace identification technique was conducted to investigate the effect of user-specified parameters on modal parameters. With low block sizes weakly excited modes were not identified and increasing block size up to fifty was found to reduce both random and bias errors. Measurement duration below twenty minutes were found to produce relatively large bias and random errors, however there was little improvement with increasing measurement duration beyond twenty minutes. Extreme model orders were found to produce scatter on estimates and a suitable range of model orders were found to be between 200 and 300. A modal model consisting of five modes was identified for the SA Agulhas II. Modes were automatically tracked across four different cases of operational data. Vertical bending modes were tracked consistently across all four cases, but lateral and torsional modes were not. Energy in modal responses were highest for vertical bending modes and significant energy was found to be concentrated around vertical bending modes during an open water storm case. An analysis of the time-varying behaviour of modes in the four cases revealed highly non-stationary modal responses during an open water storm and two ice cases. The transients were found to correspond with impulsive wave slamming events in open water and ship-ice interactions during ice breaking.

Uittreksel

("Operational modal analysis on the SA Agulhas II")

CM. van Zijl

Tesis: MIng (Meganies)

Maart 2020

'n Volskaalse meting is uitgevoer op 'n poolnavorsingskip tydens 'n ekspedisie na Antarktika. 'n Stel versnellingsmeters is gebruik om die vertikale, laterale en torsionele bewegings van die romp van die skip te bepaal. 'n Parametriese studie is uitgevoer op die stochastiese subspasie identifikasie tegniek om die effek van die verstelling van parameters op modusse te ondersoek. Teen lae blokgrotes word swak opgewekte modusse nie geïdentifiseer nie, terwyl by die verhoging van blokgrote tot vyftig, is daar gevind dat ewekansige foute, sowel as sydigheid verminder is. 'n Meting onder twintig minute veroorsaak relatief groot ewekansige foute en sydigheid, maar daar is weinig verbetering om 'n meting langer as twintig minute te gebruik. Ekstreme model ordes veroorsaak verstrooiing van die modale skattings en 'n geskikte reeks van model ordes is tussen 200 en 300. 'n Modale model van vyf modusse is vir die SA Agulhas geïdentifiseer. A utomatiese naspeuring van modusse is toegepas op vier verskillende gevalle van operasionele toestande. Die vertikale buigmodusse is goed nagespeur oor die vier gevalle, maar nie die laterale buigmodus en torsionale modus nie. Die energie in die eerste vertikale buigmodus is die hoogste. 'n Groot hoeveelheid energie is gekonsentreer by hierdie modus gedurende die oop water stormgeval. 'n Analise met betreking tot die tydveranderlike gedrag van die modusse in hierdie vier gevalle wys dat die gedrag van die modusse nie-stationêr is tydens die oop water en ys gevalle nie. Die transiënte gedrag stem ooreen met impulsiewe golfslaggebeurtenisse en interaksies tussen die romp van die skip met ys.

Acknowledgements

Firstly, to my mother, who is still my best friend. Thank you that I can always fully be myself around you. To Professor Annie Bekker for her guidance and support throughout this degree and for helping me to believe in myself again. You are one of the most passionate people I know and I have been immensely privileged to work with you these last three years. Thank you for all the valuable "table-cloth" talks. A big thank you to Ross, Dannielle, Stefan, Caleb, Emma and Jonathan for their love and support. I cherish every memory that I have shared with you and look forward to many more. I would like to thank the Deutsches Zentrum für Luft und Raumfahrt (DLR) for a highly enriching and memorable research exchange. Many of the ideas in this thesis are the result of the time I spent at DLR, surrounded by incredible people and with free access to the in-house MATLAB SAS Toolbox. A special thank you to Keith Soal who inspired and motivated me and challenged me to grow beyond that which I thought was possible. To James-John Matthee and LiangLiang Lu for making the time in Antarctica especially memorable. Without their help the full-scale measurements on the SA Agulhas II would have been impossible. Thank you to Captain Knowledge Bengu and Captain Freddie Ligthelm and the crew of the SA Agulhas II who made life and work on the ship possible and all the more enjoyable. I am grateful to the Department of Environmental Affairs of South Africa and Flotilla Foundation that I could be a member of the SANAE 58 voyage and Weddell Sea Expedition. Lastly, I would like to thank God who I have come to know during this degree as Life, Truth, Light, Strength and Peace. Thank you that I can call you Father and Friend.

> Whoever find his life will lose it, and whoever loses his life for my sake shall find it (Matthew 10:39).

Contents

List of Figures

List of Tables

Chapter 1

Introduction

1.1 Background

Ice-going vessels operate under extreme environmental conditions. Interactions with waves and sea-ice result in dynamic systems with changing boundary conditions, complex environmental loads and the effective structural (dynamic) properties attributed to the system itself. Along with large static forces that arise from wave and ice actions on the vessel hull, energy from these inputs propagate through the structure causing significant vibrations. These motions and vibrations are related to the incidence motion sickness and discomfort of human inhabitants (Bekker *et al.*, 2017) and have implications for the structural health of ships due to low-cycle fatigue damage (Blenkarn, 1970). Key considerations concerning the operation of these vessels is management of wave- and ice-induced loads to prevent catastrophic failure and to maintain safe levels of structural vibration and maintain service life (Hamilton *et al.*, 2011).

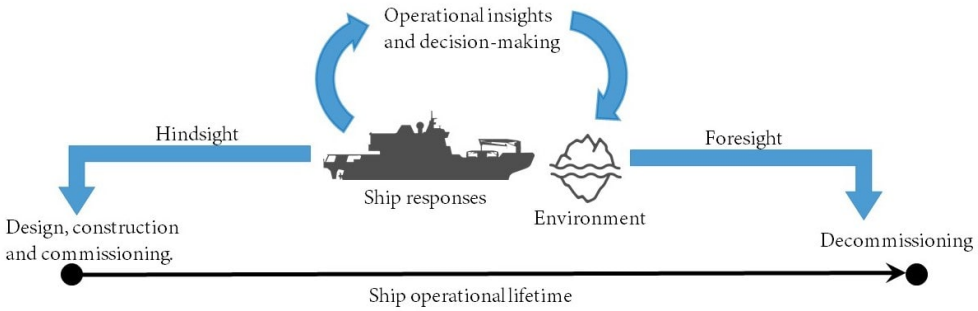

Figure 1.1: Illustration of insights gained from full-scale ship data throughout its lifetime.

Full-scale data collected from ships provides invaluable insights during its operational lifetime, Figure 1.1. The design of ice-going vessels is largely based on data extrapolated from model-scale tests and computed-based finite-element models. However, it is extremely difficult to exactly simulate the boundary conditions and environmental loading conditions of the actual operational environment. This is especially true for vessels operating in Antarctica for which data is sparse and which do not only operate in ice-infested waters but face harsh open water conditions in the Southern Ocean. Mathematical models that are built from full-scale measurements may further be used in finite element model updating and stochastic model updating (Govers, 2012) to provide additional information for the design of these ships. In addition to this hindsight perspective, mathematical models from operational data combined with statistical tools may provide valuable foresight in terms of predictions concerning the useful lifetime of the ship (Farrar and Worden, 2012; Mendler *et al.*, 2019). Recent developments in digital twin technology in the shipping industry (Erikstad, 2018) further motivate the use of physics-based and/or statistical models together with semi real-time measurements to provide actionable insights into ship operations. Digital twins may be defined as a virtual model of a real asset that represents the actual state and behaviour of an asset in close-to to real time based on sensor input (Erikstad, 2018).

Figure 1.2: The SA Agulhas II conducting cargo operations at a logistics discharge point at Penguin Bukta in Antarctica.

The SA Agulhas II (SAAII) is a South African polar supply and research vessel, providing key logistical support for the South African National Antarctic Programme (SANAP) and facilitating research in the Southern Ocean and Antarctica since her commissioning in 2012, Figure 1.2. The Sound and Vibration Research Group (SVRG) at Stellenbosch University forms part of an international consortium that aims to acquire full-scale data from the SAAII in her operational environment towards providing a scientific basis for the design of these vessels (Bekker *et al.*, 2018). Recently research interest at the SVRG concerning the SAAII has shifted to include digital services from sensor data to provide operational assistance to navigational officers and stakeholders (Bekker, 2018).

1.2 Operational modal analysis

Mathematical models that describe the dynamic behaviour of structures play an integral role in extracting the useful hindsight and foresight perspectives and operational insights described in the previous section. The so-called modal model, which describes the dynamic behaviour of structures in terms of natural frequencies, damping ratios and mode shapes (Maia and Silva, 1997) serve as inputs to advanced fields such as structural health monitoring (SHM) (Peeters, 2000), damage detection (Mendler *et al.*, 2019) and stochastic model updating (Govers, 2012)

Operational modal analysis (OMA) overcomes many challenges associated with applying traditional experimental modal analysis (EMA) to large structures. Firstly, some structures are too large to conduct the laboratory-based experiments that are common in EMA. Secondly, it is particularly difficult to simulate the complex boundary conditions that these types of structures are subjected to in operation. Since boundary conditions affect the dynamic properties of the structure, laboratory testing is not always a true reflection of the actual system response. Thirdly, unless multiple, large exciters are used it is unlikely that the modes of interest will be excited sufficiently to extract information about the modal parameters of the structure. The benefits of OMA are that testing is conducted in-operation with excitation from normal environmental inputs such as, for example, wind, waves and ice. Due to the complexity involved with measuring environmental loads, only the responses are measured and modal parameters are identified without any information regarding the magnitude or exact location of input forces. The trade-off associated with the absence of measured inputs is that the character of the loading is assumed to be random in both time and space (Brincker and Ventura, 2015). In other words, the inputs are assumed to be white noise with a stochastic spatial distribution across the structure.

Application of the modal model in advanced topic such as SHM, for example, often involve ‘tracking” the evolution of modes over time across different operating

conditions. In recent years considerable amount of attention has been devoted towards tracking modes using automated modal analysis procedures on different structures such as buildings (Sarlo *et al.*, 2018), bridges (Magalhaes and Cunha, 2011; Marrongelli *et al.*, 2017), icebreakers (Heyn and Skjetne, 2018; Soal *et al.*, 2019*a*) and lighthouses in the Arctic (Nord *et al.*, 2019)

1.3 Research aim

The aim of this thesis is to investigate OMA as a tool to build a modal model of the SA Agulhas II from full-scale responses recorded during normal ship operations. Since this work forms part of a larger vision that involves the development of state-of-the-art monitoring and decision-aiding systems, some important aspects need to be considered:

- Modal parameters that are obtained using modal identification algorithms need to be qualitatively assessed to ensure that the modal model is reliable. Performance of these techniques typically depend on various factors such as the extent to which the underlying assumption of stochastic inputs are violated which introduces uncertainties in the modal parameter estimates (Reynders *et al.*, 2008). Further, algorithm-specific parameters that need to be selected by the user often produces very different modal parameter estimates and the exact reasons for this are generally not well understood (Marrongelli *et al.*, 2017; Soal, 2018; Sarlo *et al.*, 2018).
- Automating the modal analysis process is key towards tracking changes in modal parameters across different operating conditions. As explained in the previous section, tracking the evolution of modes is important for the application of advanced research topics such as structural health monitoring and stochastic model updating.

Against this backdrop, the main objectives of the project may be summarised as follows:

1. To acquire full-scale measurements from the SA Agulhas II during normal operations in the Southern Ocean and Antarctica. The vessel will be instrumented with the necessary sensors and cables for the acquisition of continuous acceleration measurements. Observations of environmental conditions and operational ship parameters will further be collected.
2. To study at least one OMA identification algorithm in detail to form a solid theoretical basis according to which the resulting modal parameter estimates

can be assessed. The OMA algorithm will be tested on full-scale data and the potential challenges and limitations associated with the applied algorithm will be explored. Accurate estimate of modal parameters will be used to build a modal model of the ship.

3. The identified modal model will be used to explore the insights that may be gained from operational ship data. Various cases of the ship in its operational environment will be used to further assess the performance of OMA identification algorithms and to understand the complex interactions that occurs between vessels operating in Antarctica.

1.4 Organisation of text

The layout of the thesis is presented in this section to guide the reader. Chapter 2 presents a review of relevant literature relating to modal analysis, OMA theory and an overview of different OMA identification techniques. Further, different automated procedures for OMA are presented along with a summary of OMA applied to different ship structures. A brief overview of ice mechanics and ice-structure interactions discussed. In Chapter 3, a description of full-scale measurements conducted on the SA Agulhas II during a voyage to Antarctica are presented. Chapter 4 starts with a discussion of the data-driven SSI algorithm and the selection of user-specified parameters is introduced. A parametric study is conducted to provide guidelines for selecting appropriate parameters to identify an accurate modal model from operational data. Different operational case studies are presented in Chapter 6 along with an investigation into the insights that may be gained from OMA results.

Chapter 2

Literature study

2.1 Introduction

The aim of this thesis is to use operational modal analysis (OMA) to build a modal model of the SA Agulhas II and to automatically track changes in modal parameters across different operating conditions. Changes in modal parameters over time provides potential insights towards operational decision-making and into predicting the structural health of the vessel. This chapter starts with a review of different dynamic models and the modal model. Then some concepts relating to OMA are briefly reviewed. Important concepts relating to automated modal analysis procedures are discussed next before reviewing some OMA studies that have already been conducted on ships. Finally, principles of ice-structure interactions are reviewed which are important for the interpretation operational data collected during ice breaking.

2.2 Dynamic models of vibrating structures

Civil and mechanical engineering structures are inherently complex. Such structures consist of infinitely many "points" that have three translational and three rotational degrees of freedom (six in total). A convenient way to analyse these structures is to use a simplified model that exhibits approximately the same dynamic characteristics of the actual structure. A commonly used model for vibrating models is the multi-degree of freedom (MDOF) model.

2.2.1 Multi-degree of freedom model

The MDOF model consists of masses connected by springs and dampers. Such a model aims to capture inertial, elastic and viscous damping effects that exist in

many real structures and generally approximates the behaviour of these structures quite closely. Figure 2.1 shows a MDOF system with N masses. The MDOF model is generally categorised as a linear time-invariant (LTI) system in system identification (Kailath, 1980) and may be mathematically described by the linear second-order differential equation in Eq. 2.1.

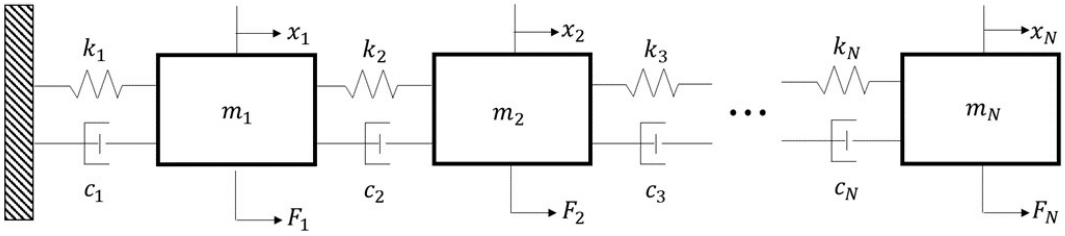

Figure 2.1: The MDOF system for vibrating structures.

$$M\ddot{z}(t) + D\dot{z}(t) + Kz(t) = F(t) = bu(t) \tag{2.1}$$

In Eq. 2.1 $M \in \mathbb{R}^{n\times n}$ is the mass matrix, $D \in \mathbb{R}^{n\times n}$ is the damping matrix and $K \in \mathbb{R}^{n\times n}$ is the stiffness matrix. The matrices M, D and K are referred as the spatial parameters of the MDOF model and constitute what is known as the spatial model of a MDOF system. Notice that in Equation 2.1, the spatial parameters are independent of time. Further, $z(t) \in \mathbb{R}^{n\times 1}$ contains the displacement coordinates of each degree of freedom and $F(t) \in \mathbb{R}^{n\times 1}$ describes the input force acting at each degree of freedom. The force vector may further be factored into a matrix $b \in \mathbb{R}^{n\times n}$ and vector $u(t) \in \mathbb{R}^{n\times 1}$ which describe the spatial distribution and magnitude of the input force, respectively.

Although the MDOF model represents the behaviour of vibrating structures quite accurately, this model is rarely used in the form presented in Equation 2.1. Instead, there are advantages to using an alternative representation of the structural dynamics, called state space models.

2.2.2 Continuous-time state space models

State space models originate in control and electrical engineering and generally apply to any dynamic system. A system is generally any object on which inputs act to produce a change in internal behaviour (state) resulting in observable outputs. A continuous-time state space model is obtained for the MDOF model by defining a state variable $x(t) \in \mathbb{R}^{2n\times 1}$, a state matrix $A \in \mathbb{R}^{2n\times 2n}$ and a input matrix $B \in \mathbb{R}^{2n\times 1}$ as follows:

$$x(t) = \begin{pmatrix} z(t) \\ \dot{z}(t) \end{pmatrix}, A_c = \begin{pmatrix} 0 & I_n \\ -M^{-1}K & -M^{-1}D \end{pmatrix}, B_c = \begin{pmatrix} 0 \\ -M^{-1}b \end{pmatrix} \tag{2.2}$$

Now the spatial model in Equation 2.1 may be written in the following form:

$$\dot{x}(t) = A_c x(t) + B_c u(t) \tag{2.3}$$

At this point it is worthwhile to consider some of the variables that have been defined in Eq. 2.2 in more detail. The state variable contains the states of the system. In theory, the states are the minimum number of variables required to fully describe the dynamic behaviour of the system. Moreover, in Eq. 2.3 the state matrix A_c is shown to hold the $N \times N$ parameter matrices and as such represents the dynamic properties of the N DOF structure. In fact, the state transition matrix contains a description of the dynamic properties of the structure in its eigen-solution. This will be discussed in detail in Section 2.3. With this in mind, Eq. 2.3 makes intuitive sense since it simply states that the change in internal dynamic behaviour (state) of the system $\dot{x}(t)$ depends on the current state $x(t)$, its dynamic properties A and the nature and spatial distribution of the input force $u(t)$. An additional observation equation may be defined to relate the l observed outputs of the structure to the internal state of the system and to the input forces acting on the structure:

$$y(t) = C_c x(t) + E_c u(t) \tag{2.4}$$

Where $C_c \in \mathbb{R}^{l \times N}$ is the observation matrix and $E_c \in \mathbb{R}^{l \times m}$ is the direct transmission matrix. Intuitively, Eq. 2.4 relates the observable outputs of the structure to the internal dynamic behaviour (state) and to some direct feedthrough action of the input forces. One advantage of the continuous state space formulation presented here is that a direct analytical solution may readily be obtained (Kailath, 1980):

$$x(t) = e^{A_c t}\, x(0) + \int_0^t e^{A_c(t-\tau)}\, B_c\, u(t) \tag{2.5}$$

Eq. 2.5, $x(0)$ consists of two solutions (represented by the two terms): (1) the homogenous (free-response) solution which assumes zero input ($u(t) = 0$) and (2) a non-homogenous (forced) solution which models the action of the input force. $x(0)$ represents the initial conditions of the system (without which there would be no free response). Assuming , for now, only a free response (due to some initial conditions without any inputs), the system outputs are obtained from Equation 2.4 using Equation 2.5:

$$y(t) = C e^{A_c t}\, x(0) \tag{2.6}$$

2.2.3 Discrete-time state space models

The continuous-time state space model presented in the previous section assumes that states and outputs of a system can be realised as continuous functions in time. In reality, knowledge of the states and outputs are confined to discrete time instances. To account for this, the continuous-time state space models in Equation 2.3 and Eq. 2.4 may be transformed to a discrete-time model:

$$x_{k+1} = Ax_k + Bu_k \tag{2.7}$$

$$y_k = Cx_k + Du_k \tag{2.8}$$

The discrete-time model in Eq.2.7 and Eq. 2.8 are obtained by applying a so-called zero-order hold (ZOH) discretisation scheme to the continuous-time state space model. The ZOH assumes that the states and outputs remain constant between sampling instants. Assuming ZOH, the parameters of the continuous model (A_c, B_c, C_c, D_d) are related to the corresponding discrete-time parameters as follows:

$$A = e^{A_c \Delta t}, \quad B = (A - I)A_c^{-1}B_c, \quad C = C_c \text{ and } D = D_c \tag{2.9}$$

Using the definitions in Eq.2.9, the homogenous solution of the continuous-time state space model in Eq. 2.5 may be obtained for the discrete-time system:

$$\begin{aligned} x_k &= e^{A_c k \Delta t}\ x_0 \\ x_k &= A^k\ x_0 \end{aligned} \tag{2.10}$$

Similarly, the discrete outputs are:

$$y_k = C\ A^k\ x_0 \tag{2.11}$$

2.2.4 Model and measurement noise

The discrete-time state space model may further be adapted to account for model noise and measurement noise. Model noise arises due to inherent inaccuracies in the mathematical model. For example, the MDOF model in Eq. 2.1 assumes that the structure is linear and time-invariant. Measurement noise, as the name suggests, is introduced on measured inputs and outputs by imperfect transducers and cables. Model noise and measurement noise may be introduced in the discrete-time state space model as follows:

$$x_{k+1} = Ax_k + Bu_k + v_k \tag{2.12}$$

$$y_k = Cx_k + Du_k + w_k \tag{2.13}$$

The quantities v_k and w_k are usually assumed to be stochastic quantities with special properties and are dealt with using specific mathematical and statistical techniques. However, introducing these quantities (which are not deterministic) means that analytical solution as in Eq. 2.5 and Eq. 2.10 are not available.

2.3 The modal model

Although the state space models presented in the previous section prove to be very useful for solving for the dynamics of the MDOF model, further insights into the behaviour of vibrating structures is gained from a so-called modal model.

2.3.1 Free response solution

The modal model is derived from the continuous-time state space model by performing an eigenvalue decomposition on the state matrix A_c:

$$A_c = \Psi_c \Gamma_c \Psi_c^T \tag{2.14}$$

Where $\Psi_c \in \mathbb{C}^{l \times 2n}$ holds the $2n$ eigenvectors $\psi_{c,r} \in \mathbb{C}^{l \times 1}$ of the matrix A_c in its columns and the corresponding $2n$ eigenvalues $\lambda_{c,r}$ are the entries of the diagonal matrix $\Gamma_c \in \mathbb{C}^{2n \times 2n}$ $(r = 1, 2, ..., 2n)$. Often it is assumed that the system is "under-damped". This simply means that the entries of the damping matrix are relatively small compared to the entries of the mass and stiffness matrices and that the vibration response will involve some oscillatory behaviour before returning to equilibrium. In this case, the eigen-solution of A_c consists of n complex conjugate pairs of eigenvalues and eigenvectors:

$$\Psi_c = \begin{pmatrix} \psi_{c,1} & \psi_{c,2} & \cdots & \psi_{c,n} & \psi_{c,1}^* & \psi_{c,2}^* & \cdots \psi_{c,n}^* \end{pmatrix} \tag{2.15}$$

$$\Gamma_c = \begin{pmatrix} \lambda_{c,1} & 0 & \cdots & 0 & 0 & 0 & \cdots & 0 \\ 0 & \lambda_{c,2} & \cdots & 0 & 0 & 0 & \cdots & 0 \\ \vdots & \vdots & \ddots & \vdots & \vdots & \vdots & \vdots & \vdots \\ 0 & 0 & \cdots & \lambda_{c,n} & 0 & 0 & \cdots & 0 \\ 0 & 0 & \cdots & 0 & \lambda^*_{c,1} & 0 & \cdots & 0 \\ 0 & 0 & \cdots & 0 & 0 & \lambda^*_{c,2} & \cdots & 0 \\ \vdots & \vdots & \vdots & \vdots & \vdots & \vdots & \ddots & \vdots \\ 0 & 0 & \cdots & 0 & 0 & 0 & \cdots & \lambda^*_{c,n} \end{pmatrix} \tag{2.16}$$

With $\psi_{c,r}$ $(r = 1, 2, ...n)$ representing the r^{th} unique eigenvector of A_c and $\psi^*_{c,r}$ the corresponding complex conjugate. Similarly, $\lambda_{c,r}$ $(r = 1, 2, ..., n)$ and $\lambda^*_{c,r}$ are the r^{th} unique eigenvalue and corresponding complex conjugate, respectively. Using the matrix Ψ_c, the state variable of the continuous-time state space model may be transformed to modal coordinates:

$$x(t) = \Psi_c q(t) \tag{2.17}$$

The reason for this transformation will become clear as the discussion progresses. For now, assume that we are only interested in the free response of the system (i.e. $u(t) = 0$)). Further, substituting Eq. 2.17 into Eq. 2.3 and pre-multiplying the entire equation with Ψ^T_r:

$$\Psi^T_c \Psi_c \dot{q}(t) = \Psi^T_c A_c \Psi_c q(t) \tag{2.18}$$

And using the orthogonality properties of eigenvectors (Maia and Silva, 1997):

$$\psi_{c,i} A_c \psi^T_{c,j} = \begin{cases} 1, & \text{if } i = j \\ 0, & \text{if } i \neq j \end{cases} \tag{2.19}$$

The following result is obtained:

$$\dot{q}(t) = \Gamma_c q(t) \tag{2.20}$$

Where Γ_c is a diagonal matrix and Eq.2.20 represents a set of $2n$ uncoupled first order differential equations with the following solution in matrix form:

$$q(t) = e^{\Gamma_c t} Q \tag{2.21}$$

Where $Q \in \mathbb{R}^{2n \times 1}$ represents a vector of integration constants and $e^{\Gamma_c t} \in \mathbb{C}^{2n \times 2n}$ is a diagonal matrix with the r^{th} entry equal to $e^{\lambda_{c,r}}$. Reversing the coordinate transform in Eq. 2.17, the solution for the state variable $x(t)$ may be obtained:

$$x(t) = \Psi_c e^{\Gamma_c t} Q = \sum_{r=1}^{2n} Q_r \psi_{c,r} e^{\lambda_{c,r} t} \tag{2.22}$$

The form of Equation 2.22 is convenient, because it expresses the total vibration response as the sum of n simple vibratory motions called modes. Each mode is described by four so-called modal parameters, namely a natural frequency, damping ratio, mode shape and modal scaling constant. The natural frequencies and damping ratios belonging to each mode is obtained directly from the corresponding eigenvalues $\lambda_{c,r}, r = 1, 2, 3, ...n$:

$$\lambda_{c,r} = -\zeta_r \omega_r + i\omega_r \sqrt{1 - \zeta_r^2} \tag{2.23}$$

With ω_r and ζ_r representing the r^{th} natural frequency and damping ratio, respectively. Using Equation 2.23, the term $e^{\lambda_{c,r} t}$ in Equation 2.22 may be interpreted as the product of a decaying exponential function, with rate of decay determined by $\zeta_r \omega_r$ and a harmonic function with frequency equal to $\omega_r \sqrt{1 - \zeta_r^2}$. This means that the total vibration time-response is simply the sum of decaying harmonic functions. Further, the time-response of each mode is multiplied by a spatial solution, which is represented by the eigenvector. The eigenvector maps the time-response to each degree of freedom and assigns a relative displacement magnitude, direction and phase (the phase is due to the complexity of the eigenvectors). The eigenvector is often called a mode shape since it represents a "shape" of deformation associated with each mode. The modal scaling constant Q_r represents the contribution of each mode to the overall response and depends on the initial conditions of the system.

2.3.2 Forced response

Up until now, only a free response has been considered. The free response provides insight into how a structure could respond due to its inherent dynamic properties. The forced response provides information about how the structure will respond to excitation. Using the free response solution in Eq. 2.22, the forced response may be represented by the following convolution integral:

$$x_p(t) = \int_0^t e^{\Gamma_c (t-s)} \; \Psi_c^T \; B_c \; u(s) ds \tag{2.24}$$

The result produced by the convolution integral in Equation 2.24 is rather complicated. However, the most important point here is that convolution of the forcing function with the free response represented by $e^{\Gamma(t-s)}$ produces a signal that has properties of both "parent" signals. If the forcing function is similar (in frequency) to one of the modes, then the resulting signal will be dominated by the

convolution of this modal response and the forcing function. The spatial distribution of the input force further influences the resulting forced vibration due to the shape associated with each mode of deformation. For example, if the input acts at a degree of freedom with a large relative amplitude in the mode shape of the mode that is excited, the resulting deformation will be large. The phenomenon where excitation at a natural frequency causes a single modal response to dominate is called resonance (Inman, 2001). During resonance all the input energy is concentrated around a single mode of deformation and can cause high stresses at the degrees of freedom with large mode shape components.

2.4 Operational modal analysis

In this section, stochastic processes are introduced. Then some of the underlying assumptions relating to OMA are discussed, along with an overview of different identification techniques and previous studies involving OMA on ship structures.

2.4.1 Stochastic processes

Familiarity with some concepts from stochastic vibration theory is integral to understanding the OMA framework. First, covariance or correlation functions are introduced. Strictly speaking, covariances and correlation functions are not the same, but for zero mean processes they are essentially identical (Brincker and Ventura, 2015) and the terms are used here interchangeably. The correlation function is used to characterise Gaussian-distributed stochastic processes (Melsa and Sage, 1973) and represents a statistical measure of the similarity between a signal with a time-shifted version of itself (auto-correlation) or between two signals that are shifted in time relative to one another (cross-correlation) (Bendat and Piersol, 1980). For two correlated continuous-time signals $x_1(t)$ and $x_2(t)$, an unbiased estimate of the correlation function is defined as follows:

$$\hat{\Lambda}_{12}(\tau) = \frac{1}{T - |\tau|} \int_0^T x_1(t) x_2(t + \tau) dt \tag{2.25}$$

Where the correlation function $\Lambda_{12}(\tau)$ is a function of a time variable τ which describes the relative shift between the continuous-time signals. Eq. 2.25 represents a mathematical operation called a convolution integral which, in basic terms, involves the "mixing" of the signals $x_1(t)$ and $x_2(t)$ (Brandt, 2011). The continuous-time definition in Eq. 2.25 may be extended to a discrete-time definition as follows:

$$\hat{\Lambda}_{12,i} = \frac{1}{N-i}\sum_{k=0}^{N-i} x_{1,k}x_{2,k+i}^{T} \tag{2.26}$$

In Eq. 2.26 the subscript i represents the shifted discrete-time instant (equivalent to τ)) in the continuous-time case and k represents a specific a sequence $k = 1, 2, 3, 4, ...\infty$ similar to the continuous-time variable t. For multiple correlated signals, the stochastic process is characterised by a correlation function matrix:

$$R_{ij}(\tau)\begin{pmatrix} \Lambda_{11}(\tau) & \Lambda_{12}(\tau) & \cdots & \Lambda_{1n}(\tau) \\ \Lambda_{21}(\tau) & \Lambda_{21}(\tau) & \cdots & \Lambda_{2n}(\tau) \\ \vdots & \vdots & \vdots & \vdots \\ \Lambda_{n1}(\tau) & \Lambda_{n2}(\tau) & \cdots & \Lambda_{nn}(\tau) \end{pmatrix} \tag{2.27}$$

In Eq. 2.27, $R_{ij}(\tau) \in \mathbb{R}^{n\times n}$ is the continuous-time correlation function matrix. Although the matrix in Eq. 2.27 appears two-dimensional, it is important to remember that the correlation function matrix is itself a function of the time-shift variable τ. The i^{th} row of the correlation function matrix holds n correlation functions between the i^{th} output signal and every other output signal $j = 1, 2, 3, ...n$ including itself.

The correlation function has an equivalent representation in the frequency-domain called the spectral density, $G_{ij}(\omega)$ which is obtained by applying the Fourier Transform to the correlation function:

$$G_{ij}(\omega) = \int_{-\infty}^{\infty} R_{ij}(\tau)e^{-j\omega t}d\tau \tag{2.28}$$

Similarly, for multiple signals a spectral density matrix containing auto- and cross-power spectral densities may be constructed as follows:

$$G_{ij}(\omega) = \begin{pmatrix} G_{11}(\omega) & G_{12}(\omega) & \cdots & G_{1n}(\omega) \\ G_{21}(\omega) & G_{21}(\omega) & \cdots & G_{2n}(\omega) \\ \vdots & \vdots & \vdots & \vdots \\ G_{n1}(\omega) & G_{n2}(\omega) & \cdots & G_{nn}(\omega) \end{pmatrix} \tag{2.29}$$

2.4.2 OMA philosophy

An illustration of the OMA philosophy is presented in Figure 2.2 (Brincker and Ventura, 2015). The main idea is that inputs to the system that is being identified are white noise quantities. However, since the system inputs are not really random quantities with these specific characteristics, the system is conceptualised as

consisting of two parts. A (linear, time-invariant) structural filter which changes the frequency content to the white noise input such that the output is consistent with the actual system inputs to the physical system. The outputs of the physical system are then measured and used to identify the unknown modal parameters. The implication of introducing the structural filter is that the overall dynamic properties will be a combination of the system itself and the characteristics of the structural filter. It can further be shown that the physical poles are not biased by this assumption (James and Carne, 1995; Andersen and Dohler, 2017).

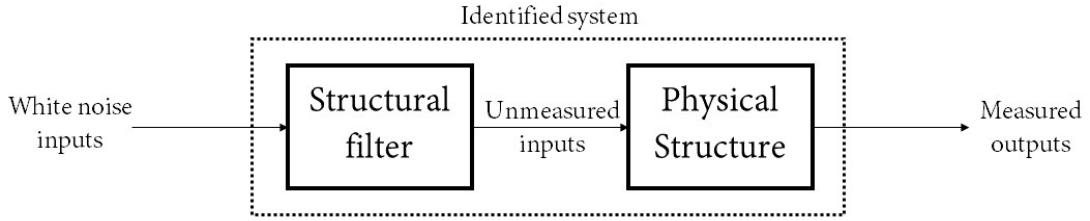

Figure 2.2: Illustration of the OMA philosophy.

2.4.3 Identification techniques

In system identification, identification techniques refer to algorithms that are used to identify the unknown parameters in a mathematical model of a system (Ljung, 1987). In OMA, this specifically relates to the identification of modal parameters. A very important requirement for modal analysis algorithms is the ability to deal with multiple inputs (to build a modal model for a multiple-degree of freedom model). Therefore, significant attention has been devoted to developing algorithms that efficiently deal with multiple outputs. For an overview of some of these methods see, for example, Brincker and Andersen (2015), Keshmiri and Mesjidian (2009) and Magalhaes and Cunha (2011). More detailed background and explanations are provided by Reynders (2012) and (Zabel, 2018).

Some of the most common techniques used in OMA are summarised in Figure 2.3. A distinction is made between time-domain and frequency-domain and between parametric versus non-parametric methods. Parametric methods essentially involve identifying a limited number of unknown parameters, such as the system matrices of the continuous-time state space model, from measurements using some sort of "fitting" technique (Reynders, 2012). Non-parametric methods involve estimating the unknown parameters directly from measurements. A simple example of a non-parametric technique is picking points in measured spectra to estimate natural frequencies.

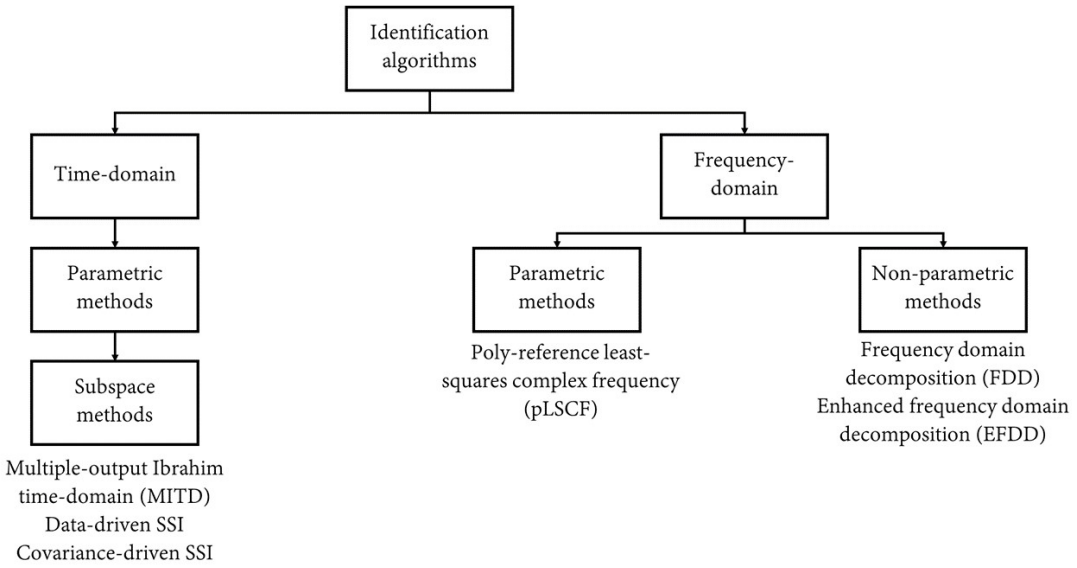

Figure 2.3: Categorisation of different identification algorithms for operational modal analysis.

Various frequency-domain methods are described in detail by, for example, Cauberghe (2004) and Pintelon and Schoukens (2001). Examples of popular frequency-domain techniques are the non-parametric frequency-domain decomposition (FDD) (Brincker *et al.*, 2000) and enhanced frequency-domain decomposition (EFDD) techniques (Ventura *et al.*, 2001) which involves estimating natural frequencies and mode shapes (and damping in the case of EFDD) from the spectral density matrix of a structure. Poly-reference least-squares complex frequency (pLSCF) is commonly used parametric frequency-domain method (Peeters and Van Der Auweraer, 2005). One limitation of the pLSCF method is that biases are obtained in damping estimates when inputs are contaminated with noise (Boswald, 2016).

Subspace methods refer to a collection of algorithms where a singular value decomposition (SVD) is used to compress data and reduce noise. Many subspace methods originated in control and electrical engineering and were developed to produce asymptotically unbiased estimates of identified parameters (Reynders, 2012). Subspace methods have a solid mathematical basis and were formulated to be implemented using robust numerical tools. Examples of subspace algorithms used in OMA are data-driven stochastic subspace identification (SSI-data) and covariance-driven stochastic subspace identification (SSI-cov) (van Overschee, P; de Moor, 1996; Peeters and de Roeck, 1999). Furher, the multiple-output Ibrahim time-domain (MITD) method is very similar to SSI-cov. These methods have been found to produce similar results (Peeters and de Roeck, 1999). Subspace identifica-

tion techniques were first used to detect structural damage by Peeters (2000) and a statistical framework by which minimum damage may be detected is described by Mendler *et al.* (2019). Further, uncertainties may be estimated for modal parameter estimates obtained using both SSI-data and SSI-cov (Dohler and Mevel, 2013; Reynders *et al.*, 2016). This involves a sensitivity analysis where variances are propagated from block Hankel data matrices through to modal parameters.

There are several sources of open-source code that implement OMA identification techniques. For example, there is the Abravibe toolbox for experimental modal analysis and signal processing by Brandt (2013) that provides source code to implement the MITD technique. An OMA toolbox by Brincker and Ventura (2015) provides algorithms for many OMA identification techniques presented here. openSID by Soal (2018) is a open-source toolbox available on Github designed specifically for OMA applications using the SSI-cov and SSI-data techniques. Further, there are a number of closed commercial software packages that may be used for OMA, most notably from companies called LMS Siemens and ARTeMIS. LMS Siemens implements a variation of the pLSCF method called Operational PolyMax (Peeters and Van Der Auweraer, 2005), while ARTeMIS applies a variety of techniques including FDD, EFDD, SSI-cov and SSI-data (Goursat *et al.*, 2010).

2.5 Automated modal analysis

In recent years considerable research attention had been devoted to developing automated modal analysis procedures. Broadly speaking, there are two main applications for automated modal analysis:

1. Selecting a subset of modal parameter estimates to build a modal model from a larger set of estimates containing both spurious (non-physical) and physical poles. This involves a single data set.

2. Comparing results from multiple data sets and matching similar modes to one another.

The first application is motivated by the fact that parametric modal identification algorithms often result in the identification of both physical and non-physical poles (this will be discussed in more detail in subsequent sections) and the user is tasked with making judgements regarding the selection of the final modal model (Lau *et al.*, 2007; Lanslots *et al.*, 2004). This can be a very time-consuming process and often inconsistencies are introduced due to differing opinions regarding the "correct" selection of modal estimates. The second research application involves the "tracking" of modes across different data sets and is especially useful

for, for example, structural health monitoring (Peeters, 2000; Zabel, 2018). Various studies on, for example, bridges (Magalhaes and Cunha, 2011; Caetano *et al.*, 2009; Marrongelli *et al.*, 2017), high-rise buildings (Sarlo *et al.*, 2018), ships (Soal *et al.*, 2019*a*), lighthouses (Nord *et al.*, 2019) and airplanes (Jelicic and Schwochow, 2015) have applied this type of automated modal analysis process.

The automated modal analysis process relating to the first application essentially consists of four basic steps, as shown in 2.4. The first is identification using one of the algorithms described in the previous section. The second, third and fourth steps are discussed in detail in the following sections.

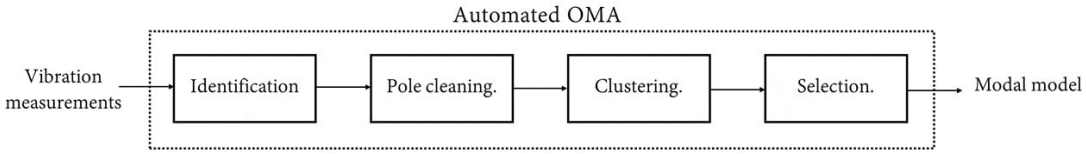

Figure 2.4: Flow diagram showing the typical process involved with automated modal analysis.

2.5.1 Pole cleaning

Common to almost all parametric methods is the specification of a parameter known as the "model" order, which basically relates to the maximum number of modes that can be identified from measured data. Since the actual number of modes is not usually known a priori, the model order is overspecified (Lau *et al.*, 2007). This results in a large number of poles, some of which are physical while others are "noise" poles, modelling both measurement and model noise. The user is often tasked with separating the physical and non-physical poles. A useful tool to aid this process is the so-called "stabilisation" diagram. The idea is to repeat the identification process for several model orders and plotting the natural frequencies of the poles at each model order, as shown in Figure 2.5. The physical poles are identified as the poles with natural frequencies, damping ratios and eigenvectors which do not change much from one model order to the next. These are called "stable poles. All poles, with the associated eigenvectors, identified at model order k are compared to the modal parameters identified at model order $k-1$:

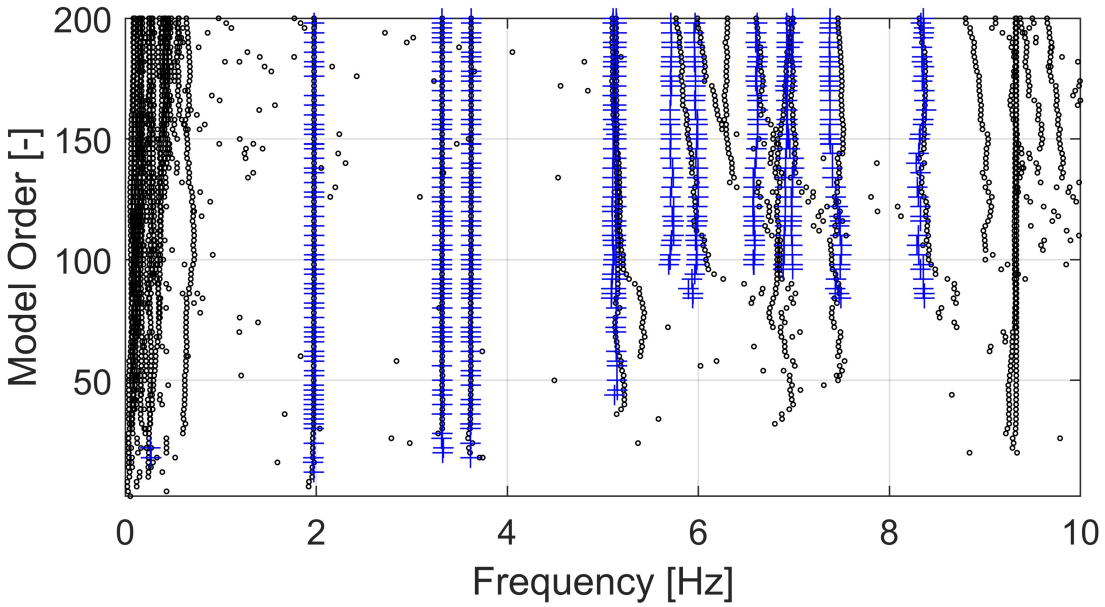

Figure 2.5: Example of a stabilisation diagram with stable + and unstable poles o.

$$\frac{|f_k - f_{k-1}|}{f_{k-1}} \leq \delta f, \quad \frac{|\zeta_k - \zeta_{k-1}|}{\zeta_{k-1}} \leq \delta\zeta, \quad MAC(\psi_k, \psi_{k-1} \geq M \tag{2.30}$$

Here f_k, ζ_k and ψ_k represents the natural frequency, damping ratio and eigenvector associated with a specific pole at model order k. The "MAC" function in Eq. 2.30 is called the modal assurance criterion and is defined as follows:

$$MAC(\psi_i, \psi_j) = \frac{(|\psi_i|^T|\psi_j|)^2}{(|\psi_i|^T|\psi_i|)(|\psi_j|^T|\psi_j|)} \tag{2.31}$$

The MAC value is a measure of orthogonality between two eigenvectors. Different modes should be orthogonal to one another (Maia and Silva, 1997) and the MAC value should be low. The same mode, however, is expected to have high similarity (and low orthogonality) and the MAC value should be high. MAC values for different modes are often visualised using MAC matrices, Figure 2.6. An cross-MAC is presented in Figure 2.6a which represents comparison of five different with themselves (diagonal entries) and each other (off-diagonal entries). High similarity occurs where modes are compared to themselves, but low when compared to each other. Similarly, an auto-MAC matrix comparing different samples of the same mode is presented in Figure 2.6b. High similarity is observed for all entries. Stable

poles are indicated with blue squares in Figure 2.5 and the stabilisation diagram can be cleaned by ignoring poles that do not satisfy the stabilisation criteria.

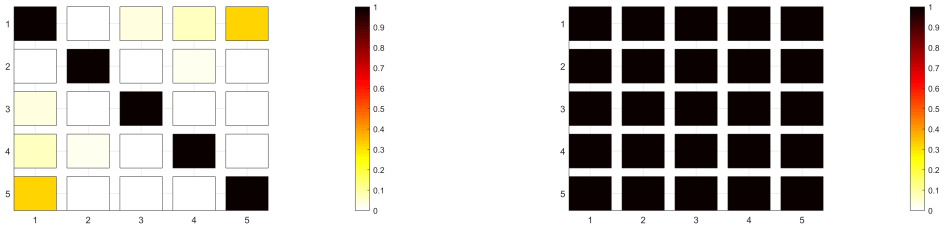

(a) (b)

Figure 2.6: Examples of (a) cross-MAC and (b) auto-MAC matrices to compare eigenvectors.

2.5.2 Clustering

Once unstable poles have been removed, modal parameter estimates are usually clustered. Cluster analysis generally refers to the grouping of objects based on certain inherent characteristics (Hair *et al.*, 2014). This means that within clusters there is high similarity, while across between different clusters there is low similarity. Figure 2.7 presents a very simple cluster analysis which involves plotting the natural frequency of stable pole versus the damping. Clearly, groups or clusters of poles with very similar frequency and damping ratios are identifiable. Some clusters have greater spread than others and typically outliers (represented by random scatter) exist even after pole cleaning. The aim of clustering is to produce groups of estimates that each represent a physical mode of interest.

There are various sophisticated clustering techniques that involve hierarchical and non-hierarchical clustering methods (Hair *et al.*, 2014). A concise overview of different clustering methods for automated modal analysis is provided by, for example, Hasan *et al.* (2019) with more detailed explanations of non-hierarchical clustering techniques available from (Caetano *et al.*, 2009). Studies involving hierarchical clustering techniques for long-term monitoring of bridges (Caetano *et al.*, 2009; Magalhaes and Cunha, 2011; Marrongelli *et al.*, 2017) and buildings Sarlo *et al.* (2018) have successfully applied clustering techniques to perform online modal analysis. Examples of non-hierarchical clustering techniques, such as k-means (Verboven *et al.*, 2002) and fuzzy-C clustering (Goethals *et al.*, 2004) are further available in literature.

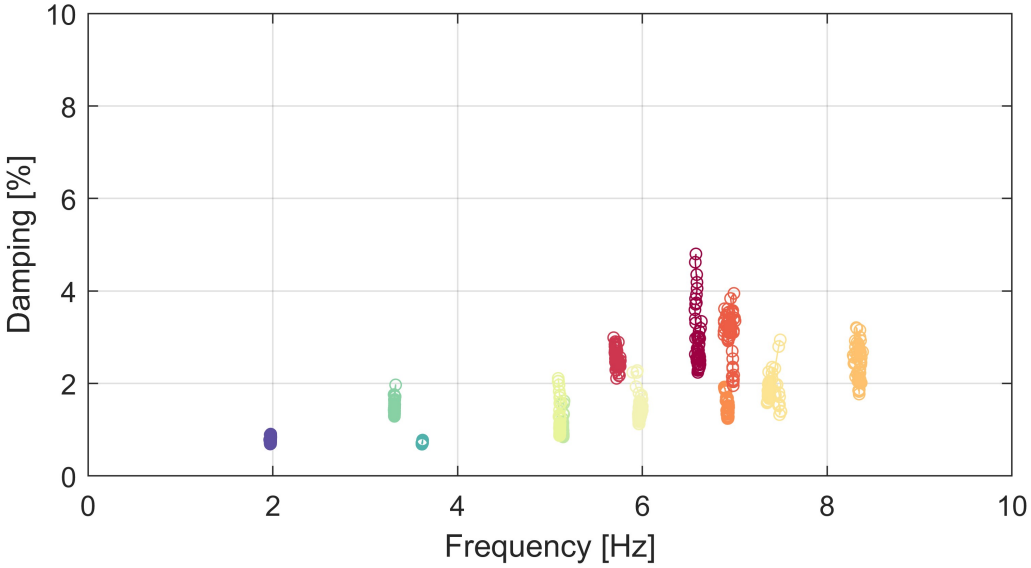

Figure 2.7: Example of clustering.

2.5.3 Selection

The final step in automated modal analysis is to select a single representative estimate from every cluster to build the final modal model. A rather simple automated selection process involves developing algorithms that imitate the decision-making process followed by expert analysts when choosing poles from a stabilisation diagram (Lanslots *et al.*, 2004). When conducting online-monitoring of wing flutter Jelicic and Schwochow (2015) selected poles from clusters that were identified at five consecutive model orders below some user-specified maximum. More sophisticated machine-learning algorithms have been tested to extract optimal estimates of modal parameters from clusters (Volkmar *et al.*, 2019; Soal *et al.*, 2019*c*). These studies used the difference between measured and synthesised spectra as a cost function to compare different combinations of mode parameters that were chosen by the selection algorithms.

2.5.4 Mode tracking

Mode tracking involves the grouping of modal parameters from multiple data sets, but in principle is similar to the automated modal analysis procedures described in the previous section. The main idea is that modes from one data set needs to be compared to modes from other data sets and similar modes are grouped together. The groups of modes formed from different data sets are called mode families. A very simple, but useful, technique was used by Jelicic and Schwochow (2015) for

online monitoring of air-plane flutter modes, and was further successfully applied to track modes of ship structures (Soal, 2018; Soal *et al.*, 2019*a*). This technique compared modes from different mode sets using the extended modal assurance criteria (MACXP) (Vacher *et al.*, 2010).The MACXP is defined as follows:

$$MACXP(\psi_i, \lambda_i, \psi_j \lambda_j) = \frac{(\frac{\psi_i^* \psi_j}{\lambda_i + \lambda_j} + \frac{\psi_i^T \psi_j}{\lambda_i + \lambda_j})^2}{(\frac{\psi_i^* \psi_i}{|\mathrm{Re}(\lambda_i)|} + \frac{\psi_i^T \psi_i}{2|(\lambda_i)|})(\frac{\psi_j^* \psi_j}{|\mathrm{Re}(\lambda_j)|} + \frac{\psi_j^T \psi_j}{2|(\lambda_j)|})} \tag{2.32}$$

In Eq. 2.32, Re() represents an operator that outputs only the real part of a complex number. The idea behind using a MAC-type value for tracking is that natural frequencies and damping ratios are likely to change across different data sets (due to changes in boundaries or system parameters themselves) but the associated mode shape will remain similar. The MACXP value is used to compare newly identified modes from a data set to some existing database of modes consisting of many mode families. The new modes are assigned to a mode family if the MACXP similarity is high otherwise a new mode family is formed if no existing family is found. MACXP tracking was found to produce improved results in the study by Soal (2018) compared to comparing only eigenvectors using the ordinary MAC. Other examples of tracking strategies may be found, for example, in Caetano *et al.* (2009); Magalhaes and Cunha (2011); Marrongelli *et al.* (2017); Sarlo *et al.* (2018).

2.6 Operational modal analysis on ships

In this section, four studies involving OMA on ship structures are reviewed. Rosenow and Uhlenbrock (2007) document one of the first successful studies where OMA was applied to a ship structure. The enhanced FDD (EFDD) (Ventura *et al.*, 2001) and covariance-driven SSI techniques were applied to sixty minutes of operational data extracted from a roll-on-roll-off (RoRo) container vessel using ARTeMIS Extractor software. Thirteen bending and torsional modes were successfully identified. The study further revealed a dependency between certain operating conditions and the identified modal parameters. Namely, increasing that ship speed results in a decrease in natural frequency and an increase in the damping ratio. OMA results in the presence of harmonic excitation was investigated and both EFDD and SSI techniques were successfully used to extract structural modes despite harmonic contamination. The EFDD technique, a non-parametric method that uses measured spectra, was used to identify sharp narrow peaks from measurements in the frequency-domain which were subsequently removed by linear interpolation. SSI was found to be robust to the presence of harmonics. Both EFDD and SSI performed better when longer measurement records were used for the identifica-

tion process. However, when harmonics were coincident with structural modes, the modal parameter estimates from both identification techniques were biased, especially damping estimates.

Orlowitz and Brandt (2014) conducted OMA on a roll-on lift-off (RoLo) vessel using measurements under different operating conditions. The study was aimed at investigating the effect of operating conditions on the identified modal parameters. Three operating conditions were considered, namely two constant speed cases (10 knots at 18 knots, respectively) and one case where the vessel was anchored in deep water. Thirty-minute time records were analysed from each case using the Multiple output Ibrahim time-domain (MITD) method. Five bending and torsional modes were identified. In agreement with the results of Rosenow and Uhlenbrock (2007), natural frequency and damping ratios were found to decrease and increase, respectively, with increasing speed. The natural frequency of vertical bending modes decreased by more than ten percent, while damping ratios of the vertical bending modes increased significantly by up to 288 percent.

Full-scale measurements were obtained from a polar vessel, the SA Agulhas II, while anchored in a harbour by Soal (2015). An OMA was conducted on the data using the frequency-domain Operational POLYMAX and time-domain SSI techniques. Three vertical bending modes were successfully identified. The natural frequencies obtained by the two methods were in close agreement (less than 1.2 percent). Damping ratio estimates differed more significantly, especially for the second vertical bending mode (59 percent). The natural frequencies were further compared to results of a finite element model (FE) model obtained from the ship manufacturer, STX Finland. Generally, the natural frequencies were lower than that reported by the ship manufacturers. This difference was attributed to a difference in the actual ship draught (6.8 m) and that assumed for the FE model (7.7 m).

Soal (2018); Soal *et al.* (2019*a*) further conducted full-scale measurements on the German polar vessel, the Polarstern, during the 2016 PS100 research expedition to the Arctic. Tracking changes in modal parameters across varying operating conditions was investigated. The frequency-domain LSCF and SSI techniques were used to extract modal parameters from measurement records of five different case studies. Seven global bending and torsional modes were successfully identified. Comparatively, the LSCF method was found to estimate fewer modes and damping estimates were generally lower than SSI. Changes in modal parameters were successfully tracked through the implementation of automatic modal selection algorithms using an extended modal assurance criterion (MACXP) (Vacher *et al.*, 2010). Modes that were not identified consistently across all cases were attributed to insufficient excitation of the mode or noise interference. Soal (2018) further observed a high statistical correlation between some modes and operational pa-

rameters such as ship speed, water temperature, air temperature, wind speed and wind direction in some of the cases. However, due to the complex nature of the relationships, there were no consistent statistical correlations that emerged from studying all five case studies. A novel method was implemented by Soal *et al.* (2019*a*) which involved combining SSI estimates with a multi-variate statistical model of operational data, using a Kalman filter. This idea was aimed at making measured data maximally informative and to reduce the effect of uncertainties in modal identification and tracking. When the proposed method was applied to full-scale measurement data for modal tracking, it was found that accurate predictions of modal parameters could be found even in the absence of SSI estimates.

2.7 Structural interactions with sea-ice

Ice loads pose a risk to ice-going vessels due to high pressures on the hull which may lead to catastrophic failure (Kotilainen *et al.*, 2017). In addition, severe ice-induced vibrations (IIVs) caused by dynamic ice loads have further been observed on various structures during ice-interactions, including ships during ice-breaking (Belov and Spiridonov, 2012). IIVs pose risks in terms of structural fatigue damage to structures and discomfort and motion sickness of human inhabitants (Pang *et al.*, 2016). As shown in Figure 2.8, peak ice loads do no typically coincide with ice-induced resonance vibrations (Bjerkas *et al.*, 2007). Therefore, IIVs are an entire field of study on its own.

2.7.1 Ice mechanics

Numerous studies on dynamic structural interactions with ice provide some key insights which are presented here. When ice interacts with a structure, the structure exerts a force that causes the ice to fail. At the same time, the ice exerts a force (with static and dynamic components) on the structure (usually called an ice load). The magnitude and characteristics of the dynamic ice load depends on several factors such as the slope of the contacting surface (Yue *et al.*, 2007; Lu *et al.*, 2015*a*), the contact area, material properties and temperature of the ice (Lu *et al.*, 2015*b*) and relative velocity (Yue *et al.*, 2009). During ship-ice interaction, Heyn and Skjetne (2018) and Su *et al.* (2011) list three main sources of ice loads during ship-ice interaction events, namely crushing, bending and splitting. Brittle crushing failure typically occurs at high encounter speeds and is typically associated with stochastic ice load signals (Yue *et al.*, 2009). The highest ice loads exerted on structures are typically associated with brittle crushing failure (Yue *et al.*, 2009), which is driven by the non-simultaneous formation of high pressure zones in the ice and microscopic changes in the material (Jordaan, 2001). Ice-

breakers are thus usually designed with a rounded bow with wider slope angles since this increases the contact area at the ship-ice interface and favours bending failure of the ice (Yue *et al.*, 2007). Ice loads arising from bending failure start with the development of circumferential cracks followed by radial cracks (Jordaan, 2001) and have been found to contain significant periodic components(Su *et al.*, 2011).

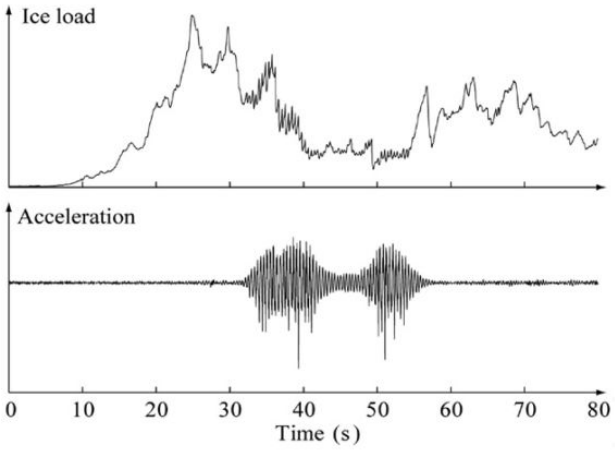

Figure 2.8: Time-histories of ice-induced resonances caused by dynamic ice loads (Bjerkas *et al.*, 2007).

Descriptions of the ice-breaking process that occurs during typical ship-ice interactions are presented by, for example, Heyn and Skjetne (2018) and Su *et al.* (2011). First, the vessel encounters a section of solid ice (such as level ice or an ice floe) and slows down due to a large horizontal ice load component. The contact area between the vessel hull is typically small and the dominant mode of ice failure is crushing. As the ship slows down, the bow rises onto the ice. With increasing contact area between the bow and the ice, the vertical component of the ice load increases. Eventually, if the vertical ice load component exceeds the bending strength of the ice, bending failure of the ice against the hull occurs. As the vessel advances, additional loads on the hull may result from pieces of ice that have broken from the ice sheet. The ice debris is forced to rotate as the vessel advances through the ice field, sliding along the hull and eventually losing contact.

2.7.2 Ice-induced vibrations

Matusiak (1982) conducted full-scale measurements on a Finnish icebreaker Sisu during ice breaking in the Gulf of Bothnia. A measurement case of approximately 30 minutes long was analysed to determine the levels of vibration associated with

ice breaking and to identify the modes of vibration associated with ship-ice interaction events. Both vessel speed and ice thickness varied throughout the measurement case and four vertical bending modes were identified. Further, two measurement records of 20 minutes long each were used to relate ice-induced vibrations with stochastic ice loads acting on the vessel hull. Vessel speed and ice thickness for the two records was 12 knots and 30 cm and 15 knots and 50 cm, respectively. The natural frequencies of the vertical bending modes were found to decrease with increasing ice thickness, which Matusiak (1982) attributed this to an increase in effective mass of the structure due to ice vibrating with the hull at the ship-ice interface. Further, damping was found to increase with increasing ice thickness due to additional damping being introduced to the system at the ship-ice interface. With lower ship speed and ice thickness ice loads were found to be higher, but due to the added damping the vibration response (amplitudes) were lower.

Since the frequency content of dynamic ice loads are affected by the dominant ice breaking mechanism (Yue *et al.*, 2007), several studies have attempted to predict ice load characteristics using the time-frequency signatures of measured IIVs. Bjerka (2006); Bjerkas *et al.* (2007) investigated the frequency content of acceleration signals obtained from a lighthouse in the Gulf of Bothnia in the Arctic using the continuous wavelet transform. The advantage of the wavelet transform is a fine frequency and time resolution can be obtained, which is important for ice interaction events that typically occur over a few seconds. Periods of intermittent crushing failure at the ice-structure interface, which caused high ice loads and significant IIVs, were identified.

In a study by Heyn and Skjetne (2018), the time-frequency signature of acceleration measurements from an icebreaker, Frej, were analysed for different cases of ship-ice interaction. A Wigner-Ville distribution which calculates instantaneous energy across different frequencies was used to predict the dominating type of ice failure mechanisms that were occurring at certain ship-ice interfaces on the hull. Further, the natural frequency of the first vertical bending mode was tracked using peaks in the Wigner-Ville distribution for specific time frames. The natural frequency mode was found to vary due to the addition of effective mass on the vessel hull during ship-ice interactions.

OMA was conducted on the Norstrømsgrund lighthouse situated in the Gulf of Bothnia (Nord *et al.*, 2019). The covariance-driven stochastic subspace identification (SSI-cov) method was used to identify natural frequencies, damping ratios and eigenvectors during recorded cases of crushing, bending, splitting and creep failure. Several modes were tracked across different observation windows of approximately ten minutes long for the different cases of failure. Larger variations in modal parameters belonging to modes with higher damping was suggested to be the result of these modes participating more in the ice-structure interaction.

Crushing and bending failure excited more modes than the other modes of ice failure. Variations in modal responses across observations windows belonging to the same ice failure mechanism were attributed to differences in ice thickness, ice-dirft direction, ice properties, air temperature and accumulation of the rubble around the structure.

2.8 Conclusion

OMA provides an output-only framework through which the modal parameters of large structures may be identified. Subspace techniques are promising candidates for modal identification and open-source code to implement both data-driven and covariance-driven SSI may be found on the platform Github. MACXP tracking, which has already been applied to other mechanical structures, including another polar vessel, is a potential tool to perform automated modal tracking on the SA Agulhas II. Ice-induced vibrations caused by ice-breaking have been studied using sophisticated signal processing techniques such as the Wigner-Ville distribution and wavelet transform. The challenge with ship-ice interactions is that the transient ice load signals act on the vessel hull over a few seconds. Therefore, analysis methods are required that capture the highly non-stationary transient ship responses due to structural interactions with ice.

Chapter 3

Full scale measurements

3.1 Vessel description

The SA Agulhas II is a multi-functional polar asset equipped with several laboratories towards the stern for oceanographic, chemical, biological, geophysical and meteorological research as indicated in Figure 3.1. The SA Agulhas II was further built with an extended transom to provide space for mounting additional laboratory containers. The main cargo-holds are located towards the bow of the vessel on Deck 3. Recreational and accommodation areas on Deck 5, Deck 6, Deck 7 and Deck 8, along with the Bridge on Deck 9 are all located in the superstructure (see Figure 3.1).

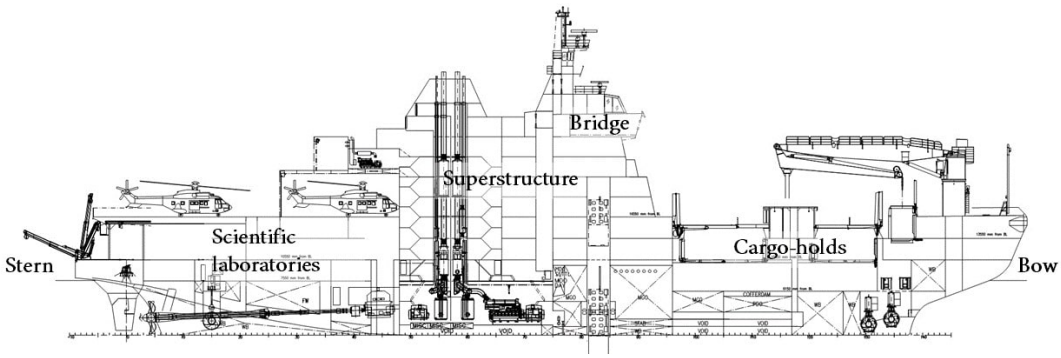

Figure 3.1: Annotated ship layout drawing showing the position of certain areas on the vessel (Finland, 2012)

.

The vessel is approximately 121.8 m between perpendiculars, with a beam and draught of 21.7 m and 7.65 m, respectively and a displacement of 13 700 tonnes. Four diesel generators provide 12 MW of power to two shaft-lines with variable pitch propellers. The ship is equipped with bow and stern thrusters for dynamic positioning. In open water the SA Agulhas II has a design speed of 14 knots. The vessel is designated a Polar Class rating of PC-5, according to the International Association of Classification Societies (2016). Further, the vessel was built with a double hull with ice strengthening equivalent to an ICE 10 vessel according to Ice Class requirements provided by De Norske Veritas De Norske Veritas AS (2016). This means that the vessel may operate in multi-year ice with glacial inclusions and in terms of ice breaking capability, the vessel is able to break through 1m ice at a constant speed of 5 knots and ice 3 m thick by backing-and-ramming. Built with a rounded bow with relatively small slope angles, the predominant ice-breaking mechanism is bending failure of the ice under the weight of the vessel.

3.2 Full-scale measurements in Antarctica

The SA Agulhas II spent the longest time at sea since her commissioning in 2012, a total of 100 days lasting from 7 December 2018 to 14 March 2019. A full voyage track is presented in Figure 3.2 and a detailed description of the voyage may be found in Appendix A.The voyage consisted of two main parts:

- The fifty-eighth annual South African National Antarctic Expedition (SANAE 58) voyage, which consisted of two legs. The first (downward) leg started on 7 December 2018 in Cape Town and ended on 31 December 2018. The second leg (return) started on 27 February 2019 with the vessel departing from Penguin Bukta to Cape Town via South Georgia, arriving on 14 March 2019. The main objectives of this part of the voyage was provide logistical support for the South African National Antarctic Programme (SANAP), transporting cargo and passengers to and from a logistics discharge point on the Antartic shelf at Penguin Bukta. A second objective was to conduct oceanographic and bio-geochemical research in the Southern Ocean led by the University of Cape Town (UCT) and Council for Scientific and Industrial Research (CSIR).

- The Weddell Sea Expedition (WSE) where the SA Agulhas II was chartered by a Netherlands-based charitable organisation called the Flotilla Foundation. The charter started on 1 January 2019 and ended on 21 February 2019. The charter objectives were to conduct oceanographic, biological and glaciological research near the Larsen C ice shelf in the Weddell Sea and to locate the 100 year old wreck of Sir Ernest Shackelton's ship, the Endurance.

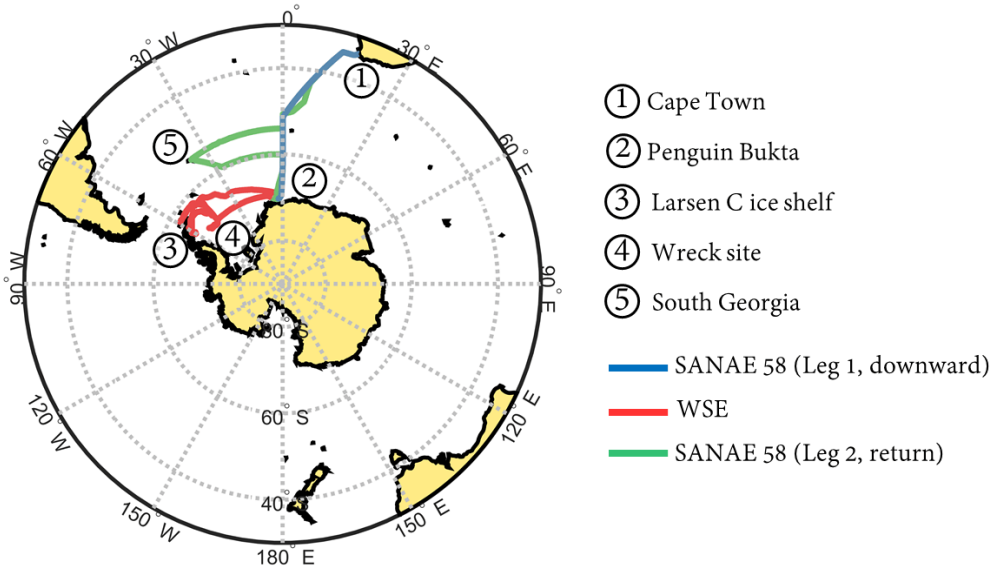

Figure 3.2: The voyage track for the two legs of the SANAE 58 voyage and WSE.

During the expedition the vessel encountered diverse, highly challenging operating environments ranging from open water storms in the Southern Ocean with swells exceeding 10 m in height to highly concentrated, multi-year ice in the Weddell Sea. Large varations in air and water temperature were encountered by the vessel as the ship moved from sub-tropical waters towards the South Pole. In addition, the ship was loaded with heavy cargo on the first leg of the voyage which was offloaded at Penguin Bukta in Antarctica between 21 and 27 December 2018. This resulted in significant changes in mass distribution (and possibly stiffness of the ship around the cargo-holds). All these changes are likely to produce noticeable variations in the vibration response of the ship.

3.3 Description of measurement systems

3.3.1 Vibration measurements

Full scale vibration measurements were conducted on the SA Agulhas with an accelerometer network consisting of twenty-eight accelerometers. Vertical acceleration of the hull was measured with fourteen accelerometers located on both the port and starboard side and distributed along the length of the vessel. Lateral hull vibration was captured by two accelerometers located at the extreme ends of the ship, one on the starboard side at the stern and one on the centreline at the bow.

A single accelerometer measured longitudinal vibration of the hull and was located at the stern. The remaining sensors monitored acceleration in the superstructure, close to the accommodation areas and recreational spaces and in the Bridge. A combination of ICP and DC accelerometers were used. All accelerometers were mounted using superglue and sensors in the hull were placed on structural elements such as beams and girders to capture mainly the global structural vibrations of the vessel. Accelerometer locations are presented in Figure 3.3 and a channel table is provided in Table 3.1.

Twenty-one coaxial BNC cables are permanently routed along cable trays to all the measurement locations on the vessel, except those located in the steering gear room (namely, Channel no. 1 to 14 and 17 to 24 in Table 3.1). The coaxial BNC cables have unique identifiers and are assigned to a specific accelerometer (see Table 3.1). Each accelerometer is connected to the corresponding coaxial BNC cable with a noise-cancelling coaxial ICP-BNC cable. The opposite ends of the coaxial BNC cables are routed to a central location in the engine store room where voltage signals from the accelerometers were captured by a data acquisition setup that was designed within the Sound and Vibration Research Group at Stellenbosch University as described by Bekker *et al.* (2018) and Soal (2015). Two LMS SCADAS Mobile SMO03 data acquisition (DAQ) units were installed in the engine store room as shown in Figure 3.3. Signals from the accelerometers are transmitted via the coaxial BNC cables to specific channels on the "master DAQ" and "slave DAQ 1" as indicated in the column "DAQ Channel" in Table 3.1. A third LMS SCADAS Mobile SM03 unit is located in the steering gear room of the vessel, "slave DAQ 2". Slave DAQ 2 is connected to the accelerometers at the stern (Channel no. 25 to 30 in Table 3.1) via noise-cancelling coaxial ICP-BNC cables. The three DAQ units are connected in a master-slave configuration via fibre optic cable such that all measurements are perfectly synchronised and belong to the same measurement project in the data acquisition software. The fibre optic cable extending between the engine store and steering gear room is a permanent installation and is routed along cable trays through water tight openings in inner walls of the vessel. The master DAQ interfaces with LMS Test Lab Turbine Testing software via an ethernet connection with a laptop computer mounted in the engine store room. Photographs showing examples of accelerometers measuring structural vibration and the data acqusition setup are presented in Figure 3.4. All measurements are sampled continuously at 2048 Hz and are stored on the laptop computer in 5 minute ".ldsf" formatted files.

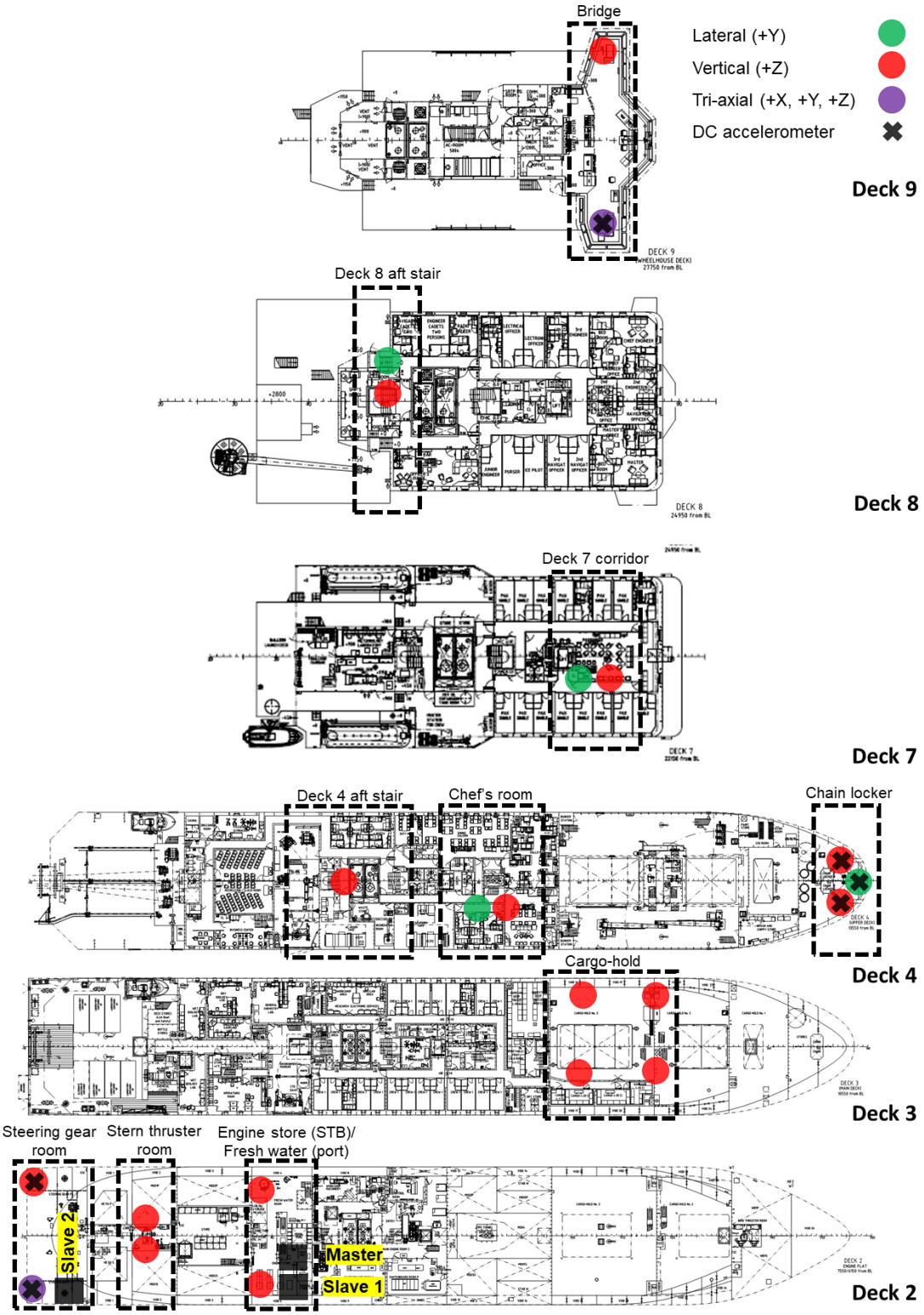

Figure 3.3: Accelerometer network on the SA Agulhas II.

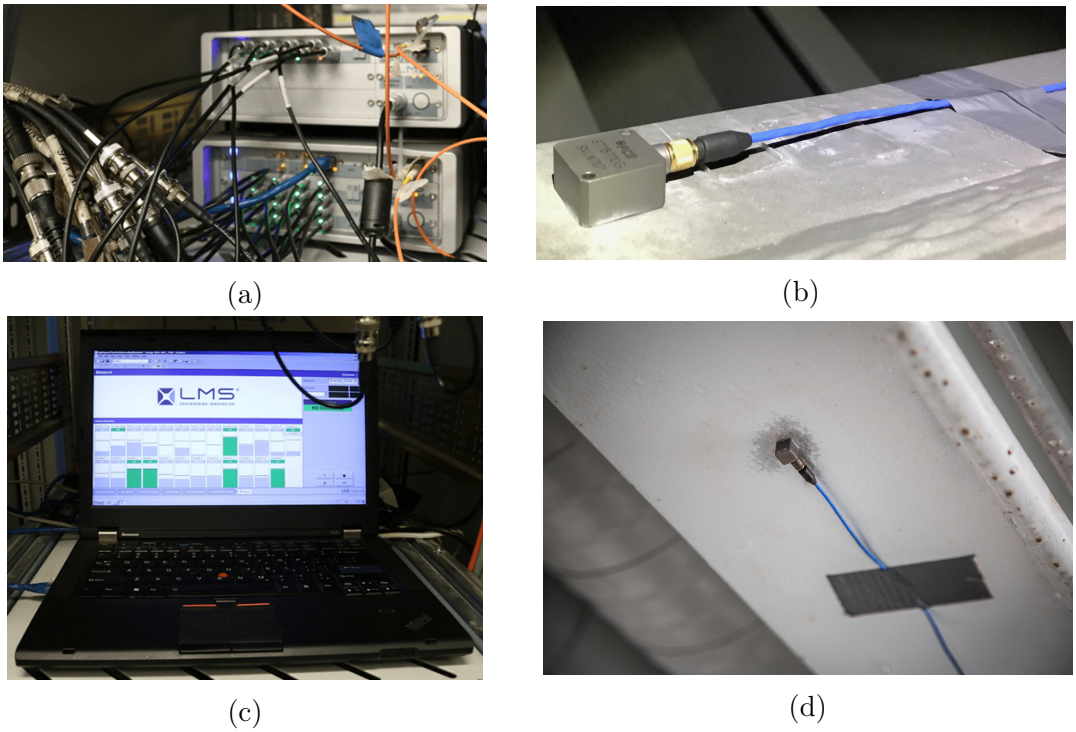

(a) (b)

(c) (d)

Figure 3.4: Photographs of measurement equipment showing a) the Master LMS SCADAS DAQ installed in engine store room b) a DC accelerometer mounted in the steering gear room c) the measurement laptop running LMS Test Lab Turbine Testing software in the engine store room d) an ICP accelerometer mounted in the engine store room.

3.3.2 Measurements of environmental conditions and ship operational parameters

In addition to vibration measurements, a separate system recorded several ship operational parameters and environmental conditions. This system is permanently installed on the ship and was initially used during the ice trials in the Baltic Sea when the vessel was commissioned Bekker *et al.* (2017). Measurements are accessible through a desktop computer located in the engine store room of the ship and are stored in binary format every few minutes. Some details of the measurements available from this system are presented in Table 3.2.

Table 3.1: Channel table for full-scale vibration measurements

Channel #	Location	Deck	Direction	Type	Sensitivity $[mV/(m/s^2)]$	DAQ/Channel	Cable
1	Bridge (starboard)	9	X	DC	20.19	Master/1	V14
2	Bridge (starboard)	9	Y	DC	20.22	Master/2	V15
3	Bridge (starboard)	9	Z	DC	20.13	Master/3	V16
4	Bridge (port)	9	Z	ICP	10.03	Master/4	V17
5	Deck 8 aft stairs	8	Y	ICP	10.2	Master/5	V18
6	Deck 8 aft stairs	8	Z	ICP	10.06	Master/6	V19
7	Deck 7 corridor	7	Y	ICP	10.03	Master/7	V12
8	Deck 7 corridor	7	Z	ICP	10.13	Master/8	V13
9	Bow (chain locker starboard)	5	Z	DC	20.24	Master/9	V1
10	Bow (chain locker centre)	5	Y	DC	20.29	Master/10	V2
11	Bow (chain locker port)	5	Z	DC	20.46	Master/11	V3
12	Deck 4 chef's room	4	Y	ICP	10.13	Master/12	V9
13	Deck 4 chef's room	4	Z	ICP	9.96	Master/13	V9
14	Deck 4 aft stairs	4	Z	ICP	10.05	Master/14	V10
15	-	-	-	-	-	-	-
16	-	-	-	-		-	-
17	Cargo-hold (fore starboard)	3	Z	ICP	9.7	Slave1/1	V4
18	Cargo-hold (fore port)	3	Z	ICP	10.25	Slave1/2	V5
19	Cargo-hold (aft port)	3	Z	ICP	10.23	Slave1/3	V7
20	Cargo-hold (aft starboard)	3	Z	ICP	10.44	Slave1/4	V6
21	Engine store room	2	Z	ICP	10.43	Slave1/5	*unlabelled*
22	Fresh water room	2	Z	ICP	10.42	Slave1/6	RGB84
23	Stern thruster room (starboard)	1	Z	ICP	10.34	Slave1/7	V20
24	Stern thruster room (port)	1	Z	ICP	10.36	Slave1/8	V21
25	Steering gear room (starboard)	2	X	DC	20.23	Slave2/1	-
26	Steering gear room (starboard)	2	Y	DC	20.23	Slave2/2	-
27	Steering gear room (starboard)	2	Z	DC	20.29	Slave2/3	-
28	Steering gear room (starboard)	2	Y	ICP	10.39	Slave2/4	-
29	Steering gear room (starboard)	2	Z	ICP	10.45	Slave2/5	-
30	Steering gear room (port)	2	Z	DC	20.31	Slave2/6	-

Table 3.2: Summary of additional ship operational variables.

Measurement system	No. of channels	Sample rate	Variables
Machine control	16	1 Hz	Propulsion motor current , propulsion motor power , propulsion motor speed, propulsion motor voltage, rudder order, rudder position, propeller pitch, propeller shaft speed.
Navigation	9	0,5 Hz	Time, latitude, longitude, speed over ground, course over ground, HDT, relative wind direction, wind speed, depth.

3.3.3 Ice observations

During ice navigation, round-the-clock visual ice observations were conducted in three to four hour surveillance shifts twice daily per observer. All visual observations were performed on the Bridge of the vessel (see Figure 3.5a). As the ship navigated through ice, breaking up pack ice and ice floes, broken segments of ice were rotated ninety degrees against the vessel hull making it possible to estimate the thickness of the ice. A yardstick (1.5 long) with black and white markings

spaced 10 cm apart was used as a reference to estimate the thickness of the broken ice, Figure 3.5b. The observer on shift was tasked with recording minute-by-minute estimates of the ice thickness (in cm), ice concentration (0 to 100 percent) and floe size (in m) in an Excel spreadsheet. The minute-by-minute observations were then used to calculate a ten minute average of the ice conditions. Further, for every ten minute observation period, the observer had to judge how much of the ice concentration recorded was brash ice (broken up pieces of ice) compared to solid pack ice and was asked to rate their experience of the size of vibrations felt on the Bridge. Ice passage started during the downward leg of the SANAE 58 voyage at 02:00 on 15 December 2018 and ended when the vessel departed from Antarctica to return to South Africa via South Georgia. In total, approximately 1640 ten minute averages were recorded in the Excel spreadsheet, equivalent to almost 275 hours of continuous ice observations.

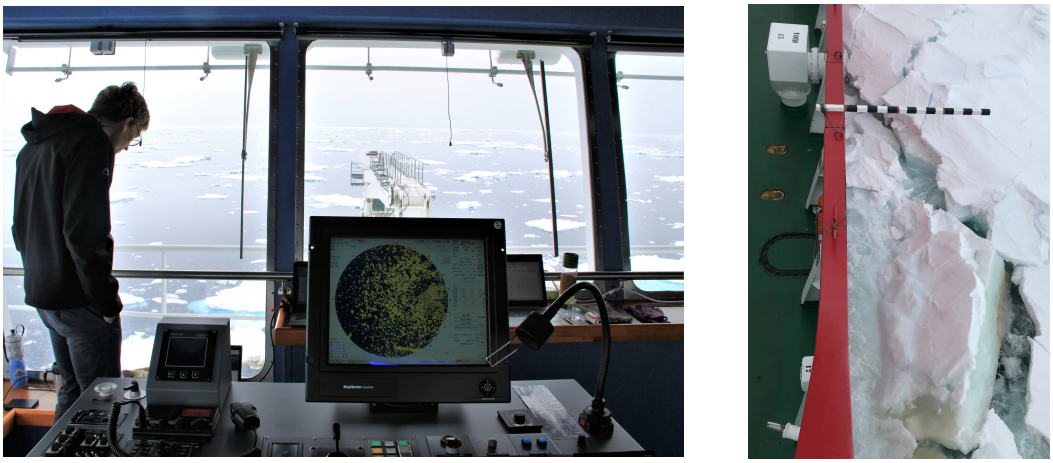

(a) (b)

Figure 3.5: Photographs showing (a) the ice observer on shift performing visual observations of ice conditions from the Bridge and (b) the yardstick used to estimate ice thickness.

3.4 Data veracity

Continuous recording of vibration from twenty-eight channels at a sample rate of 2048 Hz generates large volumes of data (around 20 GB per day). An important aspect of dealing with large data sets such as these is that the quality or "veracity" of recorded data is verified (Lovoll and Kadal, 2014). In the present context, data veracity can be thought of as how representative the recorded vibration data is of

the physical phenomena of interest, namely the global structural vibration of the vessel.

During the voyage a protocol was developed which involved routine inspections of the quality of measured vibration data. This procedure is inspired by basic principles discussed by Brandt (2011) and which has been used for assessing vibration data quality in previous studies on ship structures (Soal, 2018). In-house MATLAB scripts are then used to process the vibration data on a daily basis. The typical procedure that is followed for checking veracity of measurements is illustrated in Figure 3.6.

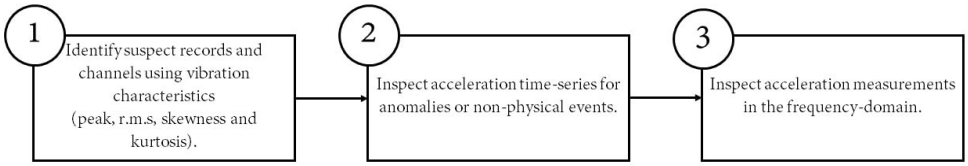

Figure 3.6: Flow chart showing the protocol followed for routine data veracity checks.

Firstly, characteristics of the vibration signals (peak, root-mean-square, kurtosis and skewness) are calculated for each five-minute record. From this perspective, it is easy to identify suspect measurement records. For example, in Figure 3.7a, measurement record three and seven contain a single channel with unusual vibration characteristics. In particular, during measurement record seven this channel has relatively high peak and r.m.s values and a kurtosis value over 800 (compared to kurtosis values across all other channels under 20). Kurtosis is a good indicator for impulsive events since in the time-domain it involves raising acceleration values to the fourth power. Large peak values are thus amplified, producing a large kurtosis value. Upon inspection, the time-series of this record contains an unusual impulsive event (indicated by the shaded red box), Figure 3.7b.

Closer inspection of the impulse reveals an event that is most likely not caused by a physical phenomenon and probably represents a voltage overload on the sensor (Figure 3.7c). Voltage overloads occur when a voltage signal is produced that is beyond the specified range on the measurement system. To protect the system from damage, the signal is "dropped" which is indicated by the sudden decrease and subsequent (more gradual) restoration of the acceleration signal. Overloads may occur due to very large acceleration events or from improper electrical connection.

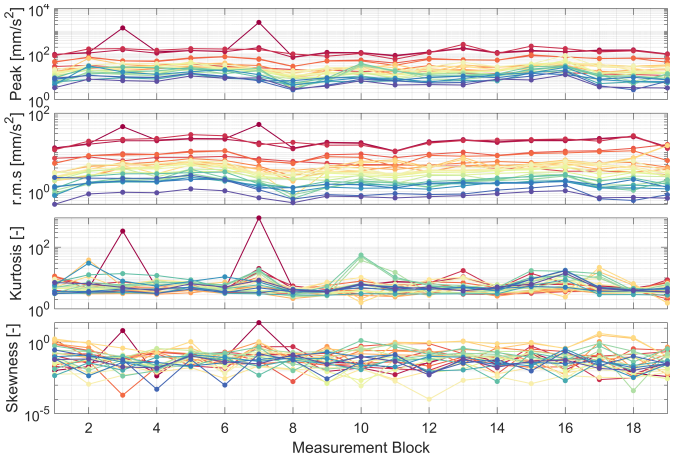

(a) Statistical indicators / metrics.

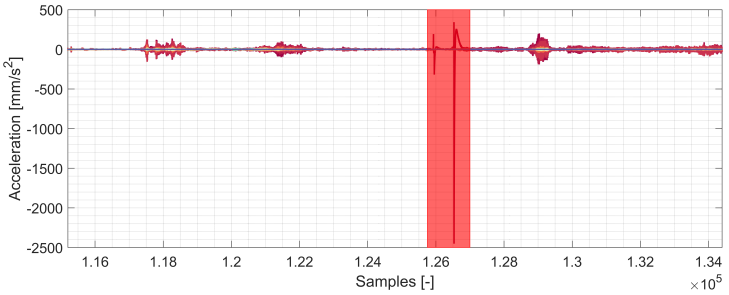

(b) Acceleration time-histories of suspect channels.

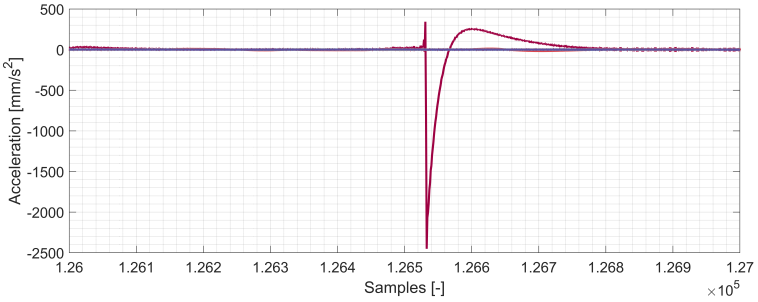

(c) Record an "overload" event on an acceleration signal.

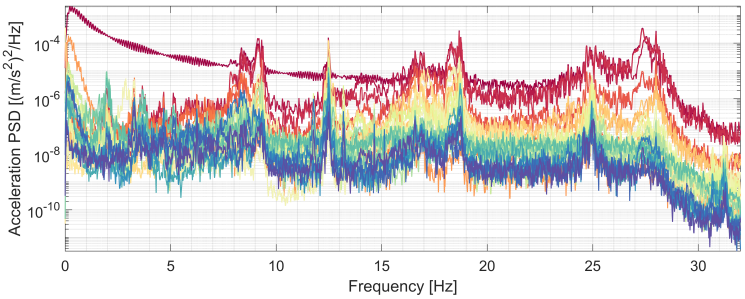

(d) Power spectral density of the suspect channel fails to capture responses accurately in the bandwidth 0 to 10 Hz.

Figure 3.7: Illustration of protocol for checking data veracity.

When the signal is inspected in the frequency-domain, it is clear that this channel fails to measure acceleration accurately below 10 Hz. This may be seen in Figure 3.7d where a single channel measures an entirely different responses to the other channels in this frequency range. Since the aim is to use acceleration signals to identify the global elastic modes of the vessel occurring in the bandwidth 1 to 10 Hz, this measurement channel is unsuitable for further analysis. This channel is flagged and if the problem persists corrective action is taken. This includes (1) checking all electrical connections on sensors and the DAQ units, (2) adjusting the voltage ranges on the measurement system to capture higher levels of vibration and (3) securing all cables and electrical connections with duct tape and cable ties.

Chapter 4

Parametric investigation

4.1 Introduction

Dynamic models of a system may be built from operational response measurements using output-only system identification principles. In civil, mechanical and aerospace engineering output-only system identification is called operational modal analysis (OMA) and the dynamics of the identified structure are described in terms of modal parameters. A powerful set of techniques for output-only system identification, which originated in electrical and control engineering, are called the stochastic subspace identification (SSI) algorithms. The development of these algorithms, which have a solid mathematical basis, was motivated by the need for asymptotically unbiased system identification algorithms for accurate control applications (Reynders, 2012). This means that increasing the number of samples or observations used in the identification, bias effectively removed from the estimates that are obtained. The theory behind the SSI techniques encompass a broad spectrum of fields including linear algebra, statistics and control theory. This means that the details relating to some of the fundamental expressions in these algorithms are often challenging to both newcomers and experts in the field of OMA. The SSI techniques further rely on the specification of user-specified parameters which influence estimates in the final modal model. The exact influence of parameters on estimates is not well understood and there are no general rules relating to the selection of the parameters that can applied to all types of structures.

Previous research on the German polar research vessel, the Polarstern, by Soal (2018) resulted in Matlab code that is freely available for download on the open-source platform, Github. This code was the starting point for implementing the data-driven SSI technique on full-scale data from the SA Agulhas II. However, in order to apply the SSI algorithms to ship data the underlying theory needed to be understood. To this end, a detailed synthesis using many different sources

explaining both fundamental concepts and more challenging details of the data-driven SSI algorithm is provided in Appendix B. Further, in this appendix the reader will find theory relating to the selection of user-specified parameters for data-driven SSI. In the following sections, a parametric study was conducted to apply the knowledge gained while delving into the details of the SSI algorithms. The objective of this study is to find suitable user-selected SSI parameters that produce accurate modal parameter estimates for the SA Agulhas II from output-only measurements.

4.2 Analysis methods

In this section, the effect of user specified SSI parameters on modal parameter estimates for operational ship data is explored. The idea is to present a framework by which modal parameter estimates can be assessed to gain insight into the selection of SSI parameters for complicated OMA structures. Figure 4.1 presents an overview of the methodology used in the investigation. First, a relatively simple non-parametric frequency-domain OMA technique called frequency domain decomposition (FDD) (Brincker *et al.*, 2000) is used to identify modes of interest. Then, the parametric investigation on data-driven SSI is conducted which starts with the selection of certain data-driven SSI parameters. Automated OMA is performed using the specified parameters in several steps including identification, pole cleaning, clustering and selection. Poles and eigenvectors identified using the automated OMA process which correspond to the modes of interest from the preliminary FDD analysis are then stored before the investigation is repeated with a different set of SSI parameters. The methods will be discussed in further detail in the following sections.

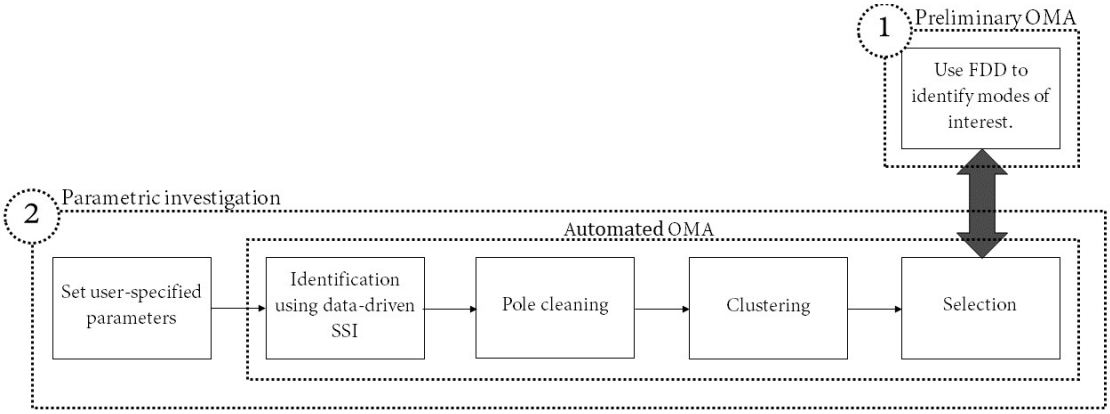

Figure 4.1: Flow diagram illustrating the method for the parametric investigation.

4.2.1 Preliminary frequency domain analysis

The main idea behind FDD is that the spectral density matrix may be transformed to modal coordinates using the mode shape matrix: (Brincker *et al.*, 2000)

$$G_{yy}(\omega_k) = \Phi G_{qq}(\omega_k)\Phi^H \tag{4.1}$$

Here $G_{yy}(\omega_k) \in \mathbb{R}^{l\times l}$ is the spectral density matrix in physical coordinates for l measurement channels at frequency line ω_k. Similarly, $G_{qq}(\omega_k) \in \mathbb{R}^{l\times l}$ is the spectral density matrix in modal coordinates. As in Chapter 2, $\Phi \in \mathbb{R}^{l\times l}$ is the mode shape matrix. The spectral density matrix in modal coordinates is a diagonal matrix (since all degrees of freedom are decoupled in modal coordinates) with each entry representing a function of frequency corresponding to a single modal coordinate. When the spectra of the modal coordinates are plotted as a function of frequency, each spectrum resembles a single degree of freedom oscillator with a peak at the natural frequency corresponding to one specific mode. In FDD, an estimate for the spectral density matrix G_{qq} is obtained by performing a singular value decomposition (SVD) on the spectral density matrix G_{yy} (Brincker *et al.*, 2000):

$$G_{yy}(\omega_k) = USU^H \tag{4.2}$$

Here $S \in \mathbb{R}^{l\times l}$ is a diagonal matrix containing the so-called singular values and $U \in \mathbb{R}^{l\times l}$ is an orthonormal matrix holding the corresponding singular vectors in its columns. From Equation B.21, a few observations may be made. Firstly, comparing the form of SVD to the form of Equation 4.1, the matrix S may be interpreted as an estimate of the spectral density matrix in modal coordinates while the matrix U is an estimate of the mode shape matrix. However, an important characteristic of the SVD is that singular values always appear in the matrix S in descending order. This means that at frequency lines coincident with or close to natural frequencies, the first singular value represents the spectral density function of the dominating modal coordinate while the remaining singular values model the contribution of other modes and noise to the measured vibration response. Further, at a frequency line corresponding to the natural frequency of a specific mode, the first singular vector is an estimate of the mode shape of that mode. In the case where two modes are closely spaced, the first singular value and vector contains information about the dominating mode while the natural frequency and mode shape of the other mode is obtained from the second singular value and singular vector, respectively.

4.2.2 Investigation of block size, duration and model order

In this study, the following three data-driven SSI parameters are investigated:

1. Block size
2. Measurement duration
3. Model order

A full subset of reference channels are used throughout. The reason for this is that it becomes difficult to track the effect of one specific parameter when variations in one parameter is likely to have a direct effect on the selection of another parameter. For example, it has been observed with ship data that using different subsets of reference channels changes the minimum block size required to identify certain modes. The investigation starts by first allowing block size to vary while measurement duration and maximum model order are kept constant:

- Varying block size, $i = 10, 20, ..., 70$.
- Constant measurement duration, $n_b = 20$ min..
- Constant maximum model order, $n_{max} = 270$.

The choice of measurement duration is based on 20 minutes producing 2400 observations of the lowest expected natural frequency (approximately 2 Hz) and is further motivated by a study by Soal (2018) in which modes were successfully tracked for a similar vessel using a 20 minute observation window. The model order was allowed to vary between 2 and 270 resulting in a total of 18360 poles and eigenvectors identified across all model orders ($2+4+...+270 = 18360$). Unstable poles were immediately removed using the following limits to compare poles from consecutive model orders: $\delta f \leq 0.01, \delta\zeta \leq 0.1, MAC(\psi_i, \psi_j) \geq 0.95$. Then modal estimates were automatically clustered using MACXP ($MACXP(\psi_i, \lambda_i, \psi_j, \lambda_j) \leq 0.95$). This means that poles (and the associated eigenvectors) with a MACXP value greater than 0.95 were grouped together. The poles and eigenvectors that correspond to the five modes identified in the FDD analysis were analysed further. Figure 4.2 provides an example of a "cleaned" stabilisation diagram which shows the clusters corresponding to the five modes of interest together with various other stable poles. It is clear that other modes could have been included in the analysis, however for the purposes of this work only the five modes identified in Figure 4.2 were considered.

This automated procedure is repeated for each block size ranging from ten to seventy and the resulting seven different cluster sets consisting of five modes are

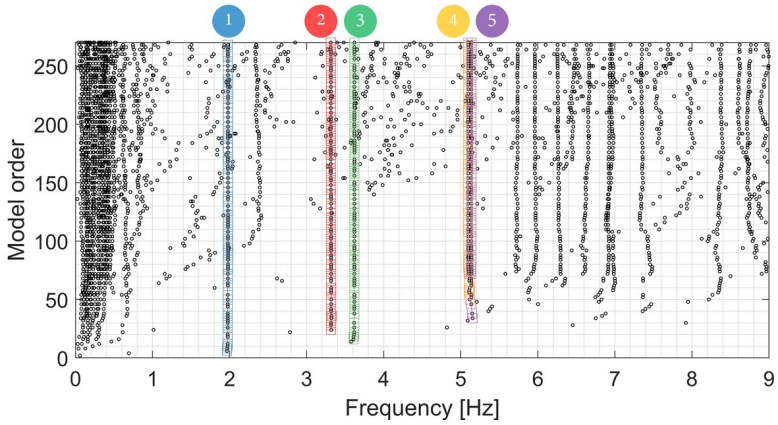

Figure 4.2: Clusters corresponding to the five modes of interest.

subjected to a statistical analysis. This means that the clusters are treated as samples or observations of the same mode for which summary statistics (mean, median, quartiles, variance, minimum and maximum) may be calculated. Therefore, although model order is allowed to vary during the investigation, the resulting clusters are treated merely as observations with no knowledge of the model orders at which the individual samples were identified. This is appropriate for investigating these parameters because the point was to identify overall trends in the behaviour of the clusters that arise solely from varying duration and block size. The summary statistics and the individual cluster values themselves are used as metrics to investigate the effect of block size. Since the "correct" value of the modal estimates are unknown, trends that arise from the variation of block size are observed to gain insight into the practical use of the data-driven SSI algorithm.

Once the block size investigation is complete, the second part of the parameter investigation involves studying effect of measurement duration on modal parameter estimates. The method is similar to that used for the block size investigation with a varying measurement duration and constant block size and maximum model order:

- Constant block size, $i = 50$
- Varying measurement duration, $n_b = 20$ min.
- Constant maximum model order, $n_{max} = 270$

The block size is based on the findings of the block size investigation. Clusters are matched to the modes of interest and are subjected to the same statistical analysis that is used for the block size investigation. Finally, investigating the model order involves fixing both the block size and measurement duration and

allowing the model order to vary between 2 and 600. After pole cleaning and clustering (using the same method as for the block size and measurement duration investigations), the clusters belonging to the modes identified in the preliminary FDD analysis are identified. The point here is to observe what happens to modal estimates at extreme model orders (low and very high) in order to avoid problems associated with selecting too low or high model orders.

4.3 Case study

The analyses presented in the subsequent sections were performed on approximately 40 minutes of data collected on the afternoon of 5 January 2019. This case study was selected as a result of stationary environmental conditions and operating parameters, see Figure 4.3. The vessel was navigated at a constant speed of about 9 knots with a constant shaft speed of about 140 rpm. The heading remained constant and the wind speed varied by less than 5 knots.

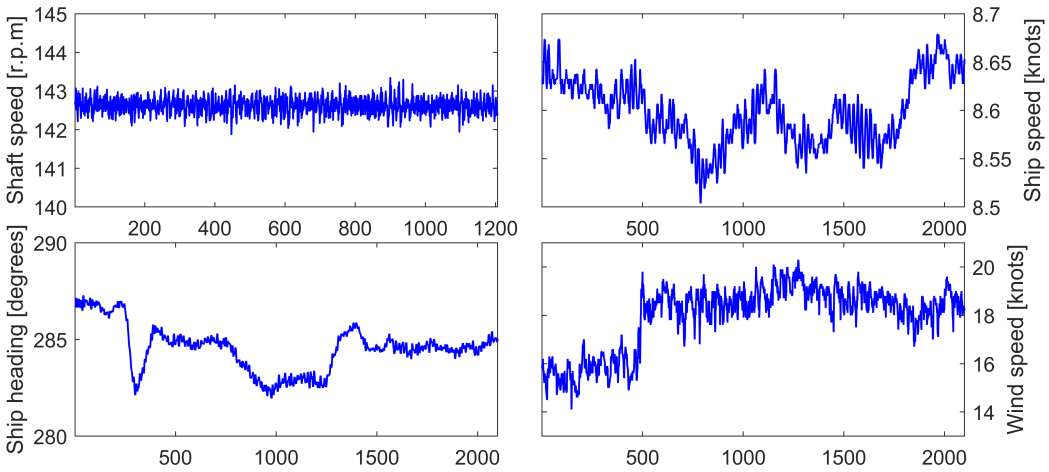

Figure 4.3: Environmental and ship operational parameters.

First, time-series measurements from twenty-seven accelerometers were detrended and decimated to 64 Hz. The time-series measurements are presented in Figure 4.4a. A noteworthy characteristic of the vibration signals are the relative stationarity of the time-series across all the measurement channels. Subsequently, cross-power spectral densities (CPSDs) were calculated between all measurement channels from the decimated time-series signals using the unbiased version of Welch, method, see Figure 4.4b. Significant low frequency vibrations below

1 Hz are attributed to the rigid body motion of the vessel and wave period. In the frequency range between 1 to 9 Hz, shown in Figure 4.4c, modal peaks may be identified that are present across most or all the measurement channels and are thought to represent the global modes of the vessel. Above 9 Hz the response measurements are dominated by the harmonics of rotating components on-board the vessel. These harmonics are represented by sharp, narrow peaks.

4.4 Results

4.4.1 Frequency domain operational modal analysis

Figure 4.5 presents a spectrum of the first four singular values of the spectral density matrix in Figure 4.4 (b). Most of the information relating to the physical structure are contained in the first two sets of singular values, including five clear modal peaks which are marked in Figure 4.5 with solid lines. The natural frequencies and estimates of the signal-to-noise ratio (SNR) are indicated by the text boxes that accompany each of the identified modes. The SNR provides an indication of how well a mode is excited to produce a response above the measurement noise floor. The SNR is calculated by taking the logarithm (base 10) of the ratio between the energy density at the modal peak (the peak in the first singular value for Mode 1, Mode 2, Mode 3 and Mode 5 and second singular value for Mode 4) and the energy density of the fifth singular value at the same frequency line scaled by factor 20 ($SNR = 20 \times \log_{10}(P_1/P_2)$)). The fifth singular value was used since it clearly contains information about only measurement noise. Possible modes are indicated by dotted lines in Figure 4.4. These modes do not have clear modal peaks for two possible reasons: (1) the modes are not excited sufficiently above the measurement noise floor and/or (2) the assumption of white noise inputs that are random in both space and time is violated. The implication of violating the "non-white" input assumption is that the mode is not excited sufficiently to produce a vibration response that can be accurately identified.

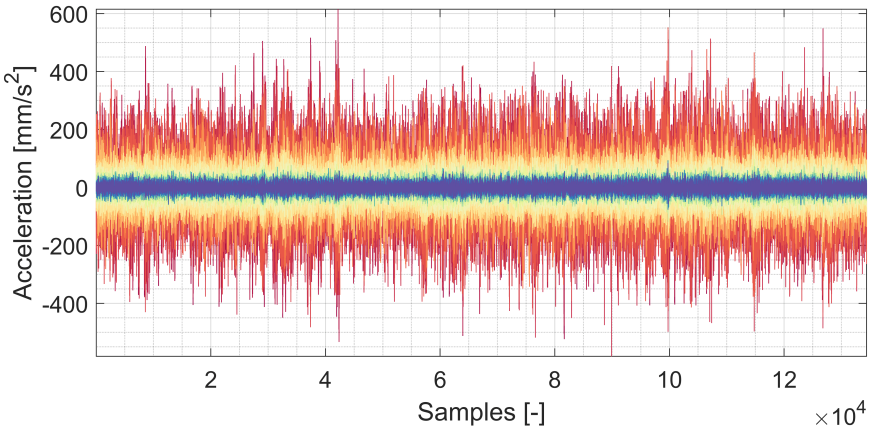

(a)

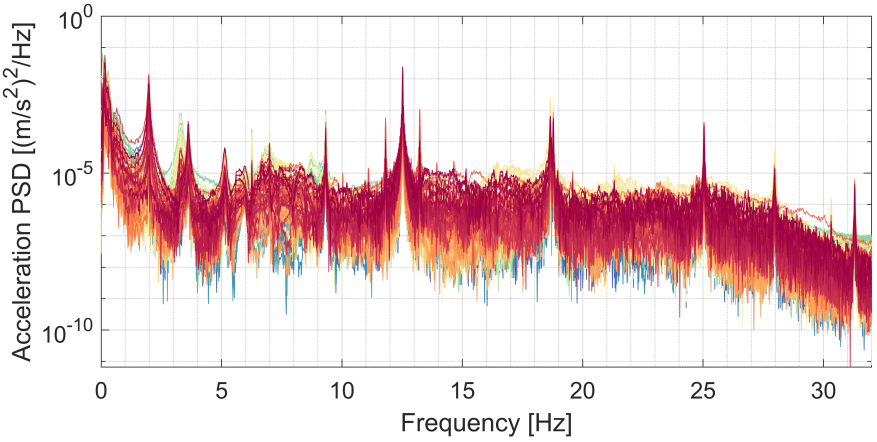

(b)

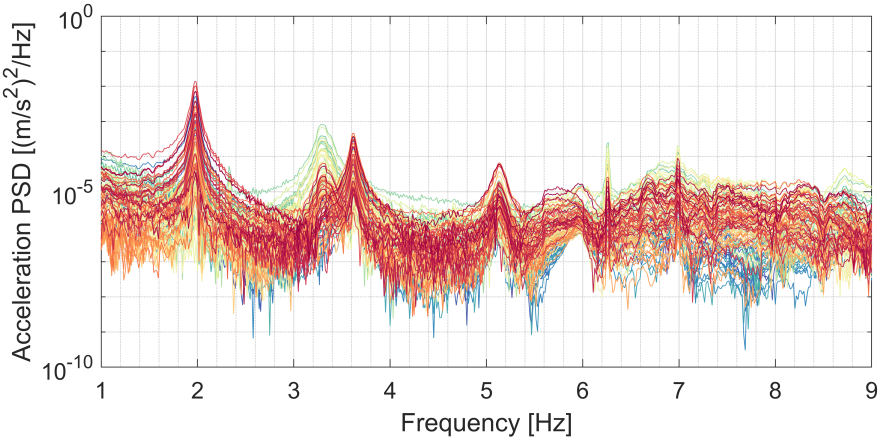

(c)

Figure 4.4: (a) Acceleration time-series (b) Acceleration cross-power spectral densities, bandwidth 0 to 32 Hz (c) Acceleration cross-power spectral densities, bandwidth 1 to 9 Hz.

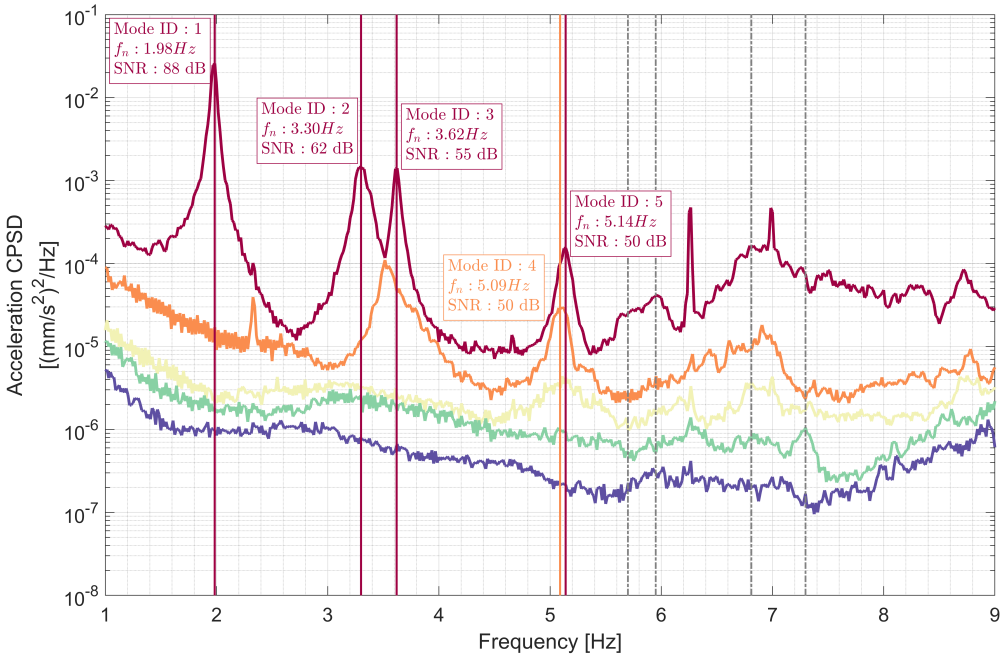

Figure 4.5: First five singular values of power spectral density matrix, bandwidth 1 to 9 Hz.

4.4.2 Block size

The effect of varying block size is presented for each mode identified during the FDD analysis in Figure 4.6. Box plots for frequency and damping show the median (solid red line), mean (green cross) and upper and lower quartile (filled blue box) values that were calculated for the clusters at different block size. The actual cluster values themselves are included in the box plots (as black dots) to show the actual spread of data which are sometimes disguised by summary statistics. (The way in which clusters are presented here as statistical quantities in box plots was inspired by the work of Soal *et al.* (2019*b*)). Further, "cluster diagrams" which show frequency clusters plotted versus damping clusters are presented for each mode. This provides a different perspective to the box plots, allowing one to visualise the convergence (or divergence) of frequency and damping estimates and easily identify outliers. In addition, for each mode and block size Table 4.1 presents the cluster size, normalized cluster variance, the minimum and maximum cluster values and percentage difference between the respective minima and maxima. The

minimum variance and percentage difference are for each mode are represented in Table 4.1 by cells filled with red. The following observations may be made:

- The first, and perhaps most important, observation is that at low block sizes certain modes are not accurately identified. This is apparent from the absence of box plots and values in Table 4.1 for Mode 4 (at block size 10 and 20) and Mode 5 (at block size 10). This means that during the clustering process, modal estimates of Mode 4 and Mode 5 were not sufficiently similar to form clusters that could be considered in the analysis. Referring back to the SNRs presented in 4.5 for the FDD analysis, the relatively low SNRs of Mode 4 and Mode 5 is likely why larger block sizes are required to identify these modes.

- Generally, there appears to be convergence of mean and median values of the frequency and damping clusters with increasing block size. Similarly, the quartile range of frequency and damping clusters appears to decrease as block size increases from 10 to 50. This indicates that in a certain range of block sizes, bias error can be reduced by increasing the block size.

- For block sizes above 50, the quartile range of frequency increases for Mode 2 and Mode 4 while the quartile range of damping clusters remains sufficiently small. This effect is clearly seen in the cluster diagrams of these modes, where the clusters seem to form a horizontal line with low variation in damping but large spread in frequency. Interestingly, this effect is observed for Mode 2 and Mode 4 which both have relatively high damping compared to the other modes.

- Concerning the actual cluster values, these may be used to gain insight into the effect of block size on random errors in modal estimates. In general, increasing block size results in fewer outliers in damping estimates with the exception of Mode 1 which has significant outliers in damping estimates for block size 70.

Intuitively it makes sense that bias can be removed by increasing block size and that there is an upper limit (or convergence) associated with the improvement of estimates. Increasing block size can be interpreted as increasing the number of observations of a free decay which may improve the accuracy of the identified poles (see Appendix B.5). However, using a similar argument it seems reasonable that increasing block size indefinitely could could produce random errors in modal estimates. This is because the dynamic signals belonging to modal responses decay to zero. This is especially true for modes with high damping (Mode 1 and Mode

3). Once the modal responses have decayed to zero, increasing the block size only includes noise in the identification, which is likely to introduce random errors.

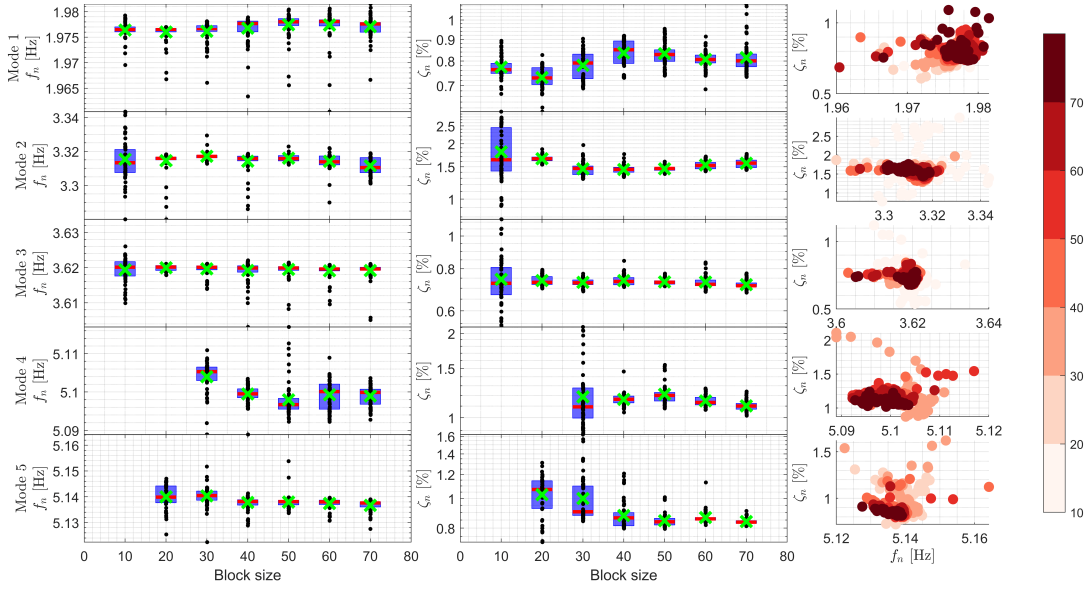

Figure 4.6: Box plots for frequency and damping clusters showing the median, mean, the 25^{th} to 75^{th} quartile range and clusters for block sizes 10 to 70

4.4.3 Measurement duration

Results for the investigation of measurement duration are presented similarly to the block size investigation. Box plots and frequency-damping "cluster diagrams" are presented in Figure 4.7. Further, Table 4.2 provides additional information relating to the variance and minima and maximum of each frequency and damping cluster. The results presented are for a single block size of 50. This makes it difficult to determine the source of random errors on estimates. In other words, whether random errors (outliers in the clusters) arise from the measurement duration or from the specific choice of block size. However, if random errors (outliers) are ignored for the moment, it is possible to make a few observations relating solely to measurement duration:

- Although the block size is relatively high, for a measurement duration of 5 minutes Mode 4 is not identified. This is likely due to the low SNR of Mode 4 which requires longer measurement durations to accurately identify modal parameters.

Table 4.1: Cluster sizes, variances, minima and maxima and percentage differences for Mode 1 to Mode 5 for block sizes ranging from ten to seventy

	Block size	No. of samples	Frequency				Damping			
			Variance	Min [Hz]	Max [Hz]	% diff.	Variance	Min [%]	Max [%]	% diff.
Mode 1	10	67	1,21E-06	1,970	1,979	0,46	2,57E-05	0,669	0,892	33
	20	71	1,50E-06	1,967	1,977	0,51	2,37E-05	0,607	0,827	36
	30	80	1,91E-06	1,966	1,978	0,61	4,32E-05	0,689	0,903	31
	40	85	2,58E-06	1,963	1,979	0,82	4,64E-05	0,730	0,918	26
	50	83	2,60E-06	1,966	1,980	0,71	3,45E-05	0,739	0,953	29
	60	88	3,71E-06	1,960	1,981	1,07	1,38E-05	0,686	0,914	33
	70	84	1,75E-06	1,967	1,982	0,76	5,80E-05	0,734	1,090	49
Mode 2	10	59	3,63E-05	3,293	3,343	1,52	0,0019	0,777	2,990	285
	20	76	1,16E-05	3,280	3,318	1,16	2,07E-05	1,542	1,869	21
	30	77	1,28E-06	3,313	3,329	0,48	1,09E-04	1,288	1,968	53
	40	77	1,10E-05	3,286	3,319	1,00	4,24E-05	1,319	1,757	33
	50	80	1,03E-06	3,312	3,323	0,33	1,49E-05	1,370	1,599	17
	60	80	5,52E-06	3,290	3,322	0,97	4,12E-05	1,420	1,700	20
	70	82	7,28E-06	3,301	3,319	0,55	5,00E-05	1,440	1,760	22
Mode 3	10	53	4,37E-06	3,610	3,634	0,66	2,20E-04	0,537	1,120	109
	20	74	1,81E-07	3,618	3,621	0,08	9,13E-06	0,700	0,794	13
	30	81	6,39E-07	3,614	3,621	0,19	3,80E-06	0,685	0,773	13
	40	82	2,12E-06	3,603	3,622	0,53	8,46E-06	0,706	0,844	20
	50	82	1,02E-06	3,608	3,621	0,36	3,27E-06	0,709	0,774	9
	60	79	1,04E-06	3,610	3,621	0,30	1,30E-05	0,683	0,835	22
	70	82	1,55E-06	3,610	3,620	0,28	4,68E-06	0,680	0,775	14
Mode 4	10	-	-	-	-	-	-	-	-	-
	20	-	-	-	-	-	-	-	-	-
	30	56	3,84E-06	5,090	5,110	0,39	9,38E-04	0,871	2,110	142
	40	64	7,12E-07	5,096	5,103	0,14	3,34E-07	1,045	1,462	40
	50	70	3,89E-06	5,090	5,118	0,55	9,72E-07	1,079	1,544	43
	60	59	3,00E-06	5,092	5,109	0,33	2,45E-05	1,067	1,272	19
	70	72	1,30E-06	5,093	5,104	0,22	1,77E-05	1,017	1,240	22
Mode 5	10	-	-	-	-	-	-	-	-	-
	20	41	4,55E-06	5,125	5,147	0,42	2,38E-04	0,720	1,310	82
	30	68	2,67E-06	5,122	5,152	0,57	3,26E-04	0,843	1,622	92
	40	72	3,03E-06	5,129	5,164	0,69	9,61E-05	0,797	1,208	52
	50	70	1,42E-06	5,134	5,154	0,39	1,95E-05	0,796	1,010	27
	60	64	7,77E-07	5,131	5,140	0,17	1,83E-05	0,819	1,129	38
	70	69	9,00E-07	5,128	5,139	0,22	4,10E-06	0,812	0,910	12

- A clear bias in frequency and damping estimates are observed for Mode 1, Mode 2, Mode 3 at a measurement duration of 5 minutes from the frequency‘damping cluster plots.
- For Mode 1, Mode 2 and Mode 3 increasing measurement duration appears to result in convergence of the mean and median of frequency and damping clusters. This is generally accompanied by a decrease in quartile ranges of the frequency and damping estimates.
- An important observation is that for Mode 1, Mode 2 and Mode 3 measurement durations of 20,25 and 30 minutes produce similar frequency and

damping clusters.

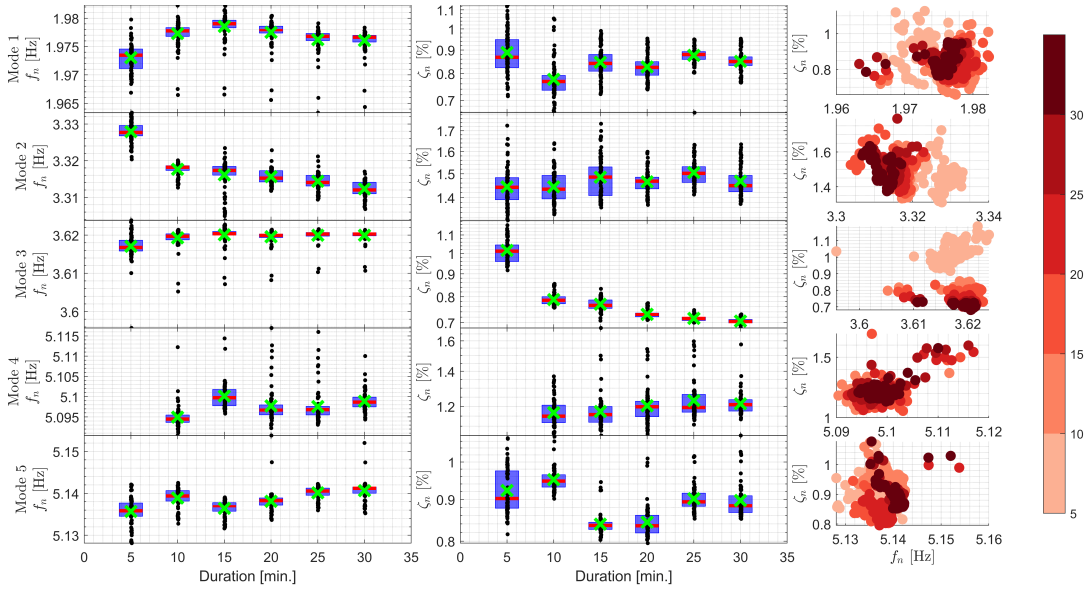

Figure 4.7: Box and whisker diagrams for frequency clusters over model orders 2 to 270 for measurement duration 5 to 30 minutes, block size 50.

4.4.4 Model order

The variation of frequency over model order is presented in Figure 4.8 along with frequency-damping cluster plots for Mode 1 to Mode 5. Here increasing model order is represented by a colour bar changing from blue (low model orders) to red (high model orders). The following is observed for natural frequencies and damping ratios:

- As expected, at low model orders (below 20 for Mode 2 and Mode 3 and below 100 for Mode 4 and Mode 5), certain modes cannot be identified.
- Surprisingly, there is also an upper maximum model order, above which certain modes are no longer identified. This is particularly evident for Mode 2, but all modes of interest generally appear to become "unstable" at high model orders.

Figure 4.8 presents the variation of each damping cluster (normalised with respect to the cluster mean) with increasing model order. Further, the effect of

Table 4.2: Cluster sizes, variances, minima and maxima and percentage differences for Mode 1 to Mode 5 for duration ranging from 5 to thirty minutes and block size 50

	Duration [min.]	No. of samples	Frequency				Damping			
			Variance	Min [Hz]	Max [Hz]	% diff.	Variance	Min [%]	Max [%]	% diff.
Mode 1	5	98	3,01E-06	1,967	1,980	0,66	9,02E-05	0,715	1,127	58
	10	94	2,48E-06	1,967	1,982	0,76	6,89E-05	0,658	1,054	60
	15	98	2,53E-06	1,967	1,982	0,76	4,39E-05	0,722	0,990	37
	20	92	2,36E-06	1,967	1,980	0,66	3,48E-05	0,739	0,953	29
	25	86	2,51E-06	1,963	1,980	0,87	1,47E-05	0,804	0,949	18
	30	92	1,82E-06	1,964	1,978	0,71	2,50E-05	0,765	0,952	25
Mode 2	5	92	2,12E-06	3,320	3,333	0,39	4,38E-05	1,310	1,725	32
	10	88	7,88E-07	3,312	3,320	0,24	3,19E-05	1,333	1,639	23
	15	96	4,86E-06	3,304	3,323	0,58	5,23E-05	1,360	1,735	28
	20	89	1,20E-06	3,312	3,323	0,33	1,61E-05	1,370	1,600	17
	25	90	1,43E-06	3,309	3,321	0,36	2,50E-05	1,412	1,791	27
	30	84	1,46E-06	3,307	3,317	0,30	2,83E-05	1,374	1,634	19
Mode 3	5	93	3,02E-06	3,596	3,624	0,78	3,86E-05	0,917	1,186	29
	10	96	1,33E-06	3,605	3,621	0,44	5,98E-06	0,756	0,855	13
	15	94	1,33E-06	3,607	3,623	0,44	7,15E-06	0,707	0,833	18
	20	92	9,27E-07	3,608	3,621	0,36	2,95E-06	0,709	0,774	9
	25	95	6,67E-07	3,610	3,622	0,33	1,26E-06	0,700	0,747	7
	30	87	6,59E-07	3,611	3,621	0,28	1,35E-06	0,681	0,730	7
Mode 4	5	-	-	-	-	-	-	-	-	-
	10	70	1,55E-06	5,090	5,112	0,43	4,57E-05	1,065	1,369	29
	15	75	1,83E-06	5,096	5,114	0,37	7,87E-05	1,056	1,694	60
	20	80	3,48E-06	5,092	5,117	0,49	7,72E-05	1,063	1,544	45
	25	79	3,20E-06	5,093	5,116	0,45	8,35E-05	1,108	1,597	44
	30	80	1,15E-06	5,094	5,110	0,31	2,83E-05	1,134	1,575	39
Mode 5	5	72	1,99E-06	5,128	5,142	0,27	3,82E-05	0,816	1,069	31
	10	75	1,09E-06	5,133	5,143	0,19	9,87E-06	0,902	1,074	19
	15	78	6,43E-07	5,132	5,139	0,14	7,12E-06	0,803	0,945	18
	20	80	1,27E-06	5,134	5,154	0,39	1,78E-05	0,796	1,010	27
	25	78	4,66E-07	5,136	5,142	0,12	1,24E-05	0,852	1,017	19
	30	85	9,95E-07	5,135	5,152	0,33	2,22E-05	0,852	1,077	26

model order on the eigenvector is presented in Figure 4.9. The approach here was to compare each cluster value to the mean cluster mode shape. The mean mode was calculated iteratively according to the method described by Govers (2012). The following observations may be made:

- Both the variation in damping and eigenvector with model order confirm that there is an "optimum range" for which modes are most stable and a maximum model order above which modes become less stable.
- For this particular case, the results show that for model orders between 100 and 400, damping values and eigenvectors vary by less than 10 percent and 1 percent from the mean, respectively.

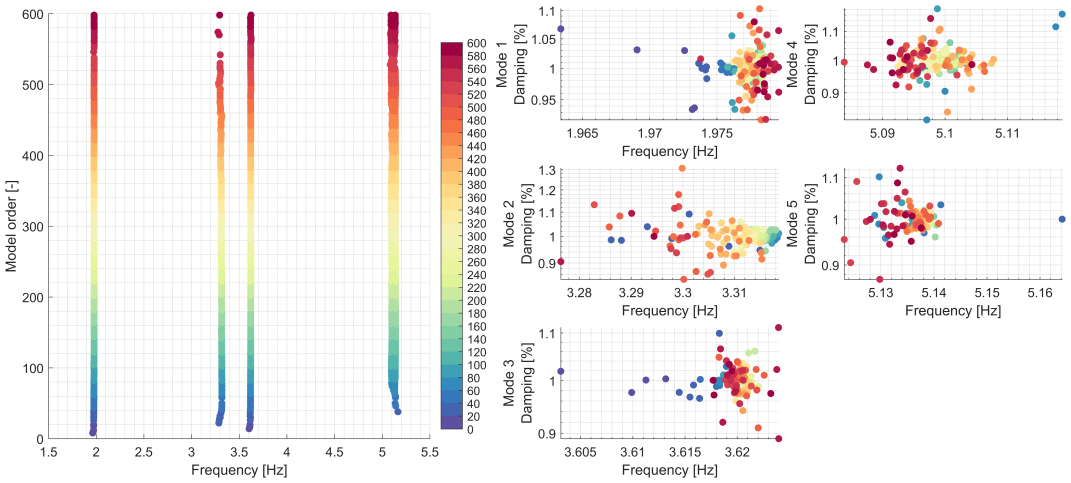

Figure 4.8: Stabilisation diagrams and cluster diagrams showing change in modal parameters with increasing model order

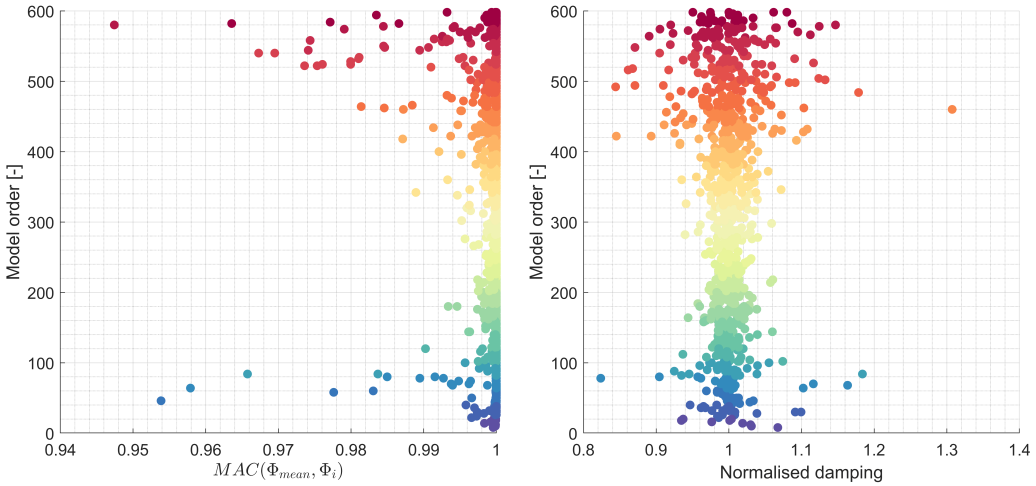

Figure 4.9: Change in MAC and damping values with increasing model order.

4.5 Conclusion

In this chapter, a parametric investigation was conducted for the data-driven SSI algorithm. Three user-specified parameters, namely block size, measurement duration and model order were investigated. For block sizes below thirty, weakly

excited modes are not successfully identified by the algorithm. Estimates converge when the block sizes greater than fifty are used, namely with higher block sizes bias error is removed. Random error may increase when excessive block sizes are used since noise is included in the computation of covariances. Using a block size of fifty, measurement durations below twenty minutes produced estimates with relatively high bias and random errors. However, increasing measurement duration from twenty to thirty minutes did not improve modal parameter estimates further. Extreme model orders (high and low) produce considerable scatter in modal parameter estimates. A suitable range of model orders using a block size of fifty is between 200 and 300. Accurate estimates to build a modal model consisting of five modes were identified.

Chapter 5

Variations in vibration responses of the SA Agulhas II

5.1 Introduction

The SA Agulhas II is subjected to extreme environmental loading conditions with significant structural vibrations induced by both wave-slamming and ship-ice interactions. Analysis of the distribution of the energy across different frequencies reveal significant peaks in energy which correspond to the resonant frequencies of the structure (Soal, 2015). This suggests that these structural vibrations are attributed to the excitation of global modes of vibration. This means that energy is concentrated towards producing specific responses with associated "shapes" of deformation (mode shapes). Knowledge of the modes of the structure and the associated energy provide insight into the participation of different modes and the critical areas where structural deformations are likely to be highest (determined from the mode shapes). Tracking the behaviour of modes provides insight into environmental interactions that are likely to produce resonances of the structure. Methods that produce fine time and frequency resolution are required to capture impulsive wave-slamming events (Bekker and van Zijl, 2019) and ship-ice interactions (Heyn and Skjetne, 2018).

In Chapter 4, five global modes of the SA Agulhas II were identified using a single case of operational data. This case was chosen for its stationary operating conditions and since the ambient conditions (including wind and wave inputs) were thought to represent stochastic inputs relatively well. What remains to be investigated is how the data-driven SSI algorithm performs under non-stationary conditions where the underlying mathematical assumptions are violated. Further, insight into the behaviour of these modes under different extreme loading cases provides a foundation for the development of structural health monitoring on the

SA Agulhas II.

In this chapter, the modal model of the SA Agulhas II that was obtained in Chapter 4 is described. Then different operational cases are presented and the methods that are used to analyse the data is described. Results and discussions of the insights gained are subsequently discussed.

5.2 Modal model

In Chapter 4, five modes were identified for a single set of operational data. The modal model obtained from this case is used as a reference for the analyses that follow. Mean values and standard deviation of the identified natural frequencies and damping ratios, along with descriptions and illustrations corresponding to each mode, are presented in Figure 5.1.

Mode ID	Natural frequency [Hz]	Damping ratio [%]	Mode shape description	
1	1.98 ± 0.002	0.83 ± 0.1	First vertical bending: Two-node bending with maximum displacement at midship and extreme fore and aft of the vessel.	
2	3.32 ± 0.002	1.5 ± 0.1	Lateral bending: Two-node bending with maximum displacement at the midship and extreme fore and aft of the vessel.	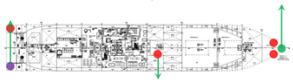
3	3.62 ± 0.002	0.73 ± 0.02	Second vertical bending: Three-node bending with maximum displacement at fore and aft of the vessel. First node (relative to the bow located between the cargo-hold and midship and other two nodes located towards the stern.	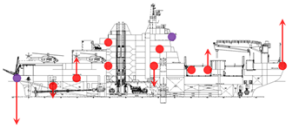
4	5.10 ± 0.005	1.2 ± 0.1	Torsional: One-node torsion with maximum displacement at the bow and stern in opposite directions.	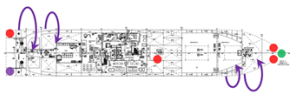
5	5.14 ± 0.003	0.85 ± 0.04	Third vertical bending: Four-node bending with maximum displacement at bow and slightly smaller relative deflection at the stern. First node located between the bow and cargo-hold and three additional nodes located between mid-ship and stern. .	

Figure 5.1: Natural frequencies, damping ratios and mode shapes of five modes of the SA Agulhas II.

5.3 Description of case studies

During the Weddell Sea Expedition the SA Agulhas II encountered a wide range of challenging operating conditions. Four case studies of approximately two hours

each were selected for analysis. The location where these cases were recorded are roughly indicated on the voyage track in Figure 5.2.

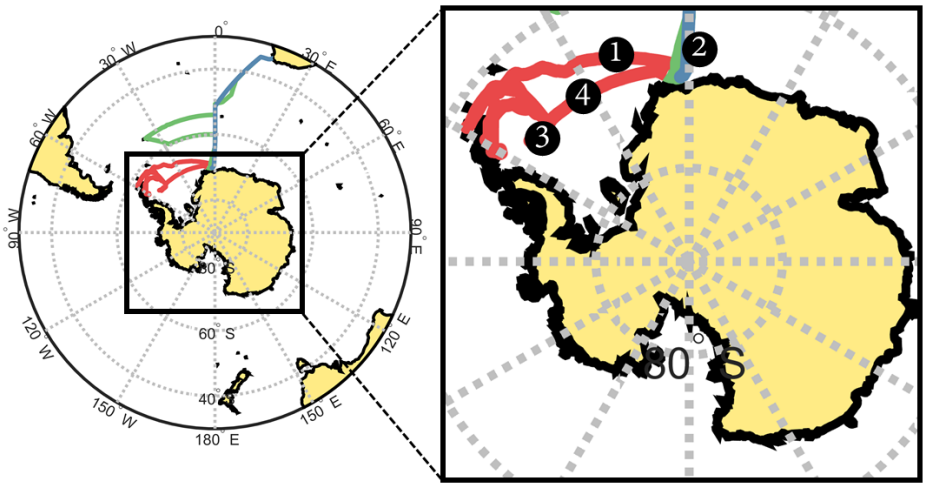

Figure 5.2: Location where case studies were recorded on voyage track.

The first case (Case 1) is a reference case which consisted of stationary, calm open water conditions. Two cases (Case 2 and Case 3) represent instances of ice navigation where the vessel was forced to engage in backing-and-ramming operations to break through sea-ice. Both the ice cases represented a challenge to navigational officers who were particularly concerned about damage to the propeller due to ice impacts and having the vessel become beset in the heavy sea-ice for extended periods of time. Finally, an open water storm case (Case 4) was selected to gain insight into the vibration response of ice-going vessels operating in harsh open water conditions in the Southern Ocean. Descriptions of Case 1, Case 2 and Case 4 are subsequently provided.

5.3.1 Case 1: Transit for Penguin Bukta to Larsen C

This case (Case 1) is a record of stationary vibration response obtained during transit of the vessel from Penguin Bukta to the Larsen C ice shelf and was recorded on 4 January 2019 between 14h00 and 17h00. The vibration measurements presented here provide a reference to which non-stationary cases may be compared. During

transit the vessel skirted along the ice edge with minimum ice navigation. Four engines were used to produce maximum power output so that the vessel could reach its destination as quickly as possible. For this particular case, the vessel sailed through calm open water operating under stationary conditions with the propeller running at constant speed of 140 rpm and the vessel maintaining speed just under 9 knots. Wind speed varied between 14 and 20 knots and the vessel maintained course in a north-westerly direction. Figure 5.3 provides an example of the calm sea-state and minimal ice cover that the vessel experienced during operation.

Figure 5.3: Photograph showing calm, open water during the transit recorded in Case 1.

5.3.2 Case 2: Ice breaking on approach to Penguin Bukta

Case 2 represents the first of two ice cases and was recorded during the approach to Penguin Bukta between 07:00 and 09:00 on 17 December 2018. Since this case was recorder prior to reaching the ice shelf, the vessel was heavily loaded with cargo. The cargo was mostly stored in the cargo-hold on Deck 3 and fuel containers were stacked on top of the cargo-hold on Deck 4. Figure 5.4a shows a photograph of the vessel in port prior to departure from Cape Town in its fully loaded condition. The presence of the cargo adds mass to the ship and is also expected to have a stiffening effect on the vessel structure due to the way it is fastened to the deck structure. Case 2 was thought to represent harsh ice conditions with ninety to one hundred percent sea-ice concentration and average and maximum ice thicknesses observed of 60 and 120 cm, respectively. Worth considering is that the ice observer on shift noted that large amounts of the total sea-ice concentration was ”brash” ice. Brash ice is basically broken up pieces of ice floating on the sea surface.

Although brash ice resists ship motion it is not expected to be associated with large ice loads on the vessel hull. During this case, the vessel was stopped twice by vast floes over 2 km in diameter and was forced to engage in backing-and-ramming operations to proceed through the ice field. Further, the highly concentrated brash ice which surrounded the vessel on all sides provided little room for the vessel for manoeuvring. The vessel used the propellers and stern thrusters to clear managed ice from the area surrounding the stern and the vessel would reverse as far as possible into the broken ice field before proceeding to ram. Figure 5.4b presents the highly concentrated ice conditions during Case 2. A large floe (over 1km) in diameter can be identified slightly fore of the vessel on the port side with smaller floes and brash ice surrounding the vessel.

(a) (b)

Figure 5.4: Photograph showing (a) the SA Agulhas II loaded with cargo in Cape Town Harbour and (b) the highly concentrated ice conditions during the approach to Penguin Bukta.

5.3.3 Case 3: Ice breaking on approach to Endurance wreck site

The second ice case records the approach to the wreck site of Sir Ernest Shackleton's ship, the Endurance. The wreck site is located in the western Weddell Sea in an area known to be always covered with sea-ice. The ice conditions encountered here were similar to that for Case 2, with ice thicknesses ranging between 60 and

120cm, and vast floes exceeding 2 km in diameter. According to the voyage ice pilot, most of the ice in this area was classified as multi-year ice with glacial inclusions and was therefore judged to be more challenging than the ice conditions encountered at Penguin Bukta. Other key differences between the two ice cases is that this case was recorded after a significant amount of cargo had been offloaded at Penguin Bukta. Further, the temperatures in the Weddell Sea in early February are significantly lower than that in December in East Antarctica where Penguin Bukta is located. Figure 5.5a shows a photograph of the typical ice conditions encountered in this area which consisted of large areas covered with consolidated sea-ice and small narrow open water leads forming between the floes. During operation close to the wreck site, the vessel was mostly able to navigate through these open water leads between large ice floes. At times the vessel was stopped by vast floes and was forced to enage in backing and ramming operations. A major problem was that due to the low temperatures, the vessel could not remain stationary for long periods of time as this posed a risk of the vessel becoming beset in the open water leads where ice was forming at very high rates. Case 3 was recorded hours before the vessel was caught between two ice floes in an open water lead. When this occurred, a crane suspending a fuel container would be used in an attempt to adjust the trim of the ship to free the vessel from the ice as shown in Figure 5.5b.

(a) (b)

Figure 5.5: Photograph showing (a) the ice conditions close to the Endurance Wreck site and (b) the vessel attempting to free itself from the ice using a fuel container suspended by a crane.

5.3.4 Case 4: Open water storm during transit across Weddell Sea

The final case represents an open water storm which the vessel encountered during transit from the wreck site to Penguin Bukta in the northern part of the Weddell Sea. Swells over 10m caused significant rigid body heave, roll and pitch motions and both bow and stern wave slamming was experienced by the vessel. While navigating the ship through the storm navigational officers slowed the vessel down to speeds ranging between 2 and 3 knots and directed the vessel head-on into the oncoming waves. This case provides rare insights into the operational profile of ice-going vessels operating in Antarctica that must contend with both harsh ice conditions and extreme weather conditions. Figure 5.6 shows the vessel undergoing a bow slam as the vessel steers head-on into the oncoming waves.

Figure 5.6: Photograph showing the SA Agulhas II undergoing a wave-slam at the bow.

5.4 Analysis methods

Different analysis methods are applied to the case studies presented in the previous section. These methods are inspired by many of the latest developments in literature pertaining to ice-structure interactions, which are discussed in Chapter 2. A summary of the methods used for the analysis of the full-scale vibration measurements are presented in Figure 5.7, along with the associated insights that

may be gained. A flow diagram which shows the different analyses with relation to one another is presented in Figure 5.8. First the four cases are divided into observation windows twenty minutes long with seventy-five percent overlap. This results seventy-five observation windows in total (nineteen and sixteen windows for Case 1 and Case 2 and twenty for both Case 3 and Case 4). The analyses in Figure 5.7 and 5.8 are performed on each of the observation windows, which are subsequently discussed.

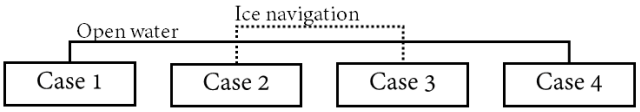

Analysis type	Analysis methods	Insights
1 OMA and mode tracking	Automated modal analysis (Data-driven SSI, pole cleaning, clustering and tracking).	• Performance of OMA algorithms under different operating conditions. • Overview of changes in dynamic properties of a system within and across different cases.
2 Mode energy analysis	Definition of modal domain and calculation of energy under APSD.	• Relative amounts of energy associated with each modal response within cases and across cases. • Changes in the participation of modes in total vibration response.
3 Mode decomposition	Time-domain digital filtering using the modal defined in four as the passband .	• Time-varying behaviour of modal responses.

Figure 5.7: Illustration of methods involved with analysis of case studies.

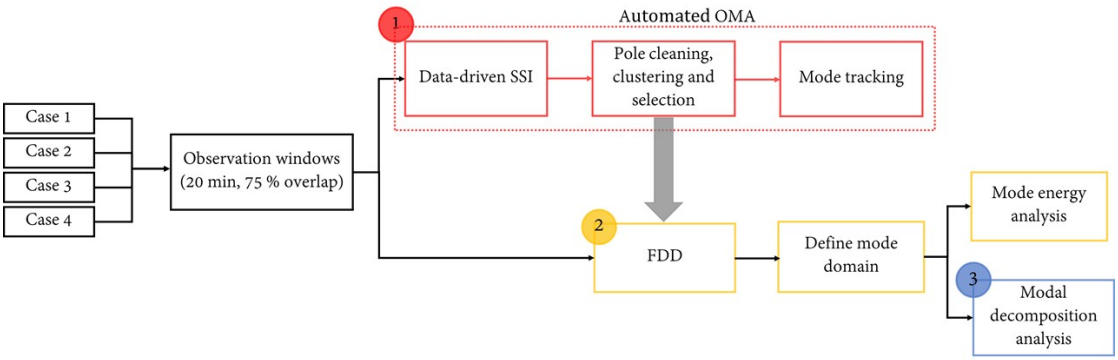

Figure 5.8: Flow diagram showing the progression of the analysis on the four cases.

5.4.1 Operational modal analysis and mode tracking

Operational modal analysis (OMA) was performed on each observation window using the data-driven SSI algorithm with the following parameters:

- Block size of 50, $i = 50$.
- Maximum model order, $n_{max} = 300$.

The observation window length ($n_b = 20$ min.), block size and maximum model order were selected based on insights gained during the parameter investigation as explained in Chapter 4. The high overlap between consecutive observation windows was used in an attempt to refine the resolution of the analysis so that only five minutes of "new" data was included in every window. Significant changes in vibration responses, which occur under non-stationary conditions (such as in ice and open water storms), could thus be monitored. However, it is recognised that impulsive interactions (between ship and ice or during wave slamming) occurs within seconds and that even using a sliding window with high overlap suffers from having poor time resolution. Automated pole cleaning and clustering was performed on the poles and eigenvectors identified using data-driven SSI. Pole cleaning was achieved using the following limits: $\delta f \leq 0.01, \delta\zeta \leq 0.1, MAC(\psi_i, \psi_j) \geq 0.95$. Further, MACXP was used to perform clustering and the clusters which correspond to the five modes of interest were identified. MACXP tracking was performed to assign modes identified in each analysis window to the appropriate mode family [1]

5.4.2 Mode energies

In a study by Heyn and Skjetne (2018), the time-frequency signature of acceleration measurements from an icebreaker were analysed for different cases of ship-ice interaction. A Wigner-Ville distribution which calculates instantaneous energy across different frequencies was used to predict the dominating type of ice failure mechanisms that were occurring at certain ship-ice interfaces on the hull. Further, the natural frequency of the first vertical bending mode was tracked using peaks in the Wigner-Ville distribution for specific time frames. The natural frequency mode was found to vary due to the addition of effective mass on the vessel hull during ship-ice interactions. Building on the ideas presented in this study, an attempt was made to gain deeper insight into the mechanisms by which environmental loads (mainly waves and ice) induce modal responses that vary in energy. As shown in Figure 5.8, this was achieved by combining the results of the

[1]The algorithm used to perform mode tracking was developed during a research exchange to the Department of Structural Dynamics and System Identification (SAS) at the Deutsches Zentrum für Luft und Raumfahrt (DLR) in Göttingen, Germany.

automated data-driven SSI with results from a frequency-domain decomposition (FDD) analysis. The FDD technique was used to define a modal domain corresponding to each mode from which associated energies could be calculated. As described in detail in the previous chapter, FDD involves computing a singular value decomposition (SVD) of a spectral density (SD) matrix. Natural frequencies are obtained by finding peaks in the first (or second when there are closely spaced modes) set of singular values. The (first) singular vector corresponding to the frequency lines where the peaks occur are estimates of mode shapes. Consider an example of the spectra of first and second singular values obtained from one of the observation windows of Case 2, Figure 5.9. Points near peaks (either in the first or second singular values) that correspond to the five modes of interest are marked with crosses. These points represent the frequency lines which correspond to singular vectors that are most similar to the eigenvectors that were identified using data-driven SSI. These singular vectors are then used as references to which neighbouring singular vectors are compared to define a modal domain. The modal domain is defined as the region in which neighbouring singular vectors have a MAC value greater than 0.9 relative to the respective reference singular vectors.

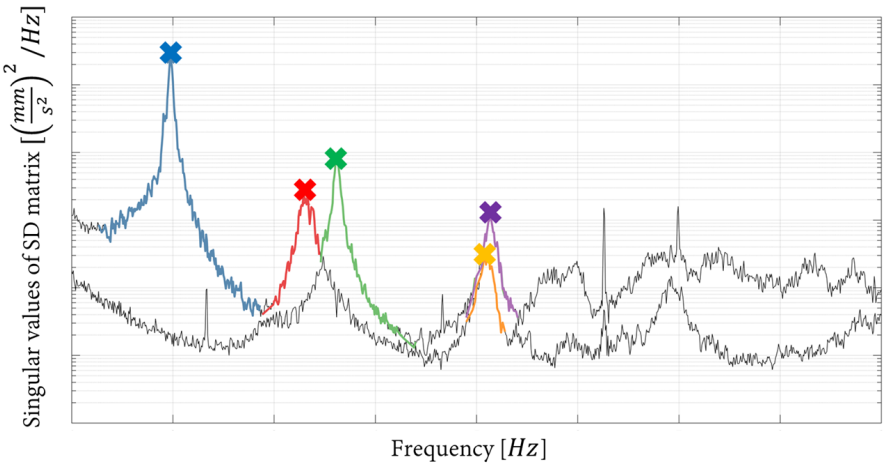

Figure 5.9: An example of the modal domains that are defined using FDD.

Once the modal domains were identified, a set of auto-power spectral densities were calculated for each mode. The channels used to compute the APSDs correspond to the five eigenvector components that have the highest (relative) amplitude [2]. The associated mode energies are then estimated as the square-root of

[2]The idea to quantify vibration level (energy) using APSD functions corresponding to the highest amplitude components of the respective mode shapes was inspired by collaborative re-

the area under auto-power spectral densities of the corresponding channels. Figure 5.10 shows an example of the APSDs from five channels that are used to compute the energies for each mode of interest.

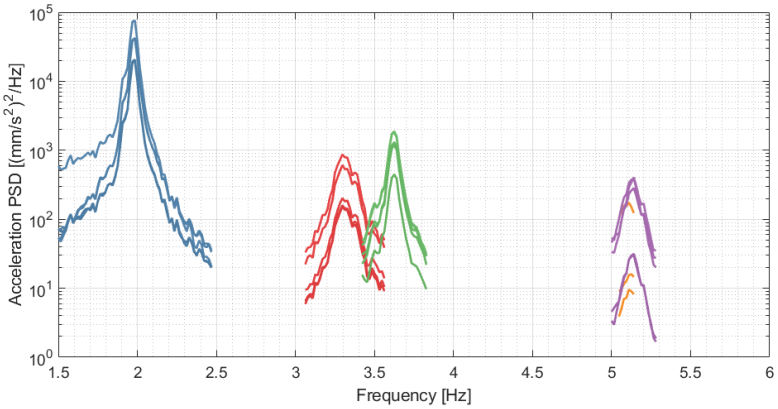

Figure 5.10: Examples of APSDs that are used to estimate mode r.m.s. energies.

5.4.3 Mode decomposition

One of the disadvantages of estimating mode energy using a root-mean-square is that the energy is "smeared" over the entire analyses period. Since structural vibrations result from environmental loads that can change drastically during an analysis period, the time-varing behaviour of the modal responses is lost. To overcome this challenge, the modal bandwidths that were defined during the mode energy analysis are used as passband frequencies for a bandpass digital filter that is used to eliminate all frequencies outside the bandwidths associated with each mode [3]. The result is five filtered time-domain signals corresponding to the five modes of interest for the different observation windows. These signals are thought to be representative of the response associated with a single mode during the observation window and are used to gain insight into the participation of the modes in the total vibration response.

search at DLR in Göttingen, Germany.

[3] In SSI-data it is possible to perform modal decomposition on a measured time-domain signal in order to isolate the individual response of each mode, see for example Peeters and de Roeck (1999). Brainstorming discussions were held at DLR in Göttingen, Germany relating to the potential applications of mode decomposition on full-scale data from the SAAII. Although the methods implemented in this work are different to those originally discussed, the idea to perform mode decomposition was inspired during these discussions.

5.5 Mode tracking

Mode tracking (as explained in Section 5.4) was performed on the observation window of the five cases to track changes in the modal parameters of the five modes identified in Section 5.2. The results and main outcomes are subsequently discussed.

5.5.1 Results

The changes in natural frequencies and damping ratios may be seen in Figure 5.11. Further, five MAC matrices corresponding to the five modes are presented in Figure 5.12 to illustrate changes in the corresponding eigenvectors [4]. Each MAC matrix compares the mode shapes identified for each observation window for the four cases. Four sub-regions or areas belonging to the four cases are labelled in Figure 5.12. It is expected that the mode shape will not vary much within a case and that the MAC value will be high in the sub-regions where mode shapes from the same case are compared. For example, the first 19×19 elements of each MAC matrix compares the mode shapes identified across the nineteen observation windows of Case 1.It is expected that here there will be high similarity between the mode shapes. This means that when two different cases are compared, the mode shapes will vary more and there will be lower similarity in these sub-regions. As an example, consider the sub-region of the MAC matrices where Case 1 and Case 2 are compared (rows 20 to 25 and columns 1 to 19). Here it is expected that the MAC values will be lower since a calm, open water case is compared to a case where the ship is operating in ice. White blocks represent missing values due to modes not being identified during the corresponding observation windows. Further, mean and standard deviations were calculated for the clusters from all the observation windows of each case for each mode. Table 5.1 summarises information about the clusters identified for the five modes.

For the reference case (Case 1), the following observations may be made:

- As expected, the stationary operating conditions result in small variations in modal parameters across the different observations windows.
- There are larger variations in the damping ratio than natural frequency.
- Some modes vary more than others, with the greatest variation in frequency, damping ratio and eigenvector for the torsional mode (Mode 4).

[4]The idea to compare mode shapes obtained from different analysis windows in a MAC matrix in this way was inspired by brainstorming discussions held during a research exchange at DLR in Göttingen, Germany. This type of display is commonly used in the in-house Matlab SAS toolbox developed at DLR.

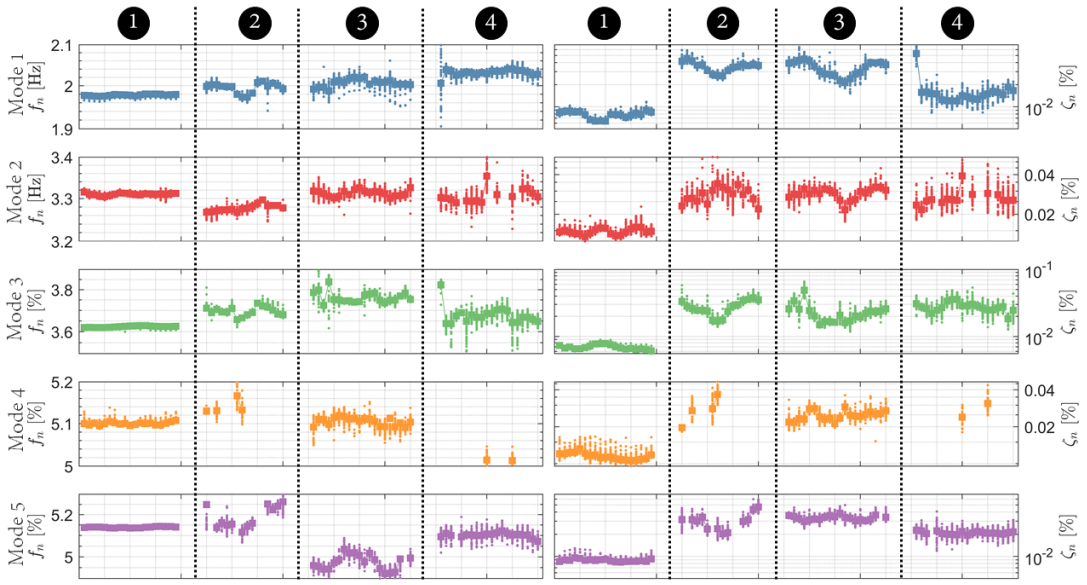

Figure 5.11: Tracking of natural frequencies and damping ratios within and across the four cases.

Further, comparing the open water case to the reference case yields the following interesting observations:

- Mode 1, Mode 3 and Mode 5 (vertical bending modes) are identified consistently across all observation windows. Mode 2 and Mode 4 which represent lateral bending and torsional modes, respectively, are not identified well under stormy conditions. This could be explained by hydrodynamic and wave-slamming forces acting predominantly in the vertical direction while the vessel is steered head-on into the waves.
- The natural frequency and damping ratio of the vertical bending modes, namely Mode 1, Mode 2 and Mode 5, are generally higher than for Case 2.
- The normalised variances in the clusters of both natural frequency and damping identified for Case 4 are generally higher than for Case 1.
- There is high similarity in the eigenvectors of the vertical bending modes between Case 1 and Case 4.
- In the observation windows where the lateral bending modes are identified for Case 4, there appears to be some variation in the eigenvector within the case itself and compared to Case 1.

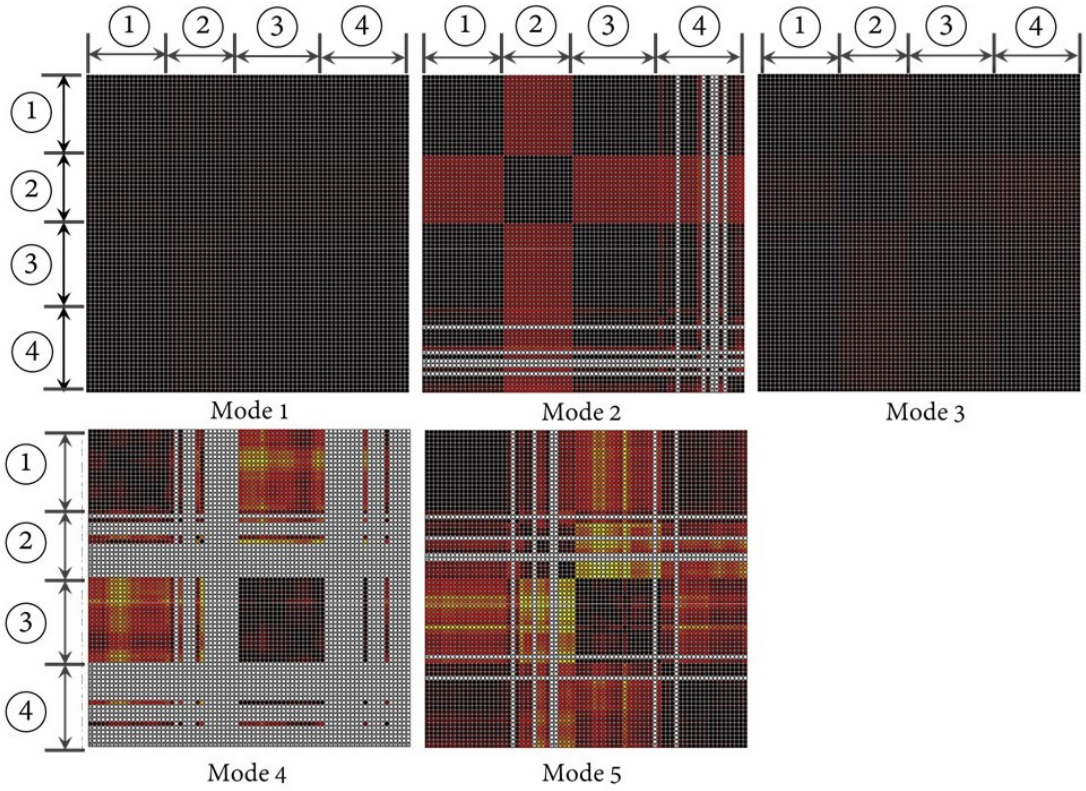

Figure 5.12: MAC matrices showing differences in eigenvector within and across the four cases.

Similarly, comparing the ice cases to one another and to the two open water cases, the following is observed:

- Damping ratios for the two ice cases are similar in magnitude and are higher than for the two open water cases.
- The natural frequencies for Mode 1, Mode 2 and Mode 3 are generally higher for Case 3 compared to Case 2, while Mode 4 and Mode 5 have a lower natural frequency for Case 3 than for Case 2. The lower natural frequency for Mode 4 and Mode 5 could be attributed to the difference in cargo-loading between the two cases (more cargo for Case 2, increasing the mass). It would make sense that these modes are particularly affected since the mode shapes involve significant motions at the cargo-hold (see Figure 5.1).
- Mode 1, Mode 2 and Mode 3 are generally identified very well for both of the ice cases. Mode 4 is mostly identified for Case 2 and is well identified

Table 5.1: Summary statistics (including cluster size, mean μ, normalised standard deviation σ/μ and normalised range $(\max - \min)/\mu$) of combined clusters obtained from the data sets of the four cases for the five modes of interest.

Case	Mode ID	Cluster Size	Frequency [Hz]			Damping [%]		
			μ	σ/μ	$(f_{max} - f_{min})/\mu$	μ	σ/μ	$(\zeta_{max} - \zeta_{min})/\mu$
Case 1	1	1740	1,987	0,0023	0,011	0,780	0,120	0,738
	2	1713	3,310	0,0014	0,010	1,48	0,074	0,703
	3	1753	3,624	0,0010	0,009	0,690	0,083	0,490
	4	1480	5,100	0,0010	0,010	1,15	0,101	0,614
	5	1552	5,139	0,0006	0,006	0,880	0,067	0,581
Case 2	1	1170	1,994	0,0066	0,040	3,50	0,184	1,028
	2	1137	3,276	0,0030	0,017	2,79	0,182	1,287
	3	1349	3,695	0,0059	0,051	2,72	0,259	1,622
	4	115	5,141	0,0046	0,022	2,81	0,244	1,011
	5	464	5,189	0,0309	0,561	3,08	0,310	1,404
Case 3	1	1521	2,008	0,0060	0,050	3,23	0,250	1,543
	2	1392	3,313	0,0033	0,027	2,80	0,113	0,728
	3	1307	3,757	0,0091	0,113	2,09	0,327	2,576
	4	1142	5,107	0,0109	0,368	2,42	0,110	0,733
	5	951	4,972	0,0080	0,051	3,32	0,117	0,782
Case 4	1	1469	2,032	0,0065	0,095	1,58	0,477	4,349
	2	845	3,305	0,0062	0,053	2,65	0,207	1,269
	3	1101	3,668	0,0116	0,106	2,76	0,215	1,483
	4	73	5,014	0,0038	0,018	2,69	0,189	0,953
	5	1312	5,102	0,0045	0,033	2,09	0,142	1,379

in Case 3. The torsional mode (Mode 5) is tracked poorly for Case 2, but tracked consistently for Case 3.

- Variances in frequency and damping estimates are generally higher for Case 2 compared to Case 3. Compared to the open water cases, both ice cases have higher variances in modal estimates than the reference case (Case 2). Case 3, however, generally has a lower variance in natural frequency than Case 4 but a higher variance in damping. Case 2 has the highest variances overall.

- Noticeable trends may be seen in the change of both the natural frequencies and damping ratios for the ice cases. The changes in modal parameters within these two cases are more significant than for the open water cases and most likely represents some sort of relationship between the modal parameters and the sea-ice surrounding the ship.

- Damping appears to be more sensitive to change than natural frequency.

- At times a direct relationship between changes in natural frequency and damping ratios exists. For example, both the natural frequency and damping follow a similar trend for Mode 1 during Case 2 and similarly, for Mode 5 in Case 3. At other times, such as for Mode 3 in Case 2 an inverse trend is observed between changes in natural frequency and damping. This could provide insight into the mechanism that causes the trend. An inverse relationship is expected when the changes are caused by the amount (or thickness) of sea-ice since ice may increase damping and add mass to the structure, which lowers the natural frequency.

- Some modes change more than others which suggests that some modes participate more in the ship-ice interaction mechanism.

- The eigenvectors for Mode 1 and Mode 3 are similar for Case 2 and Case 3. Further, insignificant changes in eigenvector are observed for these two modes when comparing the ice cases to the open water cases.

- The eigenvector identified for Mode 2 is different in Case 2 compared to Case 3 although both represent ice cases. Similarly, even larger differences are seen when comparing Mode 4 and Mode 5 for the two ice cases. This could be explained by the presence of large amounts of cargo during Case 2 which constrains the corresponding mode shapes.

5.5.2 Discussion

Automated mode tracking was used to track the same modes across vastly different operating conditions. Based on the results of the reference case (Case 1), stationary conditions which satisfy the fundamental assumptions of stochastic loading produces favourable results. In particular, under these conditions modes are consistently identified by automated modal analysis procedures. The failure of modes to be identified and tracked under different conditions may be due to a number of reasons:

- The mode is not identified by the data-driven SSI algorithm, possibly because the user-specified parameters are not suitable for the specific case.

- The mode is identified, but the mode is not similar enough to an existing mode family and is not correctly assigned.

- The mode is not excited sufficiently to produce a large enough modal response to be accurately identified.

Further work is required to determine the exact cause. The torsional mode (Mode 4) appears to be the most problematic for identification and tracking. It is worth noting that Mode 4 is very close in natural frequency to Mode 5, which could make it particularly difficult for an identification algorithm to identify this mode accurately especially when it is weakly excited. There may be physical reasons for the disappearance of this mode. The associated mode shape involves significant motion close to the cargo-holds which may be constrained (or stiffened) by cargo when the ship is heavily loaded (as it was during Case 2). Further, the disappearance of this mode (and other modes, such as Mode 2) during Case 4 may further be related to the nature of the excitation force which is thought to have a predominant vertical component.

During ice navigation damping ratios were observed to follow trends that are thought to be caused by the presence of sea-ice and ship-ice interaction mechanisms. Different cases revealed varying scatter in modal parameter estimates. The scatter could be an indication of the degree to which the underlying mathematical assumptions of OMA are violated under the associated operating conditions. For example, high scatter was observed during Case 2, Case 3 and Case 4 where conditions were highly non-stationary. Further, during Case 2 significant energy due to various sources of harmonic excitation may be another reason for uncertainty in mode estimates. Mode 1, Mode 2 and Mode 3 are identified and tracked consistently across all cases and are good candidates for continuous tracking applications.

5.6 Mode energies

In order to gain insight into how the energy of modal responses varied across the different operational conditions, root-mean-square energies associated with the five modes of interest were calculated. Each observation window from the four cases were analysed according to the method in 5.3.

5.6.1 Results

Energy bar plots showing the relative amount of energy in the five different modes across the respective observations windows of Case 1 and Case 4 are presented in Figure 5.13. Similarly, Figure 5.14 presents the relative energies during ice navigation. The energies of all four cases for the five modes are compared in Table 5.2.

The following observations may be made relating to the two open water cases:

- As expected, the calm open water reference case (Case 1) is far smaller than that for the storm case (Case 4).

- The amount by which the total energy in modal responses differ for Case 1 and Case 4 varies from mode to mode. The largest difference is observed for Mode 3 where the energy attributed to this mode is more than ten times bigger for Case 4 compared to Case 1. The smallest differences between the two cases is observed for Mode 2 with differences generally less than factor 2.

- Mode 1 dominates the modal response for both open water cases.

- During Case 4 there was larger variation in the energies attributed to each mode than for Case 1.

- During the open water storm, Mode 1 and Mode 3 contribute most of the energy in the modal responses. The lowest modal energy corresponds to Mode 2 (the lateral bending mode).

- Interestingly, although Mode 4 (the torsional mode) is identified quite poorly during the open water storm, the energy is greater than for Mode 5 which is identified consistently during this case. For Case 1, the torsional mode has the lowest energy.

Concerning the ice cases:

- The mode energies associated with the open water storm are larger than for both the two ice cases.

- The energy of all modes is greater for Case 3 than for Case 2.

- Surprisingly, the energy in the modal responses are larger for the reference case than for the first ice case, Case 2.

- For Case 3, the modal response is dominated by Mode 1. The third vertical bending mode further contributes a significant amount of energy. The lowest energies correspond to the lateral bending (Mode 2) and torsional modes (Mode 4).

- Relatively speaking, Mode 1 and Mode 2 are the modes with the highest energies for Case 2.

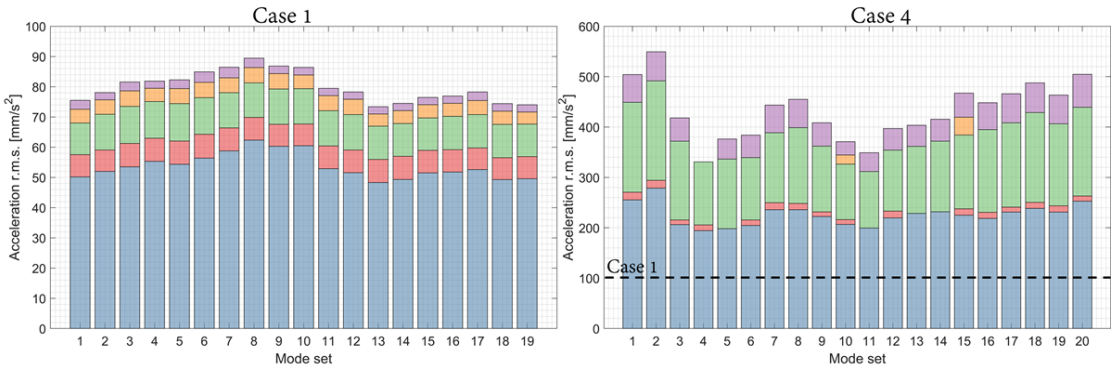

Figure 5.13: Energy bar plots showing the amount of energy associated with Mode 1 (□), Mode 2 (□), Mode 3 (□), Mode 4 (□) and Mode 5 (□) tracked across the two open water cases.

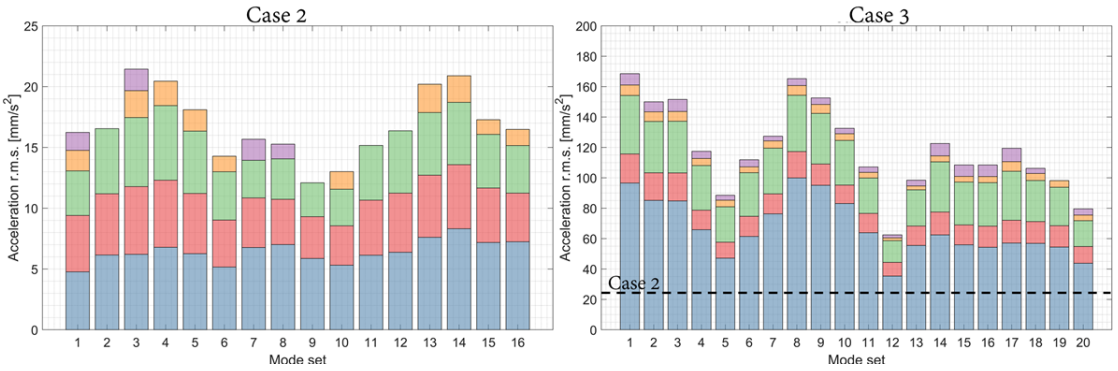

Figure 5.14: Energy bar plots showing the amount of energy associated with Mode 1 (□), Mode 2 (□), Mode 3 (□), Mode 4 (□) and Mode 5 (□) tracked across the two ice cases.

5.6.2 Discussion

Energies related to the five modes of interest were tracked across the four cases. The first vertical bending mode and third vertical bending mode generally have the highest energies for all the cases. Using the mode shapes corresponding to these modes, it is possible to locate regions where high stresses due to large deflections are likely to cause structural fatigue damage. Particularly the open water storm case contained significant amounts of energy in these modal responses. Future research may be devoted towards investigating the implications for the structural-health of ice-going vessel that spend considerable amounts of time navigating in harsh open water conditions. Energy associated with lateral bending, torsion and third vertical bending is generally low. Interestingly, low energy was generally

Table 5.2: Summary of energy in the five modes of interest for the four cases.

	Case 1		Case 2		Case 3		Case 4	
Mode ID	**Bandwidth**	**r.m.s** $[mm/s^2]$	**Bandwidth**	**r.m.s** $[mm/s^2]$	**Bandwidth**	**r.m.s** $[mm/s^2]$	**Bandwidth**	**r.m.s** $[mm/s^2]$
Mode 1	1,50 to 2,50	54 ± 15	1,64 to 2,36	6 ± 2	1,53 to 2,44	70 ± 27	1,48 to 2,60	223 ± 61
Mode 2	3,05 to 3,60	8 ± 3	3,06 to 3,47	5 ± 1	3,10 to 3,53	14 ± 6	3,25 to 3,35	12 ± 5
Mode 3	3,40 to 3,85	11 ± 3	3,50 to 3,91	4 ± 1	3,41 to 4,16	30 ± 10	3,13 to 4,13	142 ± 39
Mode 4	5,05 to 5,13	3 ± 2	5,13 to 5,19	2 ± 1	5,03 to 5,16	$4{,}6 \pm 2{,}5$	4,94 to 5,28	46 ± 18
Mode 5	4,90 to 5,40	5 ± 2	5,11 to 5,17	2 ± 1	4,88 to 5,03	$5{,}2 \pm 3$	4,93 to 5,11	27 ± 15

associated with the modal response of Case 2 although it represents an ice-breaking case. Further investigation are required to determine the exact cause. One possible reason is that heavy cargo-loading increased stiffness and mass, lowering the modal response amplitudes and energies.

5.7 Mode decomposition

One of the limitations of the mode energy analysis performed in the previous section is that information about the time-varying behaviour of modal responses are lost. In fact, this is one of the major drawbacks of OMA in general. As explained in Section 5.3, modal parameter estimates that were obtained with a very "coarse" time resolution (20 minutes) using OMA are used to isolate frequency components in an acceleration time-history that are considered to be representative of the time-varying behaviour of modes.

In this section, an observation window from each of the four cases is used to study the time-varying behaviour of the modal responses. Only the first three modes are considered since these are the modes with the highest energy.

5.7.1 Results

The following observations relating to the open water case may be made:

- The mode bandpass filtered signals for Case 1 are noticeably more stationary than for Case 4.
- During Case 4, the vessel speed is relatively constant, however, the mode bandpass signals are highly non-stationary. Several impulses followed by free-decays are observed, especially for Mode 1 and Mode 3. This likely represents wave-slamming events at the bow and stern with the associated forces containing significant forces in the vertical direction. The nature of this excitaiton (as an impulse occurring at extreme ends of the vessel) is expected to induce a large participation of the vertical bending modes in the overall vibration response.

- The mode bandpass signal for the lateral bending mode (Mode 2) is very small compared to that for Mode 1 and Mode 3. However, there is a large variation in amplitudes in signal (non-stationary). It is likely that this mode is not excited as much as the vertical bending modes due to hydrodynamic and wave slamming forces with a predominant vertical component.

Similarly, the mode bandpass signals for the two ice cases for Mode 1, Mode 2 and Mode 3 are presented in Figure 5.16. Annotations relating to the operational profile of the ship may be found in Table 5.3. The following is observed:

- Although high levels of vibration are recorded during Case 2, the mode bandpass filtered signals record low levels of vibration compared to Case 3.
- The mode bandpass signals are non-stationary for both Case 2 and Case 3.
- During ramming (see ① and ④), before the ship reaches maximum speed there are significant responses in the mode bandpass signals, especially for Case 3. This indicates possible ship-ice interactions (such as bending failure of the ice) which exerts a dynamic ice load signal.
- During reversing there is generally low modal responses (see ③ for example). This is expected since there are no interactions due to ice failure on the hull to induce a vibration.
- While the ship is breaking through managed ice (see ② and ⑤) there are impulsive peaks in the mode bandpass signals of all the modes. This means that the modes are participating in the ice-ship interaction and that impulsive ice loads are exciting global modes of the ship. These impulsive peaks may be related to crushing of the ice against the vessel hull during high-speed interactions with the ice.
- High peak values occur especially in the vertical bending modes (Mode 1 and Mode 3). This may indicate that the direction of induced ice load is in the vertical direction.
- When the ship encounters a floe (⑥) and stops, there are large levels of vibrations in the frequency range of the three modes. This may be related to ice loads caused by bending failure of the ice as the ice fails under the weight of the ship.
- There are instances when vibration levels are high but modal responses are low (②). This may be because the ship is not interacting with the ice or because the ship-ice interaction is not producing a significant modal response.

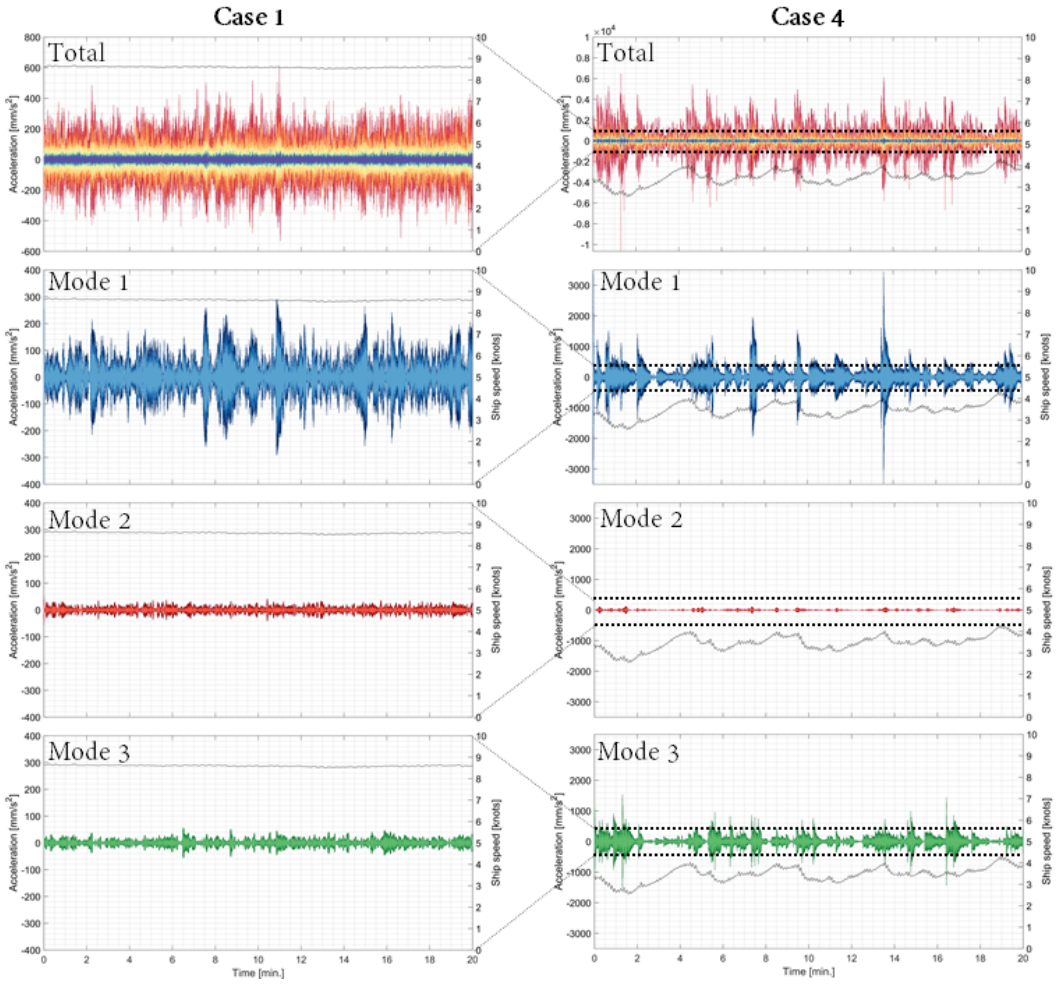

Figure 5.15: Mode bandpass filtered responses for a single observation window from the two open water cases.

Table 5.3: Comments relating to the operational profile of the ship for mode bandpass filtered signals.

Case	Label	Comments
Case 2	1	Vessel reverse and rams a floe three times at 3 knots.
	2	Vessel breaks through floe on the third ram and accelerates to approximately 3 knots.
	3	Vessel reverses through brash (managed) ice.
Case 3	4	Vessel rams floe once at 2 knots and breaks through the floe.
	5	Vessel moves between 1.7 and 4 knots through unmanaged ice.
	6	Vessel encounters floe and stops.

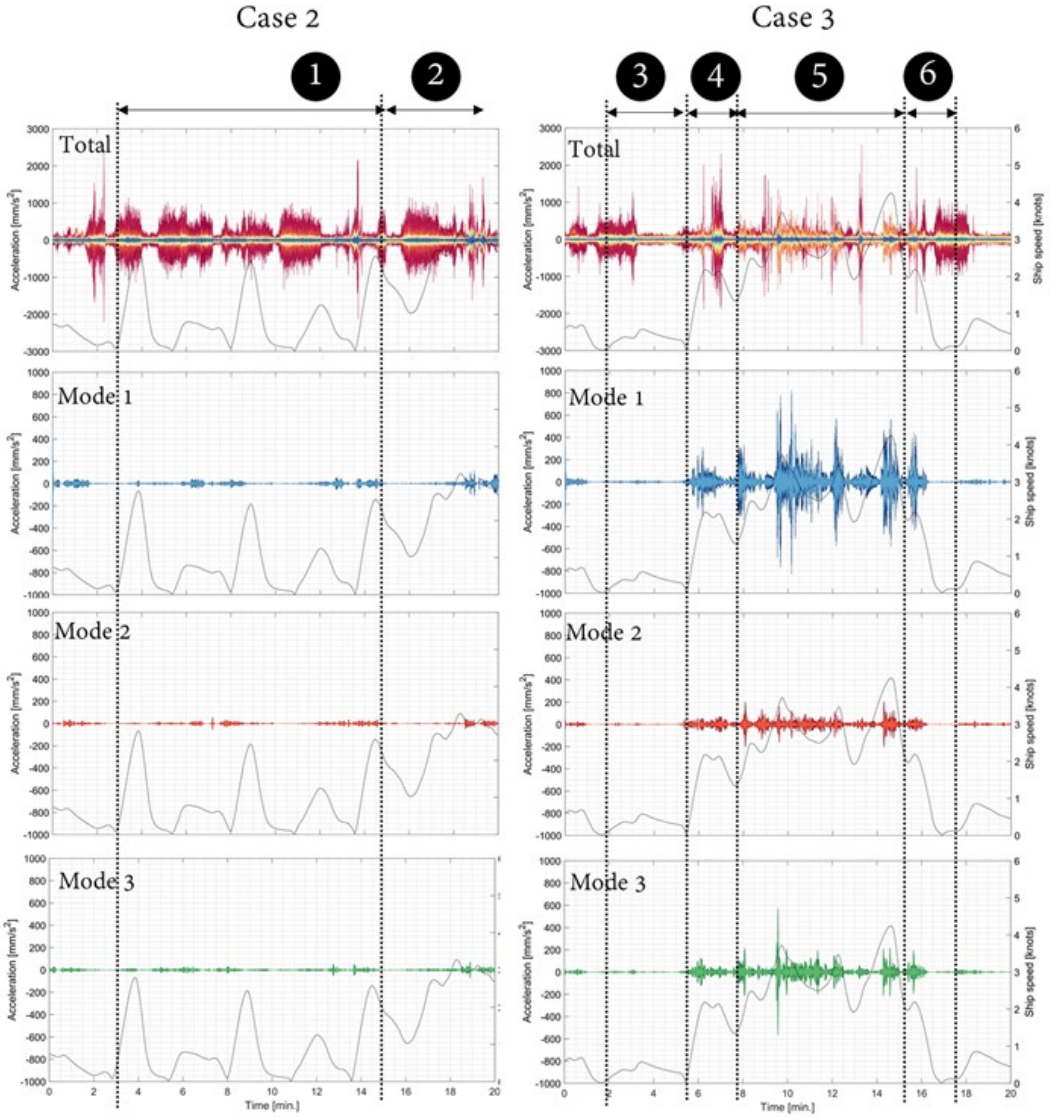

Figure 5.16: Mode bandpass filtered responses for a single observation window from the two ice cases.

5.7.2 Discussion

Time-histories were bandpass filtered to observe the time-varying behaviour of modes. Highly non-stationary responses during wave-slamming and ship-ice interactions were observed. This confirms that the modal responses that occur during these operating conditions can only be captured with sufficiently fine time-resolution. Although two ice cases were considered, the modal responses during the two cases were very different. This could be attributed to different loading

configurations of the ship or different mechanisms of ship-ice interactions.

5.8 Conclusion

The data-driven SSI algorithm was used to identify modes across four different cases which were subsequently tracked using automated modal analysis. Three modes are potential candidates for long-term tracking towards structural health monitoring. Namely the first and second vertical bending modes and lateral bending mode of the ship. The exact reason why certain modes were not well identified across all cases must be further investigated. The highest energy modal responses correspond to the first vertical bending mode and the third vertical bending mode. Significant energy in lateral and torsional modes are sometimes observed during ice navigation but not during open water navigation. Significant amounts of energy are concentrated around the first and second vertical bending modes, especially during open water navigation. Modal responses vary significantly during non-stationary open water storms and ice cases. During the ice cases, the time-varying behaviour of modes were found to potentially predict the occurrence of ship-ice interactions.

Chapter 6

Conclusions and future work

6.1 Conclusions

This thesis investigated the use of operational modal analysis (OMA) towards developing an accurate modal model of the SA Agulhas II. Operational measurements were acquired during a 100 day voyage to East Antarctica and the Weddell Sea from December 2018 to March 2019. The vessel was instrumented with twenty-eight accelerometers to capture vertical, lateral and torisonal motions. A large set of operational data was acquired and the quality of measurements were routinely verified. The vessel encountered harsh open water and ice conditions providing valuable information regarding the response of the vessel under extreme loading conditions. Data was collected over a broad range of operational and environmental conditions with significant variations in cruising speeds, air and water temperature, different ice types as well as different loading configurations of the vessel. The data-driven SSI (SSI-data) technique was explored in detail to identfy the modal parameters of the SA Agulhas II. A parametric investigation on the effect of three user-specified parameters on modal estimates obtained using the SSI-data technique was conducted. The selection of parameters were found to influence both bias and random errors on estimates. Weakly excited modes with low signal-to-noise ratios suffered particularly from incorrect selection of parameters. A set of suitable parameters were identified from a single case of operational data and a modal model consisting of five modes were obtained. OMA was applied to four operational data sets. Calm and stormy open water cases and two ice cases were considered. Modes were automatically tracked within and across different cases. Candidates for long-term tracking towards structural health monitoring were identified. The energies associated with different modes under different operating conditions were investigated. Significant concentrations of large amounts of energy were found to occur for vertical bending modes during the open water

storm case which indicates the potential dangers for structural health relating of ice-going vessels operating in harsh open water conditions for extended periods of time. Further, the transient behaviour of modes during open water wave-slamming and ship-ice interactions were investigated. The transient behaviour of modes were found to correspond to the occurrence of wave-slamming events and failure of ice at the ship-ice interface.

6.2 Future work

Based on key findings obtained in this thesis, future work relating to the following topics are suggested.

6.2.1 Additional parameter studies

The parameter study conducted in Chapter 4 may be extended to include additional operational cases and other identification algorithms, such as covariance-driven SSI. With sufficient observations of mode behaviour statistical reliability can be obtained relating to the correct selection of modal parameters.

6.2.2 Strain measurements near the midship

With large amounts of energy concentrated around vertical bending modes, considerable stresses are likely to occur near midship. Strain measurements may provide key insights into local structural damage that is likely to occur at critical regions on the ship structure.

6.2.3 Studying ice loads based on decomposition of modal responses

Time-varying behaviour of modal responses obtained through bandpass filtering acceleration time-histories were found to indicate the occurrence of ship-ice interactions that result in ice-induced vibrations. Research into the use of this method into the prediction of ice failure modes and the associated ice loads should be considered for future work. This may further compared to results from instantaneous time-frequency analysis techniques such as the Wigner-Ville distribution to assess the quality of information obtained using this technique.

List of References

Andersen, P. and Dohler, M. (2017). Advanced Operational Modal Analysis using Stochastic Subspace Identification and its Applications - Part 1. In: *Operational Modal Analysis Course at 7th International Modal Analysis Conference*.

Bekker, A. (2018). Exploring the blue skies potential of digital twin technology for a polar supply and research vessel. In: *International Marine Design Conference*.

Bekker, A., Soal, K.I. and Mcmahon, K.J. (2017). Whole-body vibration exposure on board a Polar Supply and Research Vessel in open water and in ice. *Cold Regions Science and Technology*.

Bekker, A., Suominen, M., Kujala, P., Johan, R., Waal, O.D. and Soal, K.I. (2018). From data to insight for a polar supply and research vessel. *Ship Technology Research (Schiffstechnik)*, vol. 0, no. 0, pp. 1–17. ISSN 0937-7255.
Available at: `https://doi.org/10.1080/09377255.2018.1464241`

Bekker, A. and van Zijl, C. (2019). The use of line detection to identify random impulses in long time histories. In: *Proceedings of the Eighth International Operational Modal Analysis Conferencei*. Copenhagen.

Belov, I. and Spiridonov, N. (2012). Features of Ship Vibration In Ice Operation Conditions. *International Society of Polar Engineers*.

Bendat, J.S. and Piersol, A.G. (1980). *Engineering applications of correlation and spectral analysis*. Wiley, New York, N.Y. ISBN 0471058874.

Bjerka, M. (2006). Wavelet transforms and ice actions on structures. *Cold Regions Science and Technology*, vol. 44, pp. 159–169.

Bjerkas, M., Skiple, A. and Iver, O. (2007). Applications of continuous wavelet transforms on ice load signals. *Engineering Structures*, vol. 29, pp. 1450–1456.

Blenkarn, K. (1970). Measurement and analysis of ice forces on Cook inlet structures. In: *Proceedings of the Second Annual Offshore Technology Conference*, pp. 365–378. Houston.

Boswald, M. (2016). Analysis of the bias in modal parameters obtained with frequency-domain rational fraction polynomial estimators. In: *ISMA*, September 2016.

Brandt, A. (2011 jan). Noise and Vibration Analysis. In: *Noise and Vibration Analysis*. John Wiley & Sons, Ltd, Chichester, UK. ISBN 9780470746448.

Brandt, A. (2013). The ABRAVIBE Toolbox for Teaching Vibration Analysis and Structural Dynamics. In: *Conference Proceedings of the Society for Experimental Mechanics Series*, vol. 6, pp. 131–141.

Brincker, R. and Andersen, P. (2015). Understanding Stochastic Subspace Identification.

Brincker, R. and Ventura, C. (2015). *Introduction to Operational Modal Analysis*. 1st edn. John Wiley & Sons, Ltd.

Brincker, R., Zhang, L. and Andersen, P. (2000). Modal Identification from Ambient Responses using Frequency Domain. In: *Proceedings of the 18th International Modal Analysis Conference*.

Caetano, E., Magalhaes, F. and Cunha, A. (2009). Online automatic identification of the modal parameters of a long span arch bridge. *Mechanical Systems and Signal Processing Signal Processing*, vol. 23, pp. 316–329.

Cauberghe, B. (2004). *Applied Frequency-domain System Identification in the Field of Experimental and Operational Modal Analysis*. PhD, Vrije Universiteit Brussels.

De Norske Veritas AS (2016). Rules for classification of chips for navigation in ice. Available at: `http://rules.dnvgl.com/docs/pdf/dnv/rulesship/2016-07/ts501.pdf`

Dohler, M. and Mevel, L. (2013). Efficient multi-order uncertainty computation for stochastic subspace identification. *Mechanical Systems & Signal Processing*, vol. 38, no. 2, pp. 346–366.

Erikstad, S.O. (2018). Design patterns for digital twin solutions in marine systems design and operations.

Farrar, C. and Worden, K. (2012). *Structural health monitoring : A machine learning perspective*. Wiley, Oxford.

Finland, S. (2012). SA Agulhas II deck layout drawing. Tech. Rep..

Goethals, I., Vanluyten, B. and Moor, B.D. (2004). Reliable spurious mode rejection using self learning algo- rithms. In: *ISMA*. Leuven, Belgium.

Goursat, M., Mevel, L., Andersen, P. and Dohler, M. (2010). Crystal Clear SSI for Operational Modal Analysis of Aerospace Vehicles. In: *International Modal Analysis Conference (IMAC-XXVII)*.

Govers, Y. (2012). *Parameter identification of structural dynamic models by inverse statistical analysis*. Ph.D. thesis, Unversity of Kassel.

Hair, J.F., Black, W.C., Babin, B.J. and Anderson, R.E. (2014). *Multivariate data analysis*. Harlow edn. PearsonEducation Limited. ISBN 9781292021904.

Hamilton, J., Holub, C., D, M. and Kokkinis T (2011). Ice management support for Arctic floating operations. In: *Arctic Technology Conference*.

Hasan, M.D.A., Ahmad, Z.A.B., Leong, M.S., Hee, L.M. and Idris, M.H. (2019). Cluster Analysis for Automated Operational Modal Analysis : A Review. vol. 2012.

Herlufsen, H., Gade, S., Møller, N. and Andersen, P. (). Identification Techniques for Operational Modal Analysis : An Overview and Practical Experiences.

Heyn, H.-m. and Skjetne, R. (2018). Time-frequency analysis of acceleration data from ship-ice interaction events. *Cold Regions Science and Technology*.

Inman, D.J. (2001). *Engineering vibration*. 2nd edn. Prentice Hall, Upper Saddle River, N.J. ISBN 013726142X.

International Association of Classification Societies (2016). Requirements concerning Polar Class.
Available at: `http://www.iacs.org.uk/download/1803`

James, G.H. and Carne, T.G. (1995). The natural excitation technique (NExT) for modal parameter extraction from operating structures. *The international journal of analytical and experimental modal analysis*, , no. January 2015.

Jelicic, G. and Schwochow, J. (2015). Automatic operational oodal analysis for aeroelastic applications. In: *Proceedings of the 6th International Modal Analysis Conference*. Gijon.

Jordaan, I.J. (2001). Mechanics of ice of structure interaction. *Engineering fracture mechanics*, vol. 68, pp. 1923–1960.

Kailath, T. (1980). *Linear systems T. Kailath.pdf*. PTR Prentice Hall, Englewood Cliffs.

Keshmiri, M. and Mesjidian, M. (2009). A Review on Operational Modal Analysis Researches : Classification of Methods and Applications. In: *Proceedings of the 3rd International Operational Modal Analysis Conference*.

Kotilainen, M., Vanhatalo, J., Suominen, M. and Kujala, P. (2017). Predicting ice-induced load amplitudes on ship bow conditional on ice thickness and ship speed in the Baltic Sea. *Cold Regions Science and Technology*, vol. 135, pp. 116–126. ISSN 0165-232X.

Lanslots, J., Rodiers, B. and Peeters, B. (2004). Automated Pole-Selection : Proof-of-Concept & Validation. , no. January.

Lau, J., Peeters, B., Lanslots, J. and Van Der Auweraer, H. (2007). Automatic modal analysis: Reality or myth ? *Sound and Vibrationand Vibration*, , no. January.

Ljung, L. (1987). *System Identification: Theory for User*. PTR Prentice Hall, Englewood Cliffs.

Lovoll, G. and Kadal, J. (2014). *Big data - the new data reality and industry impact*. DNV GL AS, Hovik, Norway.

Lu, W., Lubbad, R., Hoyland, K. and Løset, S. (2015*a*). Theoretical model study of level ice and wide sloping structure interactions. *Cold Regions Science and Technology*, vol. 101, pp. 40–72.

Lu, W., Lubbad, R. and Løset, S. (2015*b*). Cold Regions Science and Technology In-plane fracture of an ice fl oe : A theoretical study on the splitting failure mode. *Cold Regions Science and Technology*, vol. 110, pp. 77–101. ISSN 0165-232X.
Available at: `https://doi.org/10.1016/j.coldregions.2014.11.007`

Magalhaes, F. and Cunha, A. (2011). Explaining operational modal analysis with data from an arch bridge. *Mechanical Systems & Signal Processing*, vol. 25, pp. 1431–1450.

Maia, N. and Silva, J. (1997). *Theoretical and Experimental Modal Analysis*. Research Studies Press, Baldock.

Marrongelli, G., Magalhães, F. and Cunha, A. (2017). Automated Operational Modal Analysis of an arch bridge considering the influence of the parametric methods inputs. *Procedia Engineering*, vol. 199, pp. 2172–2177.

Matusiak, J. (1982). Dynamic loads and response of icebreaker SISU during continuous icebreaking. *Technical Report Winter Navigation research board Helsinki*.

Melsa, J.L. and Sage, A.P. (1973). *An Introduction to Probability and Stochastic Processes*. Prentice Hall.

Mendler, A., Allahdadian, S., Dohler, M., Mevel, C. and Ventura, C. (2019). Minimum detectable damage for stochastic subspace based methods. In: *Proceedings of the Eighth International Operational Modal Analysis Conferencei*.

Nord, T.S., Petersen, Ø.W. and Hendrikse, H. (2019). Stochastic subspace identification of modal parameters during ice structure interaction. *Philosophical Transactions A*.

Orlowitz, E. and Brandt, A. (2014). Topics in Modal Analysis II : Modal Test Results of a Ship Under Operational Conditions. vol. 8, pp. 4–11. ISBN 9783319047744.

Pang, F., Schen, Z., Li, H. and Xue, Y. (2016). Research on ice breaking induced vibration characteristics of a ship. In: *inter.noise*. Hamburg.

Peeters, B. (2000). *System Identification and Damage Detection in Civil Engineering*. Ph.D. thesis.

Peeters, B. and de Roeck, G. (1999). Reference-based Stochastic Subspace Identification for Output-only Modal Analysis. *Mechanical Systems & Signal Processing*, vol. 13, pp. 855–878.

Peeters, B. and Van Der Auweraer, H. (2005). PolyMax : a revolution in operational modal analysis P OLY MAX : A REVOLUTION IN. In: *1st International Operational Modal Analysis Conference*, January.

Pintelon, R. and Schoukens, J. (2001). *System identification : a frequency domain approach*. IEEE Press, New York. ISBN 0780360001.

Reynders, E. (2012 mar). System Identification Methods for (Operational) Modal Analysis: Review and Comparison. *Archives of Computational Methods in Engineering*, vol. 19, no. 1, pp. 51–124. ISSN 11343060.
Available at: `http://search.proquest.com/docview/1111806428/`

Reynders, E., Maes, K., Lombaert, G. and Roeck, G.D. (2016). Uncertainty quantification in operational modal analysis with stochastic subspace identification : Validation and applications. *Mechanical Systems and Signal Processing*, vol. 66-67, pp. 13–30. ISSN 0888-3270.
Available at: `http://dx.doi.org/10.1016/j.ymssp.2015.04.018`

Reynders, E., Pintelon, R. and Roeck, G.D. (2008). Uncertainty bounds on modal parameters obtained from Stochastic Subspace Identification. *Mechanical Systems & Signal Processing*, vol. 22, no. 4, pp. 948–969.

Rosenow, S.-e. and Uhlenbrock, S. (2007). Parameter extraction of ship structures in the presence of stochastic and harmonic excitations. In: *Proceedings of 2nd International Operational Modal Analysis Conference*.

Sarlo, R., Tarazaga, P.A. and Kasarda, M.E. (2018). High resolution operational modal analysis on a five story smart building under wind and human induced excitation. *Engineering Structures*, vol. 176, no. July, pp. 279–292. ISSN 0141-0296.
Available at: `https://doi.org/10.1016/j.engstruct.2018.08.060`

Soal, K., Govers, Y., Bienert, J. and Bekker, A. (2019*a*). System identification and tracking using a statistical model and a Kalman filter. *Mechanical Systems and Signal Processing*, vol. 133, p. 106127. ISSN 0888-3270.
Available at: `https://doi.org/10.1016/j.ymssp.2019.05.011`

Soal, K., Govers, Y., Böswald, M. and Vollmer, A. (2019*b*). TAXI VIBRATION TESTING : A NEW AND TIME EFFICIENT PROCEDURE FOR THE IDENTIFICATION OF MODAL PARAMETERS ON AIRCRAFTS. In: *IFASD*, June, pp. 1–21.

Soal, K., Volkmar, R., Hughes, L., Govers, Y. and Boswald, M. (2019*c*). Evolutionary based approach to modal parameter identification. In: *Proceedings of the Eigth International Operational Modal Analysis Conference*. Copenhagen.

Soal, K.I. (2015). *Vibration response of the polar supply and research vessel the S. A. Agulhas II in Antarctica and the Southern ocean*. Stellenbosch : Stellenbosch University.

Soal, K.I. (2018). *System identification and modal tracking on ship structures*. Stellenbosch : Stellenbosch University.

Strang, G. (2006). *Linear Algebra and its applications*. 4th edn. Thomson Learning, London.

Su, B., Riska, K. and Moan, T. (2011). Numerical study of ice-induced loads on ship hulls. *Marine Structures*, vol. 24, no. 2, pp. 132–152. ISSN 09518339.

Vacher, P., Jacquier, B. and Bucharles, A. (2010). Extensions of the MAC criterion to complex modes. In: *Proceedings of the Interntional Conference on Noise and Vibration (ISMA)*, pp. 2713–2726.

Van Overschee, P. and De Moor, B. (1992). Subspace algorithm for the stochastic identification problem. In: *Automatic*, vol. 29, pp. 1321 – 1326 vol.2.

van Overschee, P; de Moor, B. (1996). *Subspace Identification for Linear Systems: Theory - Implementation - Applications*. Kluwer Academic Publishers, Dordrecht.

Ventura, C.E., Brincker, R. and Andersen, P. (2001). Damping Estimation by Frequency Domain Decomposition. In: *Proceedings of the International Modal Analysis Conference XIX*, pp. 698–703.

Verboven, P., Parloo, E., Guillaume, P. and van Overmeire, M. (2002). Autonomous structural health monitoring part 1 : mddal parameter estimation and tracking. *Mechanical Systems and Signal Processing*, vol. 16, pp. 637–657.

Volkmar, R., Soal, K., Hughes, L., Govers, Y. and Boswald, M. (2019). Automated optimisation of output only modal paramerer identification. In: *Proceedings of the Eigth International Operational Modal Analysis Conference*. Copenhagen.

Yue, Q., Guo, F. and Kärnä, T. (2009). Cold Regions Science and Technology Dynamic ice forces of slender vertical structures due to ice crushing. *Cold Regions Science and Technology*, vol. 56, no. 2-3, pp. 77–83. ISSN 0165-232X.
Available at: `http://dx.doi.org/10.1016/j.coldregions.2008.11.008`

Yue, Q., Qu, Y., Bi, X. and Tuomo, K. (2007). Ice force spectrum on narrow conical structures. *Cold Regions Science and Technology*, vol. 49, pp. 161–169.

Zabel, V. (2018). *Operational modal analysis Theory and aspects of application in civil engineering*. Ph.D. thesis, Bauhaus Weimar.

Zill, D.G., Warren, S. and Wright, S. (2009). *Advanced Engineering Mathematics*. 5th edn. Jones and Bartlett Publishers.

Appendices

Appendix A

Full voyage description

This appendix provides a description of the fifty-eighth annual South African National Antarctic Expedition (SANAE 58) voyage and Weddell Sea Expedition (WSE) which the SA Agulhas II undertook from 7/12/2018 to 14/03/2019. The vessel spent her longest time at sea since her commissioning in 2012, a total of 100 days. Voyage tracks for both the SANAE 58 voyage and WSE are presented in Figure A.1. A detailed description of the voyages follow.

- The expedition started on 7/12/2019 in Cape Town. The vessel sailed through open water for seven days with several stations conducted underway where the vessel stopped for several hours to deploy scientific equipment and collect samples.
- At approximately 02:00 UTC on 14/12/2018, the vessel reached the marginal ice zone, commencing ice navigation. The vessel encountered harsh ice conditions between 16 and 18 December 2018 which required hours of backing-and-ramming operations before the vessel was able to break through the ice.
- The vessel reached the Fimbul ice shelf on the evening of 18/12/2018 (at approximately 19:50 UTC). The Captain decided not to proceed to the loading point on the shelf due to adverse ice conditions. Instead the vessel was intermittently moved between open water and bay ice close to Otter Bukta.
- Passengers were transported from the ship to the South African Antarctic base by helicopter on 19/12/2018 and logistics operations commenced on 22/12/2018. Cargo was offloaded from the ship for several days at the ice shelf.
- For several days starting on 27 December 2018, members of the WSE charter were transported by helicopter to the vessel from the Antarctic continent.

- On 4 January 2019, the departed from Penguin Bukta, arriving at the Larsen C ice shelf on 10 January 2019. The vessel spent approximately two weeks in the area, conducting oceanographic, biological and glaciological research. Further, sea and ice trials were conducted to test autonomous and remote-operated underwater vehicles that would be used in the search for the Endurance.

- An autonomous underwater vehicle (AUV) was lost under an ice floe during ice trials at approximately 03:00 on 15/01/2019. The vessel spent three days carving ice from the floe to retrieve the AUV. The AUV was recovered from underneath the ice floe at approximately 07:00 on 19/01/2019.

- The science programme commenced after retrieval of the AUV until 27/01/2019 when the vessel set its course to the Endurance Wreck Site in the Western Weddell Sea.

- Due to failure of a remote underwater vehicle (ROV) during trials, the ship changed course to King George Island on 30/01/2019. The vessel arrived at King George Island on 01/02/2019 and maintained position in the bay for three days awaiting spare parts for the ROV. Due to poor weather conditions the spare parts did not arrive and the vessel departed on 05/02/2019 for the Wreck Site as ice conditions in the area were worsening.

- Arrived at the ice edge on 08/02/2019 at 00:30 UTC. The vessel was able to navigate through ice at 7 knots and approached the wreck site at a NW heading using the NE drift of sea-ice to get over the site.

- The vessel arrived at the ice edge at 05:24 UTC on 10/02/2019. Search operations were initiated and the vessel spent the next day providing logistical support for AUV operators.

- On 11/02/2019 at approximately 19:00 the vessel lost contact with the AUV which was lost underneath the sea-ice.

- The vessel started a search operation to retrieve the lost AUV. However, on the evening of 13/02/2019 the search was abandoned since the worsening ice conditions posed the risk that the vessel would be trapped by encroaching sea-ice.

- On 14/02/2019 the vessel departed for Penguin Bukta transiting through open water across the Weddell Sea. Between 17/02/2019 and 19/02/2019 the ship encountered an open water storm with waves reaching 10 m in height.

- The vessel arrived at Penguin Bukta on 20 February 2019.
- On 27/02/2019 the SA Agulhas II departed from Penguin Bukta to return to Cape Town via South Thule and South Georgia.
- The ship arrived at South Georgia on 5/03/2019 and spent the day parked in the before departing for Cape Town in the evening.
- The vessel arrived in Cape Town at 02:00 UTC on 14/03/2019, ending the expedition.

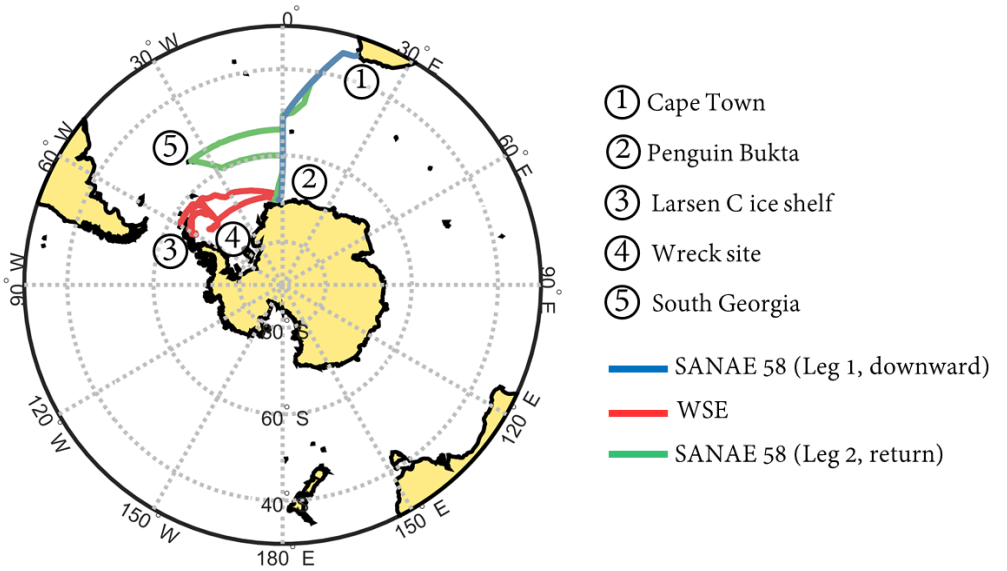

(a)

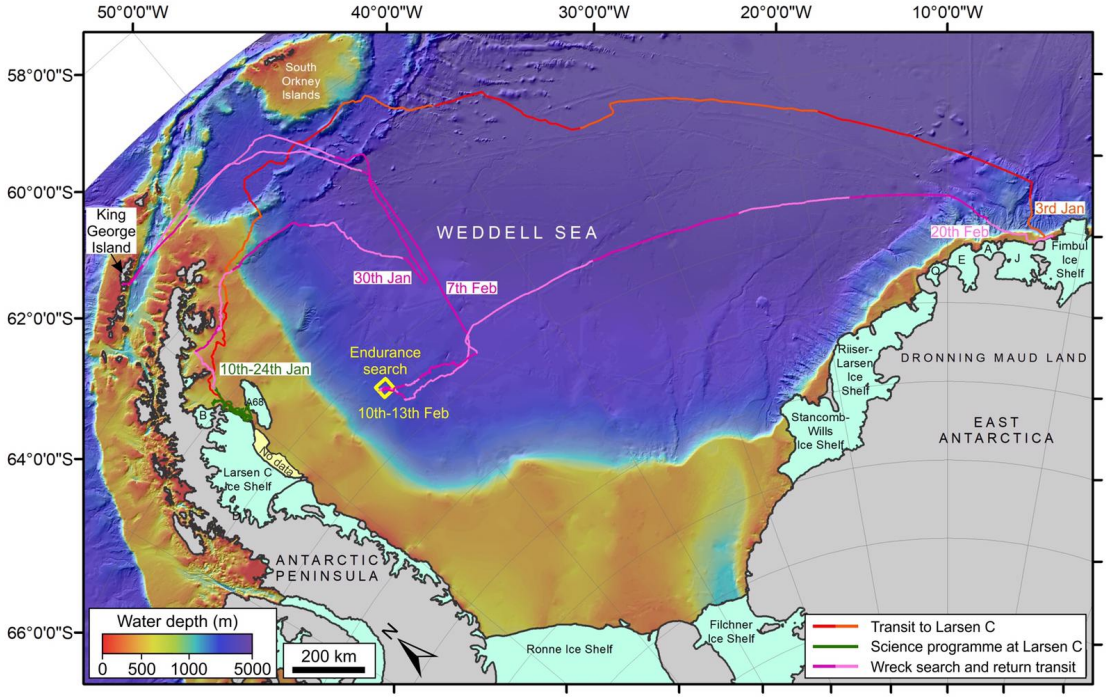

(b)

Figure A.1: Voyage tracks for (a) the entire voyage from 7 December 2018 to 14 March 2019 and (b) the Weddell Sea Expedition.

Appendix B

Stochastic subspace identification

B.1 Stochastic and innovation state space models

Operational modal analysis (OMA) involves estimating modal parameters of structures that are assumed to be excited by white noise inputs that are random in both time and space. In system identification, these types of systems are called stochastic systems and may be modelled by discrete-time stochastic state space models (van Overschee, P; de Moor, 1996):

$$x_{k+1} = Ax_k + w_k \tag{B.1}$$

$$y_k = Cx_k + v_k \tag{B.2}$$

In Eq. B.1 $x_k \in \mathbb{R}^{2n\times 1}$ is a vector containing the $2n$ system state variables and $y_k \in \mathbb{R}^{lx1}$ is a vector containing measurements from l observed outputs of the system. $A \in \mathbb{R}^{n\times n}$ is the state-transition matrix and $C \in \mathbb{R}^{l\times n}$ is the observation matrix. The vectors $w_k \in \mathbb{R}^{n\times 1}$ and $v_k \in \mathbb{R}^{n\times 1}$ are white noise sequences that model the process noise due to modelling inaccuracies (such as non-linearities and time-variance of the system) and noise on the measured outputs, respectively. Concepts related to discrete-time variables and modelling of noise have already been discussed in 2. An important distinction between the stochastic model, as opposed to the deterministic models in Section 2.2 is that the system inputs are not explicitly modelled. Instead these are assumed to be stochastic white noise quantities that are included in the white noise sequences w_k and v_k. Stochastic systems modelled by the discrete-time stochastic state space model are assumed to satisfy certain (ideal) properties (Peeters and de Roeck, 1999). Firstly, relating to the white noise sequences, w_k and v_k are assumed to be zero-mean processes:

$$\mathbf{E}[v_k] = \mathbf{E}[w_k] = 0 \tag{B.3}$$

Here $\mathbf{E}[\cdot]$ denotes the expected value operator. Further, both w_k and v_k are assumed to be Gaussian distributed which means that their behaviour may be fully described by their correlation functions. The correlation functions of w_k and v_k are defined by van Overschee and de Moor (1996) as follows:

$$\mathbf{E}\left(\begin{pmatrix} w_k \\ v_k \end{pmatrix} \begin{pmatrix} w_k^T & v_k^T \end{pmatrix}\right) = \begin{pmatrix} Q & S \\ S^T & R \end{pmatrix} \tag{B.4}$$

Here $Q \in \mathbb{R}^{n\times n}$, and $R \in \mathbb{R}^{l\times l}$ represent the autocorrelation of w_k and v_k, respectively, and S represents the cross-correlation between the two sequences. δ_n is the Kronecker delta operator which is unity at $n = 0$ and zero for all other values of n. Close inspection of the definition in Equation B.4 reveals important properties of the noise sequences w_k and v_k. Firstly, w_k and v_k are stochastic white noise quantities since their autocorrelations and cross-correlations are zero at all time lags except at $n = 0$. Secondly, w_k and v_k are stationary processes since the values of Q,R and S are time invariant. Thirdly, w_k and v_k are correlated with one another since their cross-correlation S is non-zero. Further, assumptions related to the states of the system are that these must zero-mean and uncorrelated with the sequences w_k and v_k:

$$\mathbf{E}[x_k] = 0 \tag{B.5}$$

$$\mathbf{E}[x_k v_k^T] = \mathbf{E}[x_k w_k^T] = 0 \tag{B.6}$$

Moreover, the states are assumed to be stationary (time-invariant) and Gaussian distributed and may, therefore be fully described using the state covariance matrix $\Sigma \in \mathbb{R}^{n\times n}$ (Melsa and Sage, 1973):

$$\mathbf{E}[x_k x_k^T] = \Sigma \tag{B.7}$$

The dynamics of stochastic systems may further be expressed in innovation state space form (Peeters and de Roeck, 1999). The Innovation state space model involves forming optimal system state predictions using the Kalman filter. Assuming an initial predicted state, denoted $\hat{x}_0$ and initial predicted state covariance $\mathbb{E}[\hat{x}_0 \hat{x}_0^T = 0]$, a subsequent state prediction (at time instant $k = 1$) may be formed using the actual observed output y_0 and predicted output $\hat{y}_0 = C\hat{x}_0$ along with known system parameters A and C and known noise covariances Q, R and S using the following equations:

$$\hat{x}_{k+1} = A\hat{x}_k + K_k e_k \tag{B.8}$$

$$e_k = y_k - \hat{y}_k \tag{B.9}$$

Here Eq. B.8 is called the state equation, $\hat{x}_{k+1}$ denotes the predicted state at the next discrete time step, x_k denotes the predicted state at the current time step and K_k is called the Kalman filter gain. Equation B.9 is the correction or update equation and is related to the state equation through the so-called Innovation error e_k, namely the difference between the predicted output $\hat{y}_k$ and the actual observed output y_k. Subsequently, the state equation and update equation may be used recursively to find further predictions of the system state. An important point to note here is that initially the estimated states may be very inaccurate due to the chosen initial conditions. However, in theory, as an increasing number of observed outputs have been used to "correct" the estimated states, the Kalman filter effectively suppresses the influence of noise on the estimates. Eventually, the Kalman filter reaches a steady-state and the Kalman filter gain converges to a constant value and predicted states are considered optimal predictions of the actual system states.

B.2 The data-driven SSI algorithm

The stochastic subspace identification (SSI) algorithms are a set of similar algorithms that identify the unknown dynamic parameters of a stochastic system. In particular, the data-driven SSI algorithm describes system dynamics in innovation state space form (Andersen and Dohler, 2017). Before delving into the technical details of the data-driven SSI algorithm, it is helpful to understand the general progression of the algorithm. A flow diagram of the data-driven SSI algorithm is presented in Figure B.1 which will form a basis for the discussion that follows.

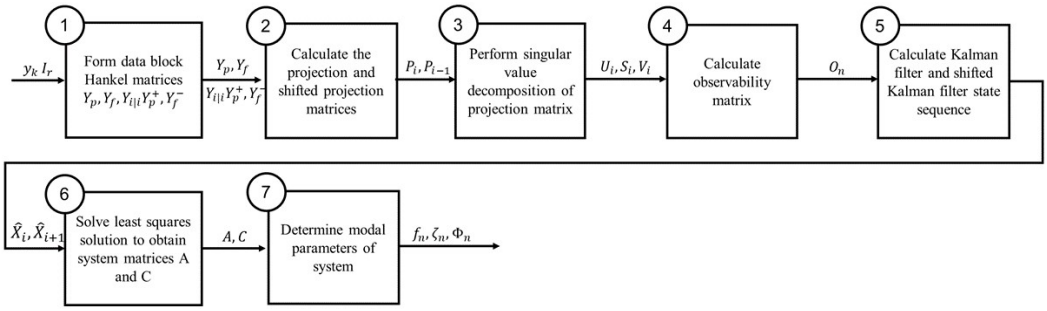

Figure B.1: Flow diagram showing the general progression of the SSI algorithm.

Step 1 of the data-driven SSI algorithm involves the formation of block Hankel data matrices from output measurements. Suppose that $y_k \in \mathbb{R}^{l\times 1}$ represents output measurements collected from l sensors at discrete time instants $k = 1, 2, ..., n_s$, where n_s is the total number of samples. Of these l sensors, a subset of r sensors

may be selected as reference sensors. The reference subset contains only the sensors with the highest quality and are assumed to capture all the physical modes of interest (Herlufsen *et al.*). Measurements from the reference sensors are represented by $y_k^{ref} \in \mathbb{R}^{l\times 1}$ and may extracted from the output measurements for each time instant k:

$$y_k^{ref} = y_k(I_r) \tag{B.10}$$

Where $I_r \in \mathbb{Z}^{r\times 1}$ represents the indices of the reference sensors in the channel table. Using the output measurements, two block Hankel data matrices $Y_p \in \mathbb{R}^{ir\times j}$ and $Y_f \in \mathbb{R}^{il\times j}$ may be constructed as follows (Peeters and de Roeck, 1999):

$$Y_p = \frac{1}{\sqrt{j}}\begin{pmatrix} y_0^{ref} & y_1^{ref} & \cdots & y_{j-1}^{ref} \\ y_1^{ref} & y_2^{ref} & \cdots & y_j^{ref} \\ \vdots & \vdots & \vdots & \vdots \\ y_{i-1}^{ref} & y_i^{ref} & \cdots & y_{i+j-1}^{ref} \end{pmatrix}, Y_f = \frac{1}{\sqrt{j}}\begin{pmatrix} y_i & y_{i+1} & \cdots & y_{i+j} \\ y_{i+1} & y_{i+2} & \cdots & y_{i+j+1} \\ \vdots & \vdots & \vdots & \vdots \\ y_{2i-1} & y_{2i} & \cdots & y_{n_s-1} \end{pmatrix} \tag{B.11}$$

The number of block rows i of Y_p and Y_f represent a user-selected parameter called the block size and the number of columns of each matrix depends on the block size, $j = n_s - 2i + 1$. The matrices in Equation B.11 may further be combined into a single block Hankel matrix $H \in \mathbb{R}^{i(l+r)\times j}$:

$$H = \begin{pmatrix} Y_p \\ Y_f \end{pmatrix} \tag{B.12}$$

Here the block Hankel matrices Y_p and Y_f are referred to as "past" and "future" of the block Hankel matrix H, respectively (van Overschee, P; de Moor, 1996). Two additional block Hankel matrices may now be defined using the block Hankel matrix H. The first is the matrix $Y_{i|i}$ that consists of only the i^{th} block row of H. The second is simply a reorganised (or "shifted") version of the matrix H, denoted H_s (Peeters and de Roeck, 1999):

$$H_s = \begin{pmatrix} Y_p^+ \\ Y_{i|i}^{\sim ref} \\ Y_f^- \end{pmatrix} \tag{B.13}$$

Where the matrix $Y_p^+ \in \mathbb{R}^{(i+1)r\times j}$ contains one additional block row compared to the original matrix Y_p, $Y_{i|i}^{\ ref}$ is formed from the i^{th} block row of Y and contains only the channels that are not in the reference subset and matrix $Y_f^- \in \mathbb{R}^{(i-1)l\times j}$ contains one less block row compared to the original matrix Y_f. The next step (Step 2) of the data-driven SSI calculates the so-called projection matrix $\mathbb{P}_i \in \mathbb{R}^{il\times j}$

and shifted projection matrix $\mathbb{P}_{i-1} \in \mathbb{R}^{il \times j}$. The projection and shifted projection matrices will be explored in further detail in the section that follows. In fact, the main advantage of the data-driven SSI algorithm is that these matrices are never actually calculated (Peeters and de Roeck, 1999). However, for the purposes of the present discussion, the projection and shifted projection matrices are formally defined as functions of the block Hankel matrices that have already been defined (Van Overschee and De Moor, 1992):

$$\mathbb{P}_i = (Y_f Y_p^T)(Y_p Y_p^T)^\dagger Y_p \tag{B.14}$$

$$\mathbb{P}_{i-1} = (Y_f^- Y_p^{+,T})(Y_p^+ Y_p^{+,T})^\dagger Y_p^+ \tag{B.15}$$

The significance of the projection and shifted projection matrices (as they are defined in Eq.B.31 and B.15) is that they hold the following factorisation properties (Dohler and Mevel, 2013):

$$\mathbb{P}_i = O_i \hat{X}_i \tag{B.16}$$

$$\mathbb{P}_{i-1} = O_i^\uparrow \hat{X}_{i+1} \tag{B.17}$$

In Eq. B.31 and Equation B.15 $O_i \in \mathbb{R}^{il \times n}$ is called the observability matrix and $\hat{X}_i \in \mathbb{R}^{n \times j}$ and $\hat{X}_{i+1} \in \mathbb{R}^{n \times j}$ are called the Kalman filter state sequence and shifted Kalman filter state sequence (Peeters and de Roeck, 1999), respectively:

$$\hat{X}_i = \begin{pmatrix} \hat{x}_i & \hat{x}_{i+1} & \cdots & \hat{x}_{i+j-1} \end{pmatrix} \tag{B.18}$$

$$\hat{X}_{i+1} = \begin{pmatrix} \hat{x}_{i+1} & \hat{x}_{i+2} & \cdots & \hat{x}_{i+j} \end{pmatrix} \tag{B.19}$$

The Kalman filter state sequences may be interpreted as follows: the columns of the matrix $\hat{X}_i$ and $\hat{X}_{i+1}$ are the outputs of a steady-state Kalman filter given as inputs the columns of the matrices Y_p and Y_p^+, respectively (Peeters and de Roeck, 1999). This idea will be explored in detail in the following section. For now it is important to notice that the observability matrix from the facorisation of the projection and shifted matrices holds the unknown system parameters of the discrete-time stochastic state space model in the following structure:

$$O_i = \begin{pmatrix} C \\ CA \\ \vdots \\ CA^{i-1} \end{pmatrix} \tag{B.20}$$

In Step 3 of the data-driven SSI algorithm the observability matrix is obtained by performing a singular value decomposition (SVD) on the projection matrix (Van Overschee and De Moor, 1992):

$$\mathbb{P}_i = U_i S_i V_i^T \tag{B.21}$$

Here $U_i \in \mathbb{R}^{n\times n}$ and $V_i \in \mathbb{R}^{n\times n}$ are orthonormal matrices and $S_i \in \mathbb{R}^{n\times n}$ is a matrix that contains singular values along its diagonal and zero entries everywhere else. Often the model order n is selected such that it is much larger than the actual model order of the system n_m (Peeters and de Roeck, 1999). The actual order of the system can be determined from the number of significant singular vectors in the matrix Σ_1 (Van Overschee and De Moor, 1992):

$$S_i = \begin{pmatrix} S_1 & 0 \\ 0 & S_0 \end{pmatrix} \tag{B.22}$$

Here Σ_1 represent the part of the matrix Σ_i that contains significant singular values and Σ_0 represents that part of the matrix that contains singular values that are negligible. The observability matrix and is determined from the factors of the SVD in Step 4 of the general SSI algorithm:

$$O_n = U_n S_1^{1/2} \tag{B.23}$$

The aim is now to extract the system matrices from the observability matrix (Step 5). In the original formulation presented by van Overschee, P; de Moor (1996), this is achieved by first calculating the Kalman filter state sequences:

$$\hat{X}_i = O_n^{\dagger} P_i, \qquad \hat{X}_{i+1} = O_n^{\uparrow,\dagger} P_{i-1} \tag{B.24}$$

Then a system of overdetermined equations may be constructed for the Innovation state space model using the (known) Kalman filter state sequences and the matrix $Y_{i|i}$ (Peeters and de Roeck, 1999):

$$\begin{aligned} \begin{pmatrix} \hat{x}_{i+1} & \hat{x}_{i+2} & \cdots & \hat{x}_{i+j} \end{pmatrix} &= A \begin{pmatrix} \hat{x}_i & \hat{x}_{i+1} & \cdots & \hat{x}_{i+j-1} \end{pmatrix} + \rho_w \\ \hat{X}_{i+1} &= A\hat{X}_i + \rho_w \end{aligned} \tag{B.25}$$

$$\begin{aligned} \begin{pmatrix} \hat{y}_i & \hat{y}_{i+1} & \cdots & \hat{y}_{i+j} \end{pmatrix} &= C \begin{pmatrix} \hat{x}_{i+1} & \hat{x}_{i+2} & \cdots & \hat{x}_{i+j} \end{pmatrix} + \rho_c \\ \hat{Y}_{i|i} &= C\hat{X}_{i+1} + \rho_c \end{aligned} \tag{B.26}$$

Where ρ_w and ρ_v are residuals that contain the innovation error. Equation B.2 and Eq. B.2 may be combined into a single equation:

$$\begin{pmatrix} \hat{X}_{i+1} \\ Y_{i|i} \end{pmatrix} = \begin{pmatrix} A \\ C \end{pmatrix} \hat{X}_i + \begin{pmatrix} \rho_w \\ \rho_v \end{pmatrix} \tag{B.27}$$

Since the noise residuals ρ_v and ρ_w are assumed to be uncorrelated with the system states, van Overschee, P; de Moor (1996) suggest that Equation B.27 may be solved in a least squares sense to obtain estimates for the state transition and observation matrix:

$$\begin{pmatrix} A \\ C \end{pmatrix} = \begin{pmatrix} \hat{X}_{i+1} \\ Y_{i|i} \end{pmatrix} \hat{X}_i^{\dagger} \tag{B.28}$$

Once the state transition matrix is available, the modal parameters can be determined in Step 6 of the general SSI algorithm. First an eigenvalue decomposition of the state matrix A is calculated. The resulting continuous-time poles then to be transformed to discrete-time and the observable part of the eigenvector needs to be extracted:

$$\lambda_{d,r} = \log(\lambda_{c,r}) \ , \ \psi_{d,r} = C\psi_{c,r} \tag{B.29}$$

The natural frequencies and damping ratios may then be determined from the discrete-time poles as follows:

$$f_r = \frac{|\lambda_{d,r}|}{2\pi} \ , \ z_r = \frac{-\mathcal{R}(\lambda_{d,r})}{|\lambda_{d,r}|} \tag{B.30}$$

B.3 The projection matrix

In the previous section, the projection matrix was formally defined as follows:

$$\mathbb{P}_i = (Y_f Y_p^T)(Y_p Y_p^T)^{\dagger} Y_p \tag{B.31}$$

Further, it was stated that the projection matrix holds an important factorisation property that makes it possible to obtain the unknown system parameters. This section aims to clarify two concepts. Firstly, the reason why the projection matrix satisfies the factorisation property in Equation B.16. Secondly, the basis for the definition of the projection matrix in Equation B.31. Further, the implementation of the data-driven SSI algorithm is addressed. In particular, it is shown that the projection matrix never has to be calculated to solve for the unknown system parameters.

To understand why the projection matrix can be factorised according to Equation B.16, the projection matrix should literally be interpreted as a matrix of

"projections" or estimates (Brincker and Andersen, 2015). In other words, the columns of the projection matrix are a type of estimate of the columns of the block Hankel matrix Y_f based on i "past" outputs which are found in the corresponding columns of the block Hankel matrix Y_p. The projection matrix may thus be expressed in the following form:

$$\mathbb{P}_i = \hat{Y}_f = \begin{pmatrix} \hat{y}_{i+1} & \hat{y}_{i+2} & \cdots & \hat{y}_{i+j} \\ \hat{y}_{i+2} & \hat{y}_{i+3} & \cdots & \hat{y}_{i+j+1} \\ \vdots & \vdots & \vdots & \vdots \\ \hat{y}_{2i} & \hat{y}_{2i+1} & \cdots & \hat{y}_{2i+j} \end{pmatrix} \tag{B.32}$$

Predicted variables may be formally defined using the conditional expectation operator (Melsa and Sage, 1973), which is a mathematical operator that produces an estimate of a variable given that a set of conditions are satisfied. Mathematically this definition is expressed as:

$$\hat{a} = \mathbf{E}[a|b] \tag{B.33}$$

In Eq. B.33 $\hat{a}$represents the conditional expectation (estimate) of the variable a and b represents the conditions that must be fulfilled. Suppose now that a predicted state variable and predicted output variable are defined using the conditional expectation operator (Andersen and Dohler, 2017):

$$\hat{x}_k = \mathbf{E}[x_k|Y_0^{k-1}] \tag{B.34}$$

$$\hat{y}_k = \mathbf{E}[y_k|Y_0^{k-1}] \tag{B.35}$$

In Eq. B.34 and Eq. B.35, the conditions imposed on the predicted variables are all the past observed outputs of the system, represented by the matrix Y_0^{k-1}:

$$Y_0^{k-1} = \begin{pmatrix} y_0 \\ y_1 \\ \vdots \\ y_{k-1} \end{pmatrix} \tag{B.36}$$

Using the observation equation of the discrete-time stochastic state space model, the predicted the outputs $\hat{y}_k$ may be expressed as follows:

$$\hat{y}_k = \mathbf{E}[(Cx_k + v_k)|Y_1^{k-1}]$$

$$\hat{y}_k = \mathbf{E}[Cx_k|Y_1^{k-1}] + \mathbf{E}[v_k|Y_1^{k-1}]$$

$$\hat{y}_k = C\hat{x}_k \tag{B.37}$$

Applying a similar conditional expectation to the state equation of the discrete-time stochastic state space model, a so-called one-step forward prediction of the state of the system is obtained:

$$\hat{x}_{k+1} = \mathbf{E}[(Ax_k + w_k)|Y_1^{k-1}]$$

$$\hat{x}_{k+1} = \mathbf{E}[Ax_k|Y_1^{k-1}] + \mathbf{E}[w_k|Y_1^{k-1}]$$

$$\hat{x}_{k+1} = A\hat{x}_k \tag{B.38}$$

It is further possible, using Equation B.3, to similarly define a two-step forward prediction of the state variable:

$$\hat{x}_{k+2} = A(A\hat{x}_k) = A^2\hat{x}_k \tag{B.39}$$

Which may be generalised to express a n-step forward prediction of the system states as:

$$\hat{x}_{k+n} = A^n\hat{x}_k \tag{B.40}$$

Now combining the result in Equation B.3 with Equation B.40 an n-step forward prediction of the system output may be written as:

$$\hat{y}_{k+n} = CA^n\hat{x}_k \tag{B.41}$$

The significance of the result in Equation B.42 is that, by definition, each column of the projection matrix is a sequence of $1, 2, 3, ..., i$ step forward predictions based on i past outputs contained in the corresponding columns of the matrix Y_p (Andersen and Dohler, 2017). For example, using Equation B.42 the first column of $\hat{Y}_f$ may be written as:

$$\hat{Y}_{[0:i-1,1]} = \begin{pmatrix} C \\ CA \\ CA^2 \\ \vdots \\ CA^{i-1} \end{pmatrix} \hat{x}_i = O_i \hat{x}_i \tag{B.42}$$

Where the observability matrix O_i was defined in the previous section. Extending this to include all the columns of $\hat{Y}_f$, it is shown that the projection matrix satisfies the general subspace matrix factorisation property:

$$\mathbb{P}_i = \hat{Y}_f = O_i \hat{X}_i \tag{B.43}$$

Here $\hat{X}_i$ is called the Kalman filter state sequence which was defined in the previous section. It is worth pointing out the similarity between the result in Equation B.42 and the form of the free decay vibration which was defined in 2.2.3 as (Brincker and Andersen, 2015):

$$y_k = CA^k x_0 \tag{B.44}$$

From this perspective, the columns of the projection matrix $\mathbb{P}_i$ may be interpreted as free decays that result from different initial conditions specified in the Kalman filter state sequence. In other words, the predicted values in the columns of $\hat{Y}_f$ are the result of a Kalman filter which uses the corresponding columns of the Kalman filter state sequences as initial values. Since these free decays have the same dynamic properties of the system itself (according to Equation B.42), intuitively it would make sense that the matrix $\hat{Y}_f$ may be used to extract the matrices A and C. These interpretations will become especially important in the next section where the effect of SSI parameters (such as the size of the block Hankel data matrices) are discussed. An important question remains to be answered, namely the basis for defining the projection matrix $\hat{Y}_f$ as a function of the block Hankel matrices Y_p and Y_f. As previously stated, the projection matrix represents a type of estimate of Y_f and is formally defined as follows:

$$\mathbb{P}_i \equiv (Y_f Y_p^T)(Y_p Y_p^T)^\dagger Y_p \tag{B.45}$$

The expression on the right-hand side of Equation 2.16 represents a conditional expectation of the matrix Y_f assuming stationary (ergodic) conditions (Melsa and Sage, 1973). This conditional expectation may further be interpreted as an orthogonal projection of the matrix Y_f onto the row space of the matrix Y_p. The row space of the matrix Y_p is defined as the linear combination of all linearly independent rows in the matrix (Zill *et al.*, 2009). (If a set of vectors are linearly independent it means that none of the vectors in the set can be expressed as a

linear combination of the other vectors in the set). The linearly independent row vectors of Y_p are said to form a basis of Y_p. The number of basis vectors is called the dimension of the row space, which in this case is the model order n, where $n \leq ir$. Further, each basis vector has j components and therefore the row space is a n-dimensional subspace of a j- dimensional space, denoted $\mathbb{R}^j$. The orthogonal projection of Y_f onto the row space of Y_p is illustrated in Figure B.2. Each row of Y_f, denoted y_f, which is assumed to lie outside the row space of Y_p, is projected onto the row space of Y_p. The result is an estimate of the row of Y_f, denoted $\hat{y}_f$, that lies in the row space of Y_p. This means that the vector $\hat{y}_f$ may be expressed in terms of basis vectors that span the row space of Y_p. Assuming that all the rows of the matrix Y_p are linearly independent and form the basis of the row space, the vector $\hat{y}_f$ may be written as:

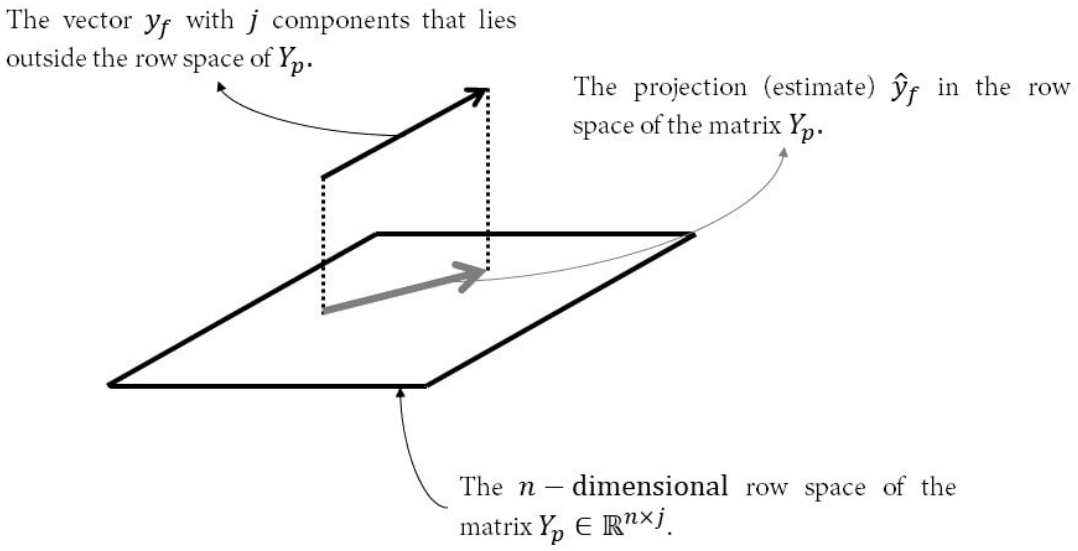

Figure B.2: Graphical description of the projection in data-driven SSI.

$$\hat{y}_f = \sum_{q=1}^{i} c_q \begin{pmatrix} y_q^{ref} & y_{q+1}^{ref} & \cdots & y_{q+j}^{ref} \end{pmatrix} \tag{B.46}$$

Which may be written in matrix form as:

$$\hat{y}_f = \begin{pmatrix} c_1 & c_2 & \cdots & c_i \end{pmatrix} \begin{pmatrix} y_1^{ref} & y_2^{ref} & \cdots & y_j^{ref} \\ y_2^{ref} & y_3^{ref} & \cdots & y_{j+1}^{ref} \\ \vdots & \vdots & \vdots & \vdots \\ y_i^{ref} & y_{i+1}^{ref} & \cdots & y_{i+j-1}^{ref} \end{pmatrix} \tag{B.47}$$

$$\hat{y}_f = cY_p \tag{B.48}$$

Where the matrix $c \in \mathbb{R}^{1\times i}$ holds the coefficients of the linear combination of basis vectors. The error e between the actual vector y_f and the projection $\hat{y}_f$ is defined as (Strang, 2006):

$$e = y_f - \hat{y}_f \tag{B.49}$$

Which is perpendicular to the row space of Y_p:

$$eY_p^t = 0 \tag{B.50}$$

Eq. B.50 comes from the fact that the vector e is perpendicular to all the rows in Y_p which means that the dot product in B.50 must result in the zero vector (Strang, 2006). Substituting B.49 into B.50 and simplifying yields the following:

$$\begin{aligned} (y_f - \hat{y}_f)Y_p^t &= 0 \\ (y_f - cY_p^T)Y_p^t &= 0 \\ y_f Y_p^T &= cY_p^T Y_p^t \end{aligned} \tag{B.51}$$

Which results in the following expression for the row vector c:

$$c = (y_f Y_p^T)(Y_p^T Y_p^t)^\dagger \tag{B.52}$$

Substituting the result in B.52 into Eq. B.48 results in an expression for $\hat{y}_f$.

$$\hat{y}_f = (y_f Y_p^T)(Y_p Y_p^T)^\dagger Y_p \tag{B.53}$$

Which may be generalised for all the rows in Y_f to obtain the definition in Eq. B.66.

B.4 Implementation of data-driven SSI

Up to this point, the discussion has focused on providing a theoretical basis for the data-driven SSI algorithm. However, one of the most important aspects of the implementation of data-driven SSI is that the projection matrix never has to be explicitly calculated using Eq. B.66 (Peeters and de Roeck, 1999). The reason for this will, hopefully, become clearer in the discussion that follows. First, consider again the block Hankel matrix H_s defined in **??**:

$$H_s = \begin{pmatrix} Y_p^+ \\ Y_{i|i}^{\sim ref} \\ Y_f^- \end{pmatrix} \tag{B.54}$$

Now using a numerical technique called QR factorisation this matrix may be factored into a lower triangular matrix $R \in \mathbb{R}^{(r+l)i \times j}$ and an orthonormal matrix $Q \in \mathbb{R}^{j \times j}$ ($QQ^T = Q^TQ = I$) (van Overschee, P; de Moor, 1996):

$$H_s = \begin{pmatrix} Y_p^+ \\ Y_{i|i}^{\sim ref} \\ Y_f^- \end{pmatrix} = RQ^T \tag{B.55}$$

Since the dimension $(r+l)i < j$ zeros in both the $R$and$Q$ factors may be omitted and the QR factorisation may be written in the following convenient form (Peeters and de Roeck, 1999):

$$H_s = \begin{array}{c} \\ ri \\ r \\ (l-r) \\ i(l-1) \end{array} \begin{array}{c} \begin{array}{cccc} ri & r & (l-r) & i(l-1) \\ \leftrightarrow & \leftrightarrow & \leftrightarrow & \leftrightarrow \end{array} \\ \begin{pmatrix} R_{11} & 0 & 0 & 0 \\ R_{21} & R_{22} & 0 & 0 \\ R_{31} & R_{32} & R_{33} & 0 \\ R_{41} & R_{42} & R_{43} & R_{44} \end{pmatrix} \end{array} \begin{array}{c} j \\ \leftrightarrow \\ \begin{pmatrix} Q_1^T \\ Q_2^T \\ Q_3^T \\ Q_4^T \end{pmatrix} \end{array} \tag{B.56}$$

At this stage the reason for performing this QR factorisation may not be entirely clear. However, the point is that the properties of the Q and R factors make it possible to write different parts of the matrices H and H_s as functions of certain rows in R and the matrix Q:

$$Y_p = \begin{pmatrix} R_{11} & 0 & 0 & 0 \end{pmatrix} Q^T$$

$$Y_f = \begin{pmatrix} R_{21} & R_{22} & 0 & 0 \\ R_{31} & R_{32} & R_{33} & 0 \\ R_{41} & R_{42} & R_{43} & R_{44} \end{pmatrix} Q^T$$

$$Y_{i_i} = \begin{pmatrix} R_{21} & R_{22} & R_0 & 0 \\ R_{31} & R_{32} & R_{33} & 0 \end{pmatrix} Q^T \tag{B.57}$$

$$Y_p^+ = \begin{pmatrix} R_{11} & 0 & 0 & 0 \\ R_{21} & R_{22} & 0 & 0 \end{pmatrix} Q^T$$

$$Y_f^- = \begin{pmatrix} R_{41} & R_{42} & R_{43} & R_{44} \end{pmatrix} Q^T$$

Using the definitions in Eq. B.4, it is further possible to express the projection and shifted projection matrices in terms of Q and R factors:

$$P_i = \begin{pmatrix} R_{21} \\ R_{31} \\ R_{41} \end{pmatrix} Q^T \tag{B.58}$$

$$P_{i-1} = \begin{pmatrix} R_{41} & R_{42} \end{pmatrix} \begin{pmatrix} Q_1^T \\ Q_2^T \end{pmatrix} \tag{B.59}$$

The significance of expressing the projection matrix in terms of Q and R factors is that its singular values and vectors may be obtained from blocks of the R matrix (Van Overschee and De Moor, 1992). This means that the observability matrix may be obtained by performing a singular value decomposition of the R factors in Equation B.58:

$$\begin{pmatrix} R_{21} \\ R_{31} \\ R_{41} \end{pmatrix} = U_i S_i V_i^T$$

$$O_n = U_n S_n^{1/2} \tag{B.60}$$

Where, as defined in the previous section, n is the actual model order of the system and represents the $n \times n$ subspace that contains the significant singular

values of S. As explained in Section B.2 a system of overdetermined equations may be constructed for the Innovation state space model using the Kalman filter state sequences and the matrix $Y_{i|i}$ to solve for the unknown system parameters:

$$\begin{pmatrix} A \\ C \end{pmatrix} = \begin{pmatrix} \hat{X}_{i+2} \\ Y_{i|i} \end{pmatrix} \hat{X}_{i+1}^{\dagger} \tag{B.61}$$

Recalling the following expressions for the Kalman filter state sequences from Section B.2:

$$\hat{X}_{i+1} = O_n^{\dagger} P_i, \quad \hat{X}_{i+2} = O_n^{\uparrow,\dagger} P_{i-1} \tag{B.62}$$

And using the fact that the projection matrix and shifted projection matrix may be expressed in terms of Q and R factors, Eq. B.27 may be expressed as follows:

$$\begin{pmatrix} A \\ C \end{pmatrix} = \begin{pmatrix} O_n^{\uparrow,\dagger} \begin{pmatrix} R_{41} & R_{42} \end{pmatrix} \begin{pmatrix} Q_1^T \\ Q_2^T \end{pmatrix} \\ \begin{pmatrix} R_{21} & R_{22} & 0 \\ R_{31} & R_{32} & R_{33} \end{pmatrix} \begin{pmatrix} Q_1^T \\ Q_2^T \\ Q_3^T \end{pmatrix} \end{pmatrix} \left(O_n^{\dagger} \begin{pmatrix} R_{21} \\ R_{31} \\ R_{41} \end{pmatrix} Q_1^T \right)^{\dagger} \tag{B.63}$$

Due to the orthonormality of the Q factors ($QQ^T = Q^TQ = I$), A and C may be expressed as functions of only the R factors from the QR factorisation in Eq. B.56:

$$A = O_n^{\uparrow,\dagger} R_{41} \begin{pmatrix} R_{21} \\ R_{31} \\ R_{41} \end{pmatrix}^{\dagger} O_n \tag{B.64}$$

$$C = \begin{pmatrix} R_{21} \\ R_{31} \end{pmatrix} \begin{pmatrix} R_{21} \\ R_{31} \\ R_{41} \end{pmatrix}^{\dagger} O_n \tag{B.65}$$

Since only the R factors are necessary to compute the system matrices, a significant data reduction is achieved through performing the QR factorisation of the block Hankel matrix Y_s (Peeters and de Roeck, 1999).

B.5 User-specified parameters in data-driven SSI

In literature, some guidelines are available regarding the selection of these parameters. This section addresses the selection of these parameters by building upon the theoretical basis provided in the previous section.

B.5.1 Reference channels

The most computationally demanding step in the data-driven SSI algorithm is the QR factorisation of the matrix Y_s. Therefore, an obvious advantage of using reference channels is that the row dimension of the block Hankel matrix Y_p is reduced by ri, which implies a similar reduction in the row dimension of Y_s. Reference channels are typically used to increase the spatial resolution of identified mode shapes when a limited number of sensors are available (Peeters and de Roeck, 1999). Furthermore, studies have found that reference channels reduces redundant information in the data matrices which normally results in the identification of spurious (mathematical) modes (Herlufsen *et al.*). Moreover, optimising the number of reference channels (namely using the fewest number of reference channels that contain all the necessary physical information) produces stable modes at lower model orders (Peeters and de Roeck, 1999).

B.5.2 Measurement duration

Under stationary conditions, increasing measurement duration is expected to improve data-driven SSI modal parameter estimates. Consider the definition of the projection matrix in data-driven SSI:

$$P_i \equiv (Y_f Y_p^T)(Y_p Y_p^T)^\dagger Y_p \tag{B.66}$$

In this definition, the matrices $Y_f Y_p^T$ and $Y_p Y_p$ contain unbiased estimates of covariances of the output data at different time lags Reynders *et al.* (2008); Brincker and Andersen (2015):

$$(Y_p Y_p^T) = \begin{pmatrix} \hat{\Lambda}_0 & \hat{\Lambda}_1 & \cdots & \hat{\Lambda}_i \\ \hat{\Lambda}_1 & \hat{\Lambda}_2 & \cdots & \hat{\Lambda}_{i+1} \\ \vdots & \vdots & \vdots & \vdots \\ \hat{\Lambda}_i & \hat{\Lambda}_{i+1} & \cdots & \hat{\Lambda}_{21} \end{pmatrix} \tag{B.67}$$

$$(Y_f Y_p^T) = \begin{pmatrix} \hat{\Lambda}_i & \hat{\Lambda}_{i-1} & \cdots & \hat{\Lambda}_1 \\ \hat{\Lambda}_{i+1} & \hat{\Lambda}_i & \cdots & \hat{\Lambda}_2 \\ \vdots & \vdots & \vdots & \vdots \\ \hat{\Lambda}_{2i} & \hat{\Lambda}_{2i-1} & \cdots & \hat{\Lambda}_i \end{pmatrix} \tag{B.68}$$

Where Λ_q for $q = 0, 1, 2, ...2i$ is defined as the output covariance matrix (Van Overschee and De Moor, 1992)

$$\Lambda_q = \lim_{N\to\infty} \frac{1}{N} \sum_{k=0}^{N} y_{k+q} y_k^T \tag{B.69}$$

And $\hat{\Lambda}_q$ is an unbiased estimate of the covariance matrix (Reynders *et al.*, 2008):

$$\hat{\Lambda}_q = \frac{1}{N-q} \sum_{k=0}^{N-q} y_{k+q} y_k^T \tag{B.70}$$

From a statistical perspective, the covariances are sufficient to fully characterise the output signals, assuming that the outputs are Gaussian-distributed and stationary (Melsa and Sage, 1973). Further, since the estimates are unbiased, sufficiently long data segments (i.e. where $j \to \infty$) effectively removes bias errors which would otherwise be propagated to the modal parameter estimates (Van Overschee and De Moor, 1992). Of course, in reality, systems are not usually analysed under stationary conditions. This may be due to changing inputs which result in non-stationary outputs or changes in the system itself (changes in dynamic properties or boundary conditions). Sometimes these changes are negligible and there is no danger in selecting excessive measurement durations. However, if the non-stationary behaviour of the system is significant, long measurement durations may produce "smeared" average estimates of the modal parameters and information about the time-varying behaviour of the system will be lost.

B.5.3 Block size

Block size has a significant influence on the computational cost of the data-driven SSI algorithm. Increasing block size by δi has the effect of increasing the number of rows of the projection matrix by $(r+l)\delta i$ rows while decreasing the column dimension by $2\delta i$. Since in most cases $(r+l) > 2$, increasing the block size is often limited by the amount of computational power that is available. However, there are a few guidelines regarding a minimum block size. Firstly, the block size should be large enough to extract all the dynamic modes from the state transition matrix, i.e. $i_{min} \leq n/r$ where n is the actual order of the system and r is the number of reference channels Peeters and de Roeck (1999). Secondly, the block size relates to the number of rows in the projection matrix $\hat{Y}_f$. Since the columns of the projection matrix may be interpreted as free decays with dynamic properties equivalent to the dynamic properties of the system, few samples or observations of the free decay will be insufficient to capture all the modal information in the signal (Van Overschee and De Moor, 1992). This is especially problematic for low frequency modes and the minimum block size should be chosen such that $i_{min} \leq f_s/f_{min}$ where f_s is the sample rate and f_{min} is the lowest natural frequency in the modal model (van Overschee, P; de Moor, 1996). Thirdly, one of the key ideas in data-driven SSI is that optimal predictions can be formed for the system states and outputs based on past observations of the outputs by correcting for the effect of

noise at each time step. This correction is achieved by comparing the actual output to the predicted output at each time step. Ideally, the differences between actual and predicted outputs should become smaller over time and the Kalman filter (which produces these estimates) should reach a steady state (Van Overschee and De Moor, 1992). However, this assumes that all past outputs are used to form the predicted states and outputs when, in the data-driven SSI algorithm, only i past outputs are used. Therefore, for real systems where modal responses are buried in large amounts of noise, large block sizes may be necessary to extract all the dynamic behaviour of the system.

Using excessive block sizes increases computational cost drastically and does not necessarily produce improved estimates. Studies on simulated data by Van Overschee and De Moor (1992) and Soal (2018) showed that modal parameter estimates converge with increasing block size. Soal (2018) further states that large block sizes result in the identification of many spurious modes with frequencies close to that of physical modes. One reason for this may be that large block sizes produces an ill-conditioned matrix $Y_pY_p^T$ (Andersen and Dohler, 2017) which introduces numerical errors in the projection matrix. This ill-conditioning occurs because $Y_pY_p^T$ holds output covariance matrices for time lags $i = 1, 2, ..., 2i$. Increasing the number of time lags (block size), increases the number of elements in $Y_pY_p^T$ that are close to zero which increases the sparsity of the matrix. Further, since the columns of the projection matrix holds vibration free decays large block sizes means that the "tails" of the free decays are included in the estimation process. These tails contain mostly noise since the modal responses have most likely decayed to zero (or close to zero).

B.5.4 Model order

Model order relates to the maximum number of modes that can be extracted from measured data. If the system is assumed to be under-damped, then the model order must be chosen to be at least twice the number of modes since the eigensolution of the state-transition matrix contains complex conjugate pairs (Maia and Silva, 1997). However, often the exact number of modes are not known exactly. For this reason, common practise is to repeat the identification calculation for increasing model orders where the maximum model order is chosen to be much larger than the actual number of modes (Lau *et al.*, 2007). The results are then plotted in a stabilisation diagram with all the identified frequencies on the abscissa and corresponding model order on the vertical axis. The physical modes should appear as "stable" vertical lines that appear at every consecutive model order while spurious modes are unstable and change significantly from one model order to the

next. The challenge, however is to know at which model order each mode should be selected.